The production of η and ω mesons in 3.5 GeV p+p interaction in HADES

Dissertation
zur Erlangung des Doktorgrades
der Naturwissenschaften

vorgelegt am Fachbereich Physik
der Goethe-Universität
in Frankfurt am Main

von
Khaled Teilab
aus Paris

Frankfurt 2011
(D30)

vom Fachbereich Physik der
Goethe-Universität als Dissertation angenommen.

Dekan:	Prof. Dr. Huth
Gutachter:	Prof. Dr. Ströbele, Prof. Dr. Stroth
Datum der Disputation:	31. August 2011

Kurzfassung

Die Untersuchung der Mesonenproduktion in Proton-Proton Kollisionen bei Energien von bis zu einem GeV über der Produktionsschwelle liefert wichtige Informationen über die Wechselwirkung zwischen Nukleonen. Theoretische Modelle beschreiben die Wechselwirkung zwischen Nukleonen über den Austausch von Mesonen. In diesen Modellen tragen verschiedene Wechselwirkungsmechanismen zur Produktion von Mesonen in Nukleon-Nukleon Kollisionen bei. Messungen von differentiellen und integralen Produktionsquerschnitten liefern somit wichtige Informationen, mit deren Hilfe der Beitrag der einzelnen Wechselwirkungsmechanismen ermittelt werden kann. Darüber hinaus liefern solche Studien essentielle Ausgangsdaten für Transportmodelle, die z.B. die Elektronenpaarproduktion in Pion- und Proton-induzierten Reaktionen sowie in Schwerionenkollisionen beschreiben.

Im Rahmen dieser Arbeit wurden differentielle und integrale Produktionsquerschnitte von ω und η Mesonen in Proton-Proton Reaktionen bei 3,5 GeV Strahlenergie mit dem High Acceptance DiElektron Spectrometer (HADES) am Schwerionensynchroton des Helmholtzzentrum für Schwerionenforschung in Darmstadt gemessen. Etwa 80.000 ω Mesonen und 35.000 η Mesonen wurden rekonstruiert. Diese Statistik erlaubte die Untersuchung von Winkelverteilungen und Dalitz-Diagrammen.

ω und η Mesonen wurden im Zerfallskanal ($\pi^+\pi^-\pi^0$) in der exklusiven Reaktion $pp \longrightarrow pp\pi^+\pi^-\pi^0$ rekonstruiert. Die geladenen Teilchen im Endzustand wurden mittels deren charakteristischen Energieverlustes, durch die Messung von Flugzeit und Impuls und durch die Reaktionskinematik identifiziert. Das neutrale Pion wurde mit der "fehlende Masse"Methode rekonstruiert. Um die Massenauflösung des Rekonstruierten η Signal zu verbessern und um Ereignisse, in denen ein π^0 produziert wurde, zu identifizieren, wurde ein kinematischer Fit angewendet.

Die Korrektur der gemessenen Daten auf Effekte der Spektrometereffizienz und Akzeptanz wurde in vier Dimensionen durchgeführt (zwei Massen- und zwei Winkel-Dimensionen). Die Akzeptanz des Spektrometers für unterschiedliche Winkelverteilungen wurde mit Hilfe von umfassenden Simulationen systematisch untersucht. Die gemessenen Daten wurden auf den Querschnitt von der Proton-Proton elastischer Streuung bei dem gleichen Strahlimpuls normiert. Systematische Fehler aufgrund

der verschiedenen Algorithmen der Datenanalyse und des Untergrundabzugs wurden bestimmt.

Die Winkelverteilungen von ω und η Mesonen im Schwerpunktsystem der Reaktion wurden gemessen. Beide Verteilungen sind leicht anisotrop. Das ppω Dalitz-Diagramm zeigt einen Hinweis auf einen Produktionsmechanismus abweichend von der einfachen Phasenraumproduktion. Jedoch ist die Abweichung der gemessenen Verteilung von Phasenraumsimulationen nicht groß. Hingegen zeigt das $pp\eta$ Dalitz-Diagramm ein Signal der resonanten Produktion über die $N(1535)$ Resonanz. Etwa die Hälfte aller η Mesonen werden über die $N(1535)$ Resonanz produziert. Die Winkelverteilung von η Mesonen im Schwerpunktsystem ändert sich für resonante und nicht resonante Produktion nicht.

Der totale Wirkungsquerschnitt für die Produktion von ω Mesonen in der exklusiven Reaktion $pp \longrightarrow pp\omega$ beträgt $106,5 \pm 0,9\ (stat) \pm 7,9\ (sys)$ [μb]. Für die η Mesonen beträgt der totale Produktionswirkungsquerschnitt $136,9 \pm 0,9\ (stat) \pm 10,1\ (sys)$ [μb] in der exklusiven Reaktion $pp \longrightarrow pp\eta$.

Abstract

The study of meson production in proton-proton collisions in the energy range up to one GeV above the production threshold provides valuable information about the nature of the nucleon-nucleon interaction. Theoretical models describe the interaction between nucleons via the exchange of mesons. In such models, different mechanisms contribute to the production of the mesons in nucleon-nucleon collisions. The measurement of total and differential production cross sections provide information which can help in determining the magnitude of the various mechanisms. Moreover, such cross section information serves as an input to the transport calculations which describe *e.g.* the production of e^+e^- pairs in proton- and pion-induced reactions as well as in heavy ion collisions.

In this thesis, the production of ω and η mesons in proton-proton collisions at 3.5 GeV beam energy was studied using the High Acceptance DiElectron Spectrometer (HADES) installed at the Schwerionensynchrotron (SIS 18) at the Helmholtzzentrum für Schwerionenforschung in Darmstadt.
About 80 000 ω mesons and 35 000 η mesons were reconstructed. Total production cross sections of both mesons were determined. Furthermore, the collected statistics allowed for extracting angular distributions of both mesons as well as performing Dalitz plot studies.

The ω and η mesons were reconstructed via their decay into three pions ($\pi^+\pi^-\pi^0$) in the exclusive reaction $pp \longrightarrow pp\pi^+\pi^-\pi^0$. The charged particles were identified via their characteristic energy loss, via the measurement of their time of flight and momentum, or using kinematics.
The neutral pion was reconstructed using the missing mass method. A kinematic fit was applied to improve the resolution and to select events in which a π^0 was produced.
The correction of measured yields for the effects of spectrometer acceptance was done as a function of four variables (two invariant masses and two angles). Systematic studies of the acceptance for different input distributions were performed.
The measured yields were normalized to the number of measured events of elastic scattering. Systematic errors due to the methods of the data analysis and the background subtraction were investigated.

Production angular distributions of ω and η mesons were measured. Both mesons exhibit a slightly anisotropic angular distribution.
The Dalitz plot of ω meson production shows indications of resonant production. However, the deviation of the distribution from the one expected by phase space simulations is not large.
The Dalitz plot of η meson production shows a signal of the production via the $N(1535)$ resonance, The contribution of $N(1535)$ to the production was quantified to be about 47%. The angular distribution of η mesons does not show significant differences between resonant and non resonant production.

The total production cross section of ω mesons in the reaction $pp \longrightarrow pp\omega$ was determined to be 106.5 ± 0.9 (stat) $\pm$ 7.9 (sys) [μb] where *stat* indicates statistical error and *sys* indicates systematic error, while that of η mesons was determined to be 136.9 ± 0.9 (stat) $\pm$ 10.1 (sys) [μb] in the reaction $pp \longrightarrow pp\eta$.

Contents

List of Figures **xi**

List of Tables **xv**

1 Motivation **1**

2 The HADES spectrometer **5**

2.1 The HADES detectors 6

2.1.1 START and VETO detectors 6

2.1.2 Ring Imaging Cherenkov detector (RICH) 6

2.1.3 Magnet spectrometer 8

2.1.3.1 The Multi-wire Drift Chambers 9

2.1.4 Multiplicity Electron Trigger Array (META) 11

2.1.4.1 TOF and TOFino 11

2.1.4.2 PreSHOWER 12

2.2 Track reconstruction 13

2.2.1 Track candidate search 14

2.2.2 Momentum determination 16

2.2.2.1 Kick plane 16

2.2.2.2 Spline Method 17

2.2.2.3 Runge-Kutta method 18

3 Data analysis **19**

3.1 Track selection 20

3.2 Event ensemble 23

3.3 Particle identification and event selection 24

3.3.1 PID via characteristic energy loss 24

3.3.2 PID via mass reconstruction using time of flight 31
3.3.3 Event selection via π^0 missing mass cut 33
3.3.4 Event selection via kinematic fit p-value cut 35
3.4 The proton-proton missing mass spectrum 38

4 Kinematic fit **41**
4.1 Introduction 41
4.1.1 The error matrix 43
4.2 Results 45
4.2.1 Pull distributions 45
4.2.2 p-value distributions 48
4.2.3 Missing mass spectra 50
4.3 Conclusion 55

5 Acceptance correction **57**
5.1 Steps of acceptance determination 58
5.1.1 Event generation 58
5.1.2 Detector simulation 58
5.1.3 Particle reconstruction 58
5.1.4 Acceptance matrix 59
5.2 Model dependent acceptance correction 59
5.2.1 Acceptance holes 59
5.2.2 Degrees of freedom (DOF) 60
5.2.2.1 Chosen DOF 61
5.3 The HADES acceptance 62

6 Acceptance studies **67**
6.1 Studies of ω meson production 67
6.1.1 SimCos8: strong anisotropic distributions 68
6.1.2 SimCos2: slightly anisotropic distributions 71
6.2 Studies of η meson production 72
6.3 Conclusion 76

7 Cross section determination and absolute normalization 79
7.1 Downscaling factor . . . 79
7.2 Branching ratio . . . 80
7.3 Normalization to the elastic cross section . . . 80
7.3.1 Determination of the elastic normalization factor . . . 81
7.3.1.1 Determination of N_{acc}^{el} . . . 81
7.3.1.2 Determination of σ_{acc}^{el} . . . 83
7.4 Relative trigger efficiency . . . 84
7.4.1 Trigger efficiency of TOF/TOFino scintillators . . . 84

8 Yield determination and systematic errors 87
8.1 Background subtraction and yield determination . . . 87
8.2 Systematic errors . . . 89
8.2.1 π^0 missing mass cut . . . 89
8.2.2 The kinematic fit p-value cut . . . 91
8.2.3 Background subtraction . . . 93

9 Results 95
9.1 η meson . . . 95
9.1.1 Dalitz plot . . . 95
9.1.2 Angular distribution . . . 100
9.2 ω meson . . . 102
9.2.1 Dalitz plot . . . 102
9.2.2 Angular distribution . . . 107
9.3 Summary and conclusion . . . 108

10 Zusammenfassung 109
10.1 Motivation . . . 109
10.2 Datenanalyse . . . 110
10.3 Akzeptanzkorrektur und Normierung . . . 111
10.4 Resultate . . . 112

References 117

A Acceptance plots 121

B Angular distributions **127**

B.1 proton angular distribution in the reaction $pp \longrightarrow pp\eta$ 127

B.2 proton angular distribution in the reaction $pp \longrightarrow pp\omega$ 129

B.3 η meson angular distribution 131

List of Figures

1.1 e^+e^- invariant mass spectrum in Ar+KCl collisions at 1.76 AGeV . . 3
1.2 Diagrams contributing to the ω meson production in proton proton reactions 4

2.1 The HADES spectrometer 5
2.2 View of the RICH detector 7
2.3 Working principle of the magnet spectrometer 8
2.4 Dimensions of the drift chamber 9
2.5 Orientation of the wire layers of the drift chambers 10
2.6 View of the time-of-flight detectors (TOF and TOFino) 12
2.7 Schematic presentation of the PreSHOWER detector 13
2.8 Principle of the *track candidate* search 14
2.9 Projection of fired drift cells 15
2.10 Spline method for momentum reconstruction 17

3.1 Analysis steps 19
3.2 χ^2 distributions of segment and track fits 22
3.3 pp missing mass for three track samples 23
3.4 Energy loss versus momentum 25
3.5 Distribution of deposited energy (-ve tracks) 26
3.6 Results of Landau fit (-ve tracks) 27
3.7 π^+ dE/dx selection 28
3.8 Distribution of deposited energy (+ve tracks) 29
3.9 Results of Landau fit (protons) 30
3.10 π^+ and proton dE/dx selection 30
3.11 Distribution of mass reconstructed using tof and momentum 32
3.12 Energy loss of pions and protons identified via tof-momentum PID . . 33

3.13 Missing mass distribution 34
3.14 Energy loss of pions and protons identified via missing mass cut . . . 35
3.15 p-value distribution all events 36
3.16 Energy loss of pions and protons identified using kinematic fit 38
3.17 pp missing mass for events selected via π^0 missing mass cut 39
3.18 pp missing mass for events selected via kinematic fit p-value cut . . . 40

4.1 Correlation of the errors of the measured track parameters 44
4.2 Pull distributions of protons in real data 46
4.3 Pull distributions of protons in simulated data 47
4.4 p-value distribution all events 48
4.5 p-value distribution simulation 49
4.6 missing mass spectra with no p-value cut 51
4.7 missing mass spectra with p-value cuts 53
4.8 missing mass spectra with p-value and π^0 missing mass cuts 55

6.1 SimCos8: ω angular distribution 69
6.2 SimCos8: ω angular distribution (selected range) 70
6.3 SimCos8: proton angular distribution 70
6.4 SimCos2: ω angular distribution 71
6.5 SimCos2: ω angular distribution (selected range) 72
6.6 SimCos2: proton angular distribution 72
6.7 Angular acceptance for η 73
6.8 SimCos8-η: Angular distributions 74
6.9 SimCos2-η: Angular distributions 75
6.10 ω: Acceptance as a function of Dalitz masses versus production angle 76
6.11 η: Acceptance as a function of Dalitz masses versus production angle 77

7.1 Distribution of elastic events 82
7.2 Simulation of elastic events 82
7.3 Proton-proton elastic cross section 83
7.4 TOFino ADC spectrum 85

8.1 pp missing mass in backward and forward directions 88
8.2 $pp\pi^+\pi^-$ missing mass distribution 90
8.3 $pp\pi^+\pi^-$ missing mass for events accepted by the kinematic fit 91

8.4 pp missing mass distribution with and without kinematic fit 92

9.1 Dalitz plot η 96
9.2 N_η as a function of $M^2_{p\eta}$ 97
9.3 Momentum distributions η 98
9.4 Momentum distributions η 99
9.5 Angular distribution of η for resonant and non resonant production . 100
9.6 Integrated angular distribution of η 101
9.7 Dalitz plot ω 103
9.8 N_ω as a function of $M^2_{p\omega}$ 104
9.9 Momentum distributions ω 105
9.10 Ratio of N_ω in real data to simulations as a function of $M^2_{p\omega}$ 106
9.11 Angular distribution of ω 107

10.1 Energieverlust von Pionen und Protonen die mit dem "π^0 fehlende Masse" Schnitt identifiziert wurden 110
10.2 Proton-Proton fehlende-Masse-Spektrum mit und ohne kinematischen Fit 111
10.3 Produktionswinkel und Protonenwinkel 112
10.4 Winkelverteilung von η und ω Mesonen 113
10.5 $pp\omega$ und $pp\eta$ Dalitz-Diagramme 115

B.1 Proton angular distribution: $pp \longrightarrow pp\eta$ 128
B.2 Proton angular distribution: $pp \longrightarrow pp\omega$ 130
B.3 η meson angular distribution: $pp \longrightarrow pp\eta$ 132

List of Tables

2.1 Dimensions of the drift chamber 9
2.2 Angle of the wires of the wire layers. 10
2.3 Properties of the wires used in the drift chambers 11

3.1 The three event hypotheses 23
3.2 Number of remaining events/hypotheses after dE/dx selection 31
3.3 Number of remaining events/hypotheses after π^0 selection 34
3.4 Number of remaining events/hypotheses after dEdx + π^0 selection . . 36
3.5 Number of remaining events/hypotheses after kinematic fit 37
3.6 Number of remaining events/hypotheses after dE/dx selection and kinematic fit 38

5.1 Selected DOF 61
5.2 Acceptance plots for η 63
5.3 Acceptance plots for ω 65

8.1 Number of reconstructed η mesons at different p-value cuts 92

A.1 Acceptance plots for η 121
A.2 Acceptance plots for ω 124

B.1 Results of the fit to the proton angular distribution in the reaction $pp \longrightarrow pp\eta$ 129
B.2 Results of the fit to the proton angular distribution in the reaction $pp \longrightarrow pp\omega$ 129
B.3 Results of the fit to the η meson angular distribution 131

1

Motivation

The **H**igh **A**cceptance **DiE**lectron **S**pectrometer HADES is a multi-purpose device installed at the Schwerionen-Synchrotron SIS 18 at the Helmholtzzentrum für Schwerionenforschung GSI in Darmstadt, Germany. The HADES collaboration has a manifold program for studying light meson production in proton, pion, and ion induced reactions with nuclei ranging from hydrogen up to gold. One of the main pillars of the HADES physics program is the study of the chiral symmetry restoration in moderately dense and hot nuclear medium.

Quantum Chromo Dynamics (QCD) is the basic theory describing the strong interaction. According to QCD, the heavy composite particles called hadrons are built of quarks (point like objects carrying electric and color charges). The strong force between quarks couples to the color charge and is mediated via gluons. The chiral symmetry is a fundamental symmetry of the QCD Lagrangian with massless quarks. The fact that constituent quarks are not massless is related to the spontaneous breaking of chiral symmetry.

The chiral symmetry breaking leads to a finite expectation value of the quark condensate in vacuum. However, theoretical calculations predict the expectation value of the condensate to drop inside a nuclear medium with increasing nuclear density until it vanishes at densities higher than three to fives times the normal nuclear matter density.

Such models also expect the mass of vector mesons (ρ, ω, and ϕ) to decrease with decreasing value of the condensate. Hence, a measurement of lower masses of vector mesons inside a nuclear medium compared with their measured vacuum masses could be interpreted as a sign for the restoration of the chiral symmetry.

Only those mesons which decay inside the medium can exhibit the expected mass modification.Those which leave the medium have by definition the vacuum properties. Accordingly, the life time of the produced mesons and their velocity distribution relative to the nuclear medium define the fraction which decays inside the medium.

The reconstruction of mesons via their hadronic decay channels can not be used to judge on a possible modification of spectral functions since the decay products react strongly with the nuclear medium and thereby the spectral information can be distorted. Leptonic decay products, on the other hand, leave the nuclear medium without interaction (apart from the negligible electromagnetic interaction), and hence reach the detector carrying the original information about the decay inside the medium. Here, the experimental difficulty arises: The branching ratios of vector mesons for leptonic decays are several orders of magnitude lower than those of hadronic decay channels. Because of this reason, HADES possesses a dedicated detector for the online identification and triggering on electrons (and positrons), the **R**ing **I**maging **Ch**erenkov detector RICH (see chapter 2). Using the RICH for online triggering, HADES is able to enrich the sample of collected events with events in which electrons and positrons are produced.

Figure 1.1 shows the inclusive e^+e^- invariant mass spectrum for events of Ar+KCl reactions at a beam kinetic energy of 1.76 GeV per nucleon [Kri10]. The solid line in the figure shows the spectrum obtained using calculations based on a transport model (HSD). The various colored lines show different components which contribute to the calculated total yield. Note that beyond 650 MeV/c^2 e^+e^- pairs from vector meson decays dominate the spectrum.

As can be seen in figure 1.1, many sources contribute to the finally observed e^+e^- invariant mass spectrum. These are mostly Dalitz decays of mesons and baryon resonances. Drawing a conclusion on possible in medium modifications of vector meson spectral functions based on the mere comparison between measured data and theoretical calculations is in such a case very difficult. To improve this situation, the HADES collaboration collected data on proton-proton and proton-niobium reactions at the same beam energy of 3.5 GeV. The idea is to compare the shapes of the experimentally measured spectrum in the ω meson mass region in both data sets. By doing that, experimental and systematic uncertainties affect less the final interpretation of a possible change in the spectral function. The results of analyzing the e^+e^-

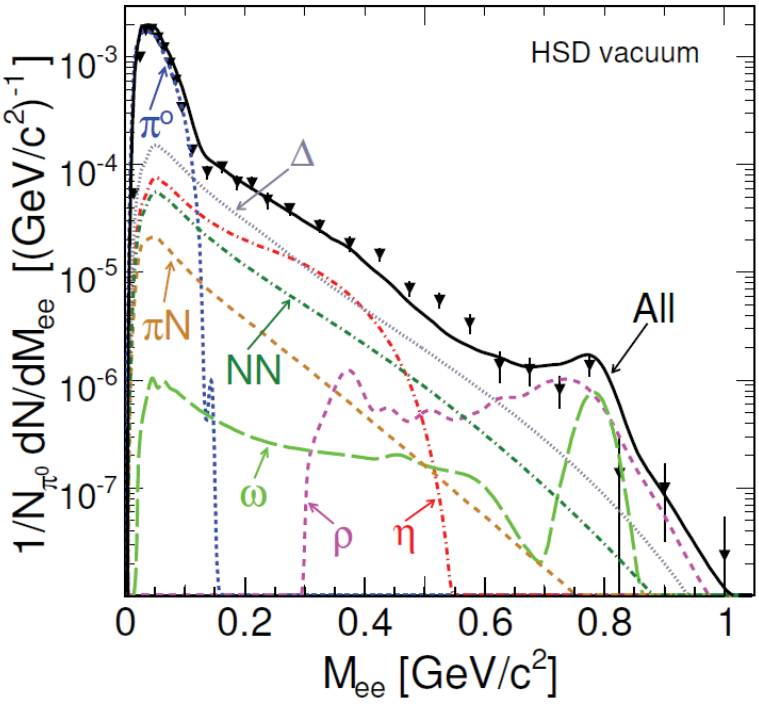

Figure 1.1: The efficiency corrected e^+e^- invariant mass spectrum from the Ar+KCl run compared to the HSD cocktail which assumed vacuum behavior of spectral functions for ρ^0 and ω mesons.

production in proton-proton data can be found in [Tar10] and in proton-niobium data in [Web11].

Differential cross sections of η/ω are needed by theoretical models to describe the e^+e^- invariant mass spectrum as shown in figure 1.1. However, the collected number of ω mesons in the decay channel e^+e^- is less than 300. It is not possible to do differential studies using such low statistics. For that, the decay channel of ω with the highest branching ratio was selected ($\omega \longrightarrow \pi^+\pi^-\pi^0$ BR: 89.2%). Note that the η meson decays into the same channel with a branching ratio of 22.7%.

Moreover, differential cross sections of light mesons provide valuable information about the nature of the nucleon-nucleon (NN) interaction. Light mesons, including the η and ω mesons, are used in One Boson Exchange models (OBE) as a mediator of the nucleon-nucleon force. OBE are also used to describe the meson production in nucleon nucleon collisions. Figure 1.2 shows the graphs included by Nakayama *et. al.* [NSH$^+$98] within a boson exchange model in a study of ω meson production in proton-proton reactions up to incident beam energies of 2.2 GeV. It has been shown

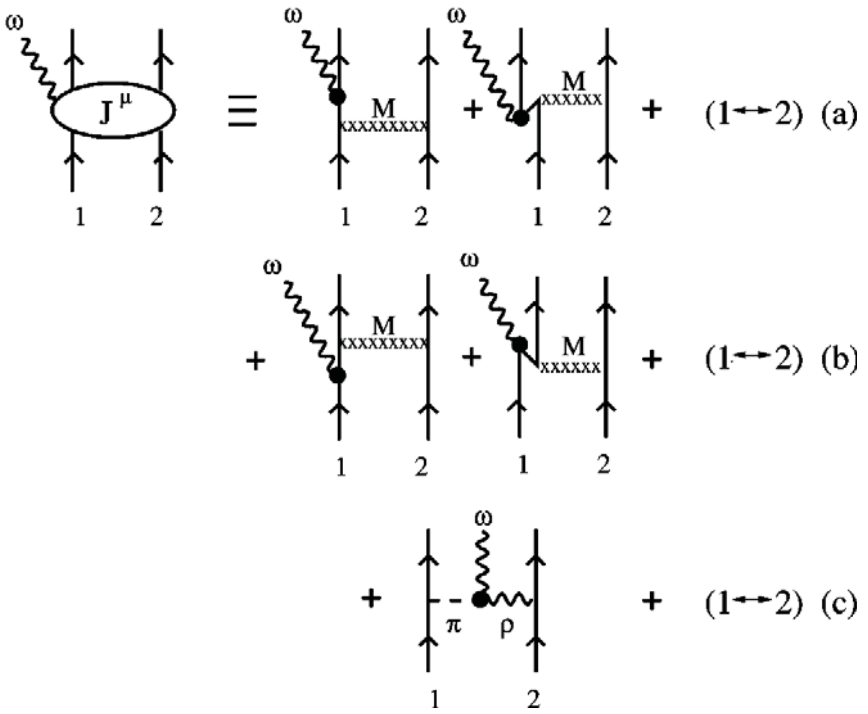

Figure 1.2: ω-meson production currents. (a) and (b) are the nucleonic current, and (c) is the meson exchange current. $M = \pi, \eta, \rho, \omega, \sigma, a_0$.

that nucleonic (a and b) and mesonic (c) currents lead to very different angular distributions of the produced ω in the center of mass frame[1]. Therefore, measuring the angular distribution provides valuable information about the magnitude of the individual contributions to the production process. Furthermore, Dalitz plots provide direct information about the contribution of nucleon excitations to the production process. The two items described in the last paragraphs are the subject of this thesis.

[1]It is worth mentioning that the extension of this model to beam energies in the range of 3.5 GeV is not straightforward [Nak10].

2

The HADES spectrometer

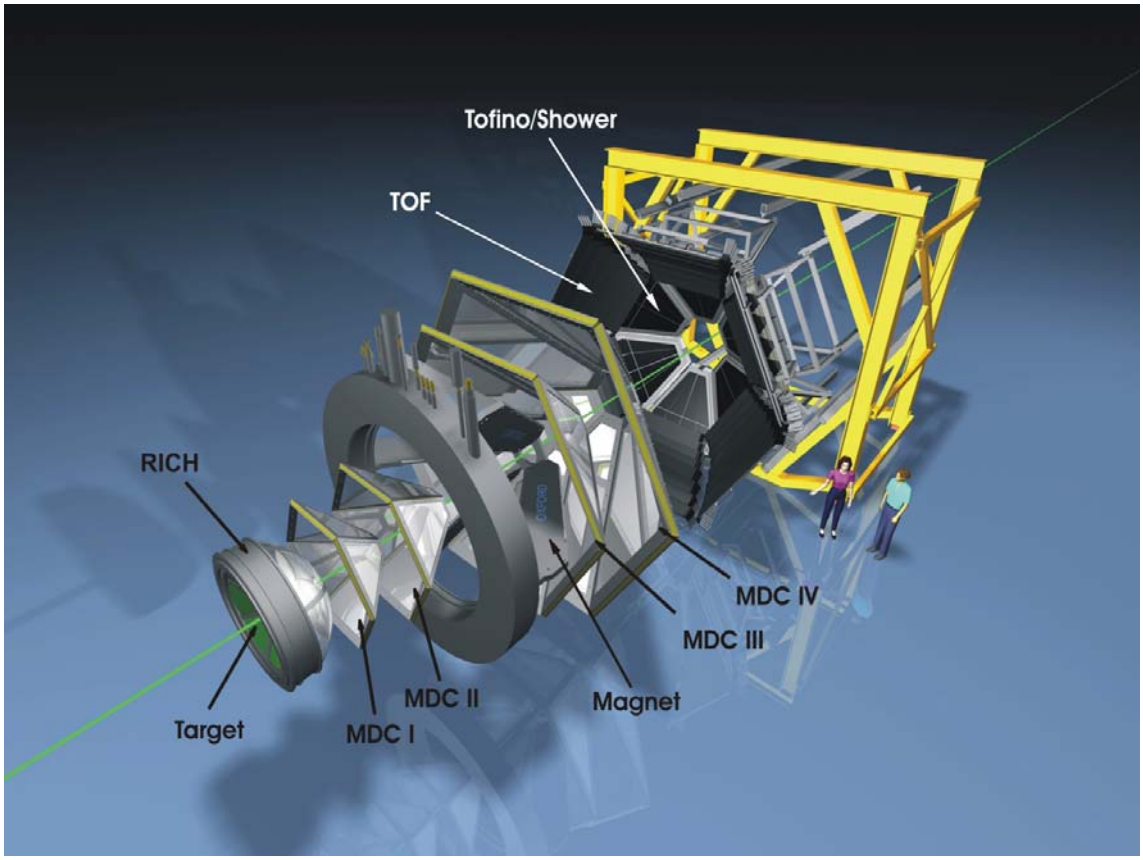

Figure 2.1: 3-dimensional exploded view of the HADES spectrometer.

The HADES spectrometer consists of the following sets of systems:

- START and VETO detectors

- **R**ing **I**maging **Ch**erenkov detector (RICH)
- Magnet
- **M**ulti-wire **D**rift **C**hambers (MDC)
- **T**ime **O**f **F**light detectors (TOF and TOFino)
- Pre-Shower detector

In the following section[1], the different systems mentioned above are briefly described. The algorithms used in the reconstruction of particle trajectories and momenta are briefly presented in section 2.2[2]. A more detailed description of the detectors and algorithms and their performance can be found in [A+09].

2.1 The HADES detectors

2.1.1 START and VETO detectors

The START and VETO detectors, are two identical diamond detectors placed 75 cm in front of and behind the target respectively. They operate in an anti-coincidence logic, such that when a beam particle detected by the START detector, passes through the target without interaction, the particle is detected by the VETO detector as well, and the corresponding event is discarded. The detectors have a size of $25 \times 15\, mm$, and a thickness of 100 μm to reduce the effect of multiple scattering and the production of secondary particles. The START detector provides the time of a reaction in the target with a precision of 50 ps.
The START detector was not included in the setup during the collection of proton-proton interaction data analyzed in this work.

2.1.2 Ring Imaging Cherenkov detector (RICH)

When a charged particle passes through a medium of refractive index n with a velocity $\beta > 1/n$, it emits Cherenkov radiation. The radiation is emitted when a charged particle moves through a medium with a velocity greater than the phase

[1] Parts of my dipolma thesis "A new method for the time calibration of the HADES drift chambers" [Tei07]

[2] Selected parts of [A+09]. References therein.

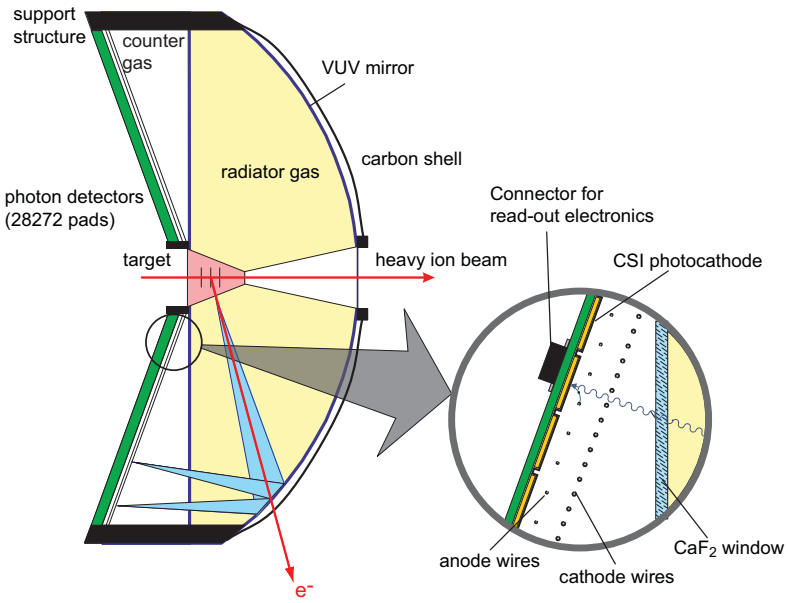

Figure 2.2: Schematic representation of the RICH detector.[B̈99].

velocity of light in the medium. The particle polarizes the surrounding medium creating dipoles. At these high velocities, the polarization is not symmetric, but mainly focused in the direction of particle movement. A coherent radiation is emitted on a defined light cone (Cherenkov radiation).

The threshold for the emission of Cherenkov radiation in the C_4F_{10} radiator gas used in the RICH detector is $\gamma_{thresh} = 18.3$. Hadrons emitted in reactions at the SIS energies of 2 $AGeV$, have a maximum γ value of 10. Therefore they are not detected by the RICH. e^-e^+ with energies above 10 MeV produce Cherenkov radiation in the RICH. Hence, the RICH detector can be used for a *real-time* lepton identification in HADES.

Electrons moving through the RICH produce Cherenkov light in a cone along their trajectories. The light is reflected by the aluminized carbon fiber mirror, and is focused as an elliptical image on the position sensitive photon detector. The photon detector is separated by a 5 mm thick CaF_2 window from the radiator volume. It is composed of three multi wire proportional chambers with a segmented photocathode. The Cherenkov light releases photoelectrons from the photo cathode, inducing an electric signal on the photocathode in one or more pads.

2.1.3 Magnet spectrometer

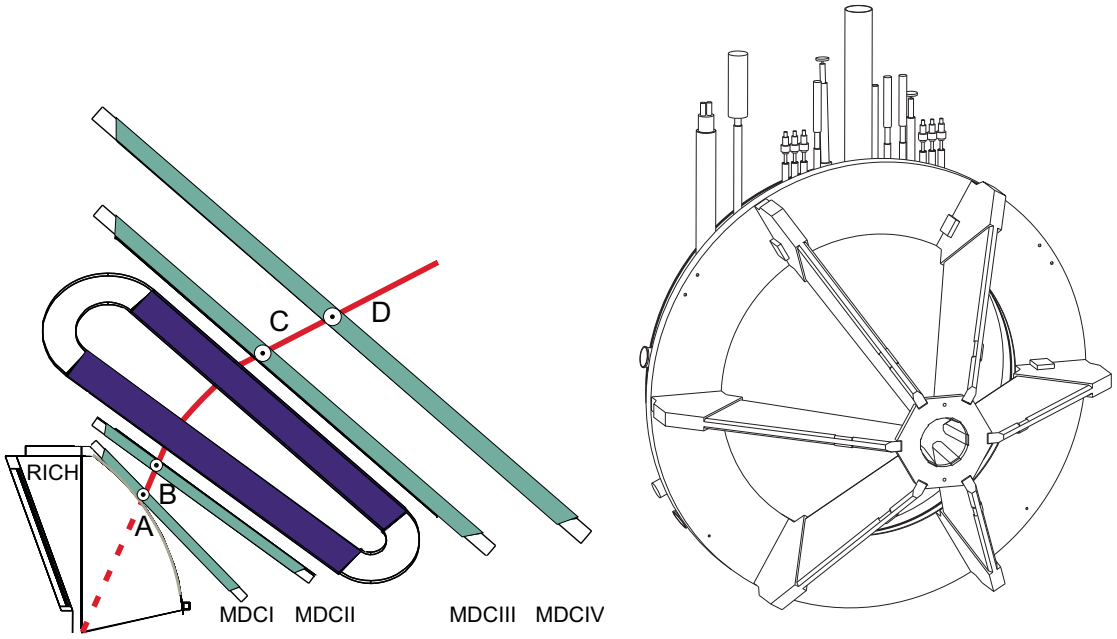

(a) (b)

Figure 2.3: (a) Working principle of the magnet spectrometer [Lip00]. The momentum of a charged particle can be determined from the bending angle of the particle trajectory inside the magnetic field, if the field strength is known. (b) View of the magnet of the HADES spectrometer.

The magnet of the HADES experiment is composed of 6 super conducting toroidal coils arranged around the beam axis. The maximum electrical current of the magnet is 3665 A, at a temperature of 4.6 K. The magnetic field strength reaches, 3.7 T inside the coils, 2.4 T near the coils, and $\sim$ 0.8 T in the middle between two coils. The magnet of the HADES experiment has to fulfill the following requirements:

- High geometrical acceptance. The magnet coils have to be compact to minimize the dead regions of the detector.
- The magnetic field strength in the region of RICH and MDC's has to be kept as low as possible.

- Acceptance of particles with a large momentum range, within a large solid angle.

Together with the MDC's, the magnet of the HADES experiment constitutes the tracking system of HADES.

2.1.3.1 The Multi-wire Drift Chambers

The HADES multi-wire drift chambers are arranged in four planes, two planes in front of the magnet and two planes behind the magnet. Each plane is divided into six identical trapezoidal drift chambers (MDC's). Each MDC covers one sector of the spectrometer. Hence, the total number of drift chambers in the spectrometer is 24.

The dimensions of the trapezoidal chambers of the four planes range from ca.

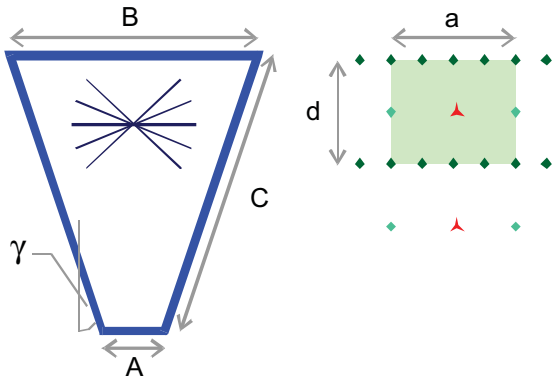

Figure 2.4: Dimensions of the drift chamber [Str98].

Plane no.	A $[mm]$	B $[mm]$	C $[mm]$	γ $[°]$	a $[mm]$	d $[mm]$	Area $[m^2]$	Volume $[l]$
I	139,21	767,38	839,19	21,98	5	5	0,34	11,99
II	205,00	905,00	1049,27	19,49	6	5	0,49	20,58
III	310,43	1804,80	2139,05	20,44	12	8	1,88	150,4
IV	345,46	2224,05	2689,04	20,44	14	10	2,83	197,8
per sector							5,54	380,77
Total							33,24	2284,62

Table 2.1: Dimensions of the drift chamber [Str98]

77×84 cm^2 (figure 2.4), for the most inner plane, up to 222×269 cm^2 for the most

outer plane. Table 2.1 shows the dimensions and sizes of the different chambers, and the cell dimensions for each of them.

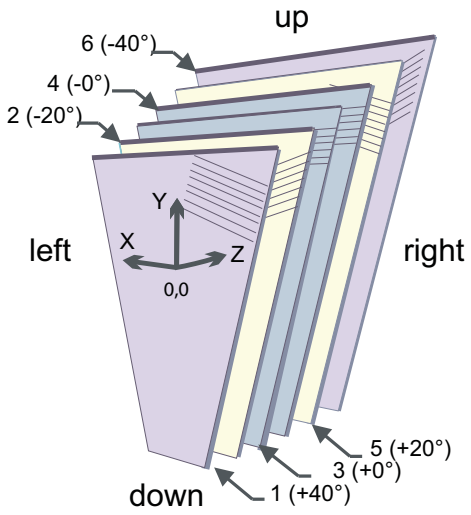

Figure 2.5: Orientation of the wire layers of the drift chambers.

	Angle [°]
Layer 1	+ 40
Layer 2	- 20
Layer 3	+ 0
Layer 4	- 0
Layer 5	+ 20
Layer 6	- 40
Cathode layers	90

Table 2.2: Angle of the wires of the wire layers.

Each drift chamber is composed of 6 field/signal wire layers, which are surrounded by two cathode wire layers. A drift cell is built from one signal wire, the two neighboring field wires, and the cathode wires of the two surrounding cathode layers.

As shown in figure 2.5, the wires of each layer are oriented at a different angle relative to the coordinate system of the chamber. The angles of the field/signal layers vary between $+40\,°$, $-20\,°$, $+0\,°$, $-0\,°$, $+20\,°$ and $-40\,°$, where the sign defines the direction of the rotation of the wires (see table 2.2). The two $\pm 0\,°$-layers are shifted, relative to each other, by an amount equal to one half of the width of a drift cell. The wires of all cathode layers are oriented at an angle of $90\,°$ relative to the chamber coordinate system.

The distances between the cathode and signal layers, and between the signal and field wires, define the dimensions of the drift cells for the different chamber planes. These dimensions range from $5 \times 5\,mm^2$, for the most inner plane (MDC-I), up to $14 \times 10\,mm^2$, for the most outer plane (MDC-IV) (see figure 2.4 and table 2.1).

Table 2.3 shows the properties of the different wires used in the chambers. In addition, the entrance and exit windows of the chambers are built using $12\,\mu m$

	Material	Diameter [μm]	
Cathode wires	Aluminium (Al)	80_{I-III}	100_{IV}
Field wires	Aluminium (Al)	80_{I-II}	100_{III-IV}
Signal wires	Gold plated Tungsten (Au/W)	20_{I-III}	30_{IV}

Table 2.3: Properties of the wires used in the drift chambers. Indices indicate the different planes.

Mylar foils coated with Aluminium [Gar98]. The materials were chosen to minimize the effect of multiple scattering of the particles on the momentum resolution of the tracking system.

2.1.4 Multiplicity Electron Trigger Array (META)

The META consists of the two time-of-flight systems TOF and TOFino covering the whole HADES acceptance, as well as the Pre-Shower system at polar angles $\theta < 45°$. It is used for particle identification and online event selection purposes based on the multiplicity of particles (multiplicity trigger).

2.1.4.1 TOF and TOFino

The TOF detector is used to measure the time-of-flight of particles from the target to the TOF itself. It is arranged in 6 sectors, each is composed of 8 modules. Each module in the TOF detector consists of 8 plastic scintillation rods, and a **P**hoto **M**ultiplier **T**ube (PMT) at each end of the rod. When hit by a particle, the scintillation rod provides a light signal which is collected at both ends by the PMT's, and is converted to a time signal using a TDC (**T**ime to **D**igital **C**onverter). Using the time information from both ends, one can calculate the time-of-flight of the particle and the position of the hit in the rod.

The TOF detector covers the polar angular range $44 < \theta < 88$. For $\theta < 45$ the TOFino detector is used to provide the time-of-flight information. The TOFino detector is similar to the TOF, nevertheless with a lower granularity. It is divided into 6 sectors, each sector composed of 4 scintillator paddles arranged radially around the beam axis (see figure 2.6). The scintillator light in the TOFino detector is collected only at one end of the paddle. Therefore, the position information of the particle hit cannot be obtained using the TOFino system alone. Only after the

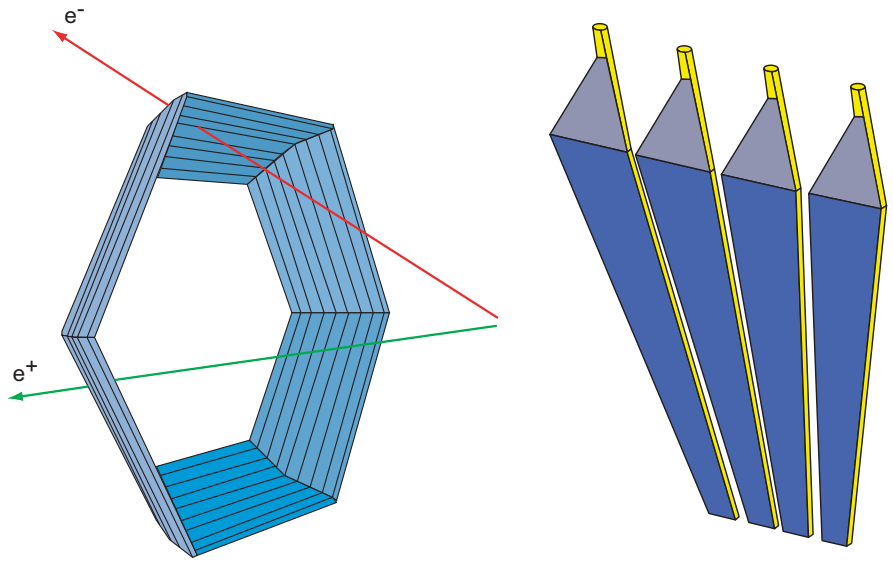

(a) (b)

Figure 2.6: Schematic view of (a) the TOF detector and (b) one sector of the TOFino detector.

correlation with the information from the PreSHOWER detector, the particle hit position can be determined.

2.1.4.2 PreSHOWER

The PreSHOWER detector is mounted behind the TOFino detector and covers the range of polar angle $18 < \theta < 45$. It is divided into 6 sectors, each of them consisting of three nearly identical multi wire chambers *(pre-converter, post 1, post 2)* (figure 2.7). Two lead converters of 1.12 *cm* and 0.84 *cm* thickness are placed between the three wire chamber. Each wire chamber is composed of one cathode layer, one wire layer, and another segmented cathode layer. The wire layer consists of alternating anode and cathode wires. The chambers are filled with an $Argon/i-butane/heptane$ gas mixture and are operated at a cathode potential of -3200 V.

Relativistic charged particles passing through the lead converter emit photons through *bremsstrahlung*. The emitted photons can convert to e^+e^- pairs by the process of pair production. If the conversion products have enough energy, they can undergo the same process as the primary particle. At the end a *shower* of

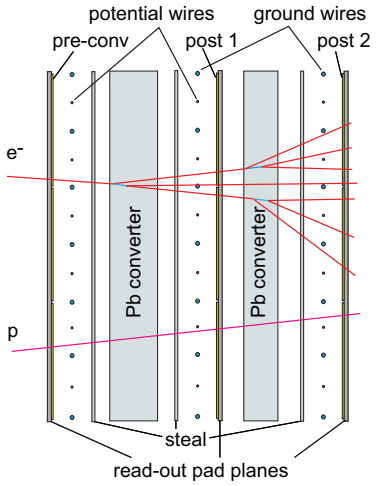

Figure 2.7: Schematic representation of the PreSHOWER detector.

electrons and positrons is created (see figure 2.7). The charged particles passing through the wire chambers ionize the molecules of the counting gas. The electrons produced by ionization move towards the anodes of the chamber where they get multiplied by an avalanche process. The avalanche results in a positive signal on the neighboring pads of the segmented cathode layer which is readout by the electronics. Through a comparison between the detected charges in the different chambers, one can deduce if a shower has been produced. In the range of energies provided by the SIS only leptons produced in a heavy ion collision will have enough energy to produce a shower. The heavy hadrons instead, have a very small probability of emitting bremsstrahlung and hence producing a shower.

2.2 Track reconstruction

The reconstruction of the particle trajectories in the tracking system of HADES is accomplished in several steps:

1. The spatial correlation of fired drift cells in the drift chambers (MDCs) is performed by a *track candidate* search (sect. 2.2.1) based on the identification of socalled *wire clusters*. The wire clusters are defined using only the geometrical positions of the fired drift cells and define *track segments*. *Track candidates*

are finally obtained through the matching of track segments in the inner and outer drift chambers within one sector.

2. The corresponding space positions of the *track candidates* are fitted by a model function taking into account the drift time information of the cells (see sect. 2.2.1).

3. The particle momentum is determined by various algorithms making use of the bending of its trajectory inside the magnetic-field region (see sect. 2.2.2).

2.2.1 Track candidate search

The *track candidate* search is based on the projection of the area of fired drift cells along a certain direction onto a common projection plane and the localization of maxima in this plane. The projection plane chosen (see fig. 2.8) is the center plane of two coplanar outer chambers, while for the non-coplanar inner geometry the plane is chosen such that the projections of the drift cells are of similar size. For the inner

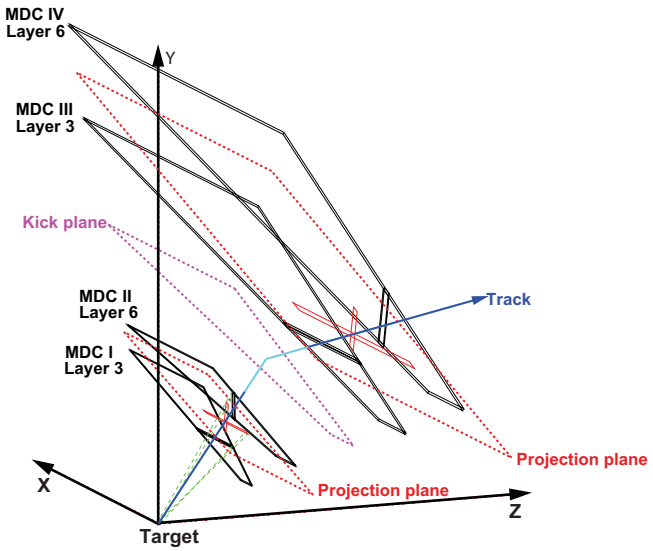

Figure 2.8: Principle of the *track candidate* search in the track reconstruction procedure. For an easy view, only one layer is shown in each MDC.

drift chambers the projection is performed with respect to the center of the target.

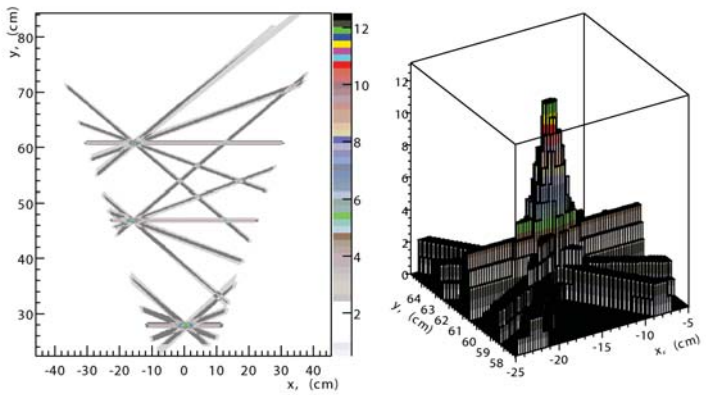

Figure 2.9: Left: $x - y$ detector coordinate space projection of the drift cells in the cluster finding procedure. Right: 2-dimensional histogram with a peak at the location where the drift cell projections have maximum overlap. In this example, the z-axis indicates the peak height, corresponding here to a track totaling 12 hit layers in the inner drift chambers.

Here, only the extension of the target along the beam axis is taken into account. The impact point of the track on the projection plane is given by the local maximum of two-dimensional distributions built from the slices spanned by fired drift cells, as shown in fig. 2.9. To reduce the number of fake candidates created by accidentally crossing hit wires, all fired drift cells belonging to either one or both inner chambers are simultaneously projected onto one plane. The target position and the location of the maximum in the projection plane then define a straight track segment in space.

The deflection of a charged particle by the toroidal magnetic field of the HADES magnet can be approximated by a momentum kick on a nearly flat virtual *kick plane*. in the field region (see sect. 2.2.2.1). Hence, when searching for wire clusters in the outer drift chambers, the same strategy is followed as for the inner ones, except that the target position is replaced by the intersection point of an inner segment with the virtual momentum kick plane. This inherent matching of inner and outer segments defines a *track candidate*. This is shown in fig. 2.8 which depicts a schematic representation of the candidate search. Note that this procedure neglects the additional deflection due to weak fringe fields reaching into the MDC volumes.

The spatial resolution of the *track candidate* search is defined by the wire spacing. The stereo angles of the wire planes have been optimized for best resolution in the

direction of particle deflection. Thus, the position resolution is worse along the x-coordinate of the chamber than on the y-coordinate. For the inner drift chambers the resolution along the x-coordinate is 1.12-1.5 mm and along the y-coordinate 0.8-1 mm. Due to their larger cell size, the resolution in the outer drift chambers is 3.9-4.8 mm and 2.9-3.3 mm in x and y directions, respectively.

The precision of the reconstructed hit points in space is improved from a few mm down to typically 0.1-0.2 mm by making use of the drift time measurement and by fitting the space coordinates of the track to a track model. This requires converting a measured drift time into a distance to the sense wire. The distance to time correlation for each drift cell geometry ($x - t$ correlation) was obtained from GARFIELD [GAR] simulations and checked against test measurements.

2.2.2 Momentum determination

The HADES data analysis employs three different momentum reconstruction algorithms. The *kick plane* method provides a fast and robust estimate of the particle momentum with limited resolution using reconstructed inner track segments and hit points on the META detector only. With better precision, as well as moderate computational requirements, the *spline* method obtains the particle momentum from matched reconstructed inner and outer *track segments*. Finally, the *Runge-Kutta* method provides the best precision in reconstructing the particle momentum, but requires more computational resources. Whereas *kick plane* can provide a momentum at order zero in case of no outer MDCs, *Spline* and *Runge-Kutta* are the standard methods to reconstruct the momentum. *Spline* provides first guess momentum and particle polarity which are then used for the iterative *Runge-Kutta*. All three momentum algorithms are applied from the lowest to the highest precision level, each step providing a starting value for the next one with the needed accuracy. The results of all algorithms are stored in parallel, allowing for a detailed monitoring of the procedure.

2.2.2.1 Kick plane

Schematically, the progressive deflection of a charged particle on its way through the toroidal field of the HADES magnet can be substituted by a single kick occurring on a two-dimensional, almost flat virtual surface, called kick plane. This surface is determined in ray-tracing simulations using GEANT3 and corresponds roughly

to the center plane of the magnetic field in any given sector of HADES. Within the *kick plane* approach, the momentum p of a deflected particle is obtained in a straightforward way from its deflection angle via pre-computed look-up tables. This approach provides a very fast initial value of p, to be used as starting point in more refined track fitting algorithms.

2.2.2.2 Spline Method

In the framework of spline momentum reconstruction method, a cubic spline is taken as a model for the particle trajectory through the magnetic field. The spline provides a smooth curve passing through the detector hit points, as well as smooth first- and second-order spatial derivatives at the given hit points. As an input, this algorithm employs *track candidates* containing inner and outer track segments. They are used to calculate intersection points of the reconstructed segments with the chamber mid-planes. Using four such intersection points in space, a cubic spline function in the $(z, r = \sqrt{x^2 + y^2})$-plane is applied. Fifty equally spaced points are selected and the corresponding derivatives are calculated. The magnetic-field strength is computed at the selected points using the three-dimensional HADES magnetic-field map (see fig. 2.10).

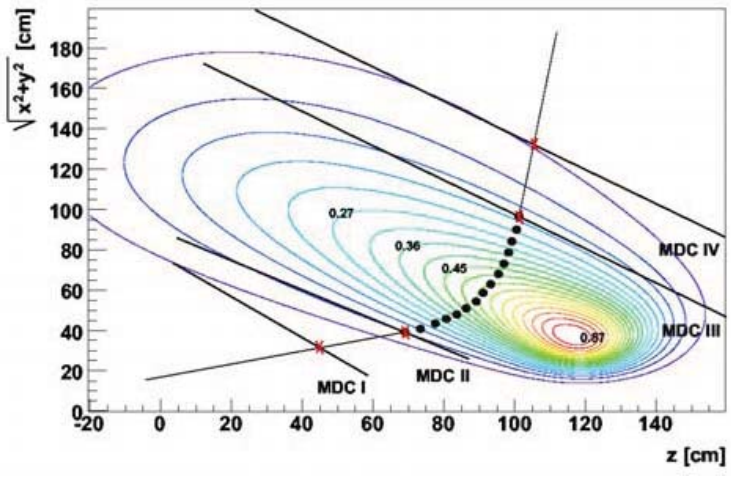

Figure 2.10: The track as modelized by a cubic spline in the plane defined by the three-momentum at the target and the beam axis. The 50 points (only 15 are shown here for clarity) run from MDCII up to MDCIII.

2.2.2.3 Runge-Kutta method

The standard method to determine the momentum of a particle traversing a known magnetic field consists in solving its equations of motion in the field region. In general, the system of second-order differential equations is handled by the fourth-order Runge-Kutta method of Nystrom in a recursive way with adaptive step size. The numerical solution of a differential equation requires, however, initial conditions of the function and its first derivatives, provided in our track reconstruction by the spline method (momentum and polarity) and the track-segment fitter (vertex and direction). The track parameters -$x, yatz = 0$ and two direction cosines in the MDCI chamber coordinate system and the momentum p- are iteratively optimized to fit to the hit points measured in the MDCs.

3

Data analysis

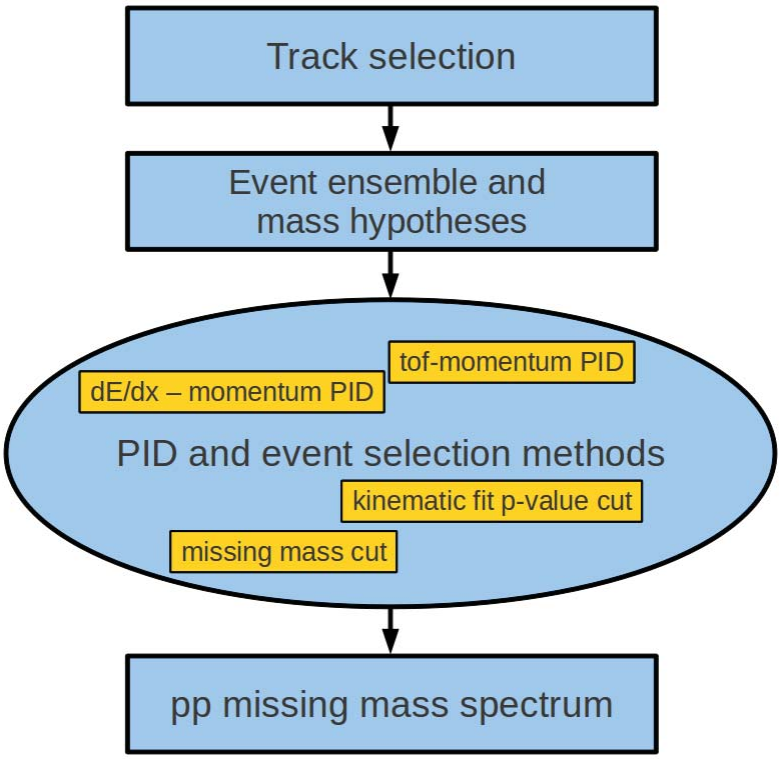

Figure 3.1: The steps of the data analysis. The algorithms indicated in step 3 include two particle identification (PID) methods which may or may not be applied in combination with one of the two event selection methods (missing mass or kinematic fit p-value cut).

In this work, data from proton-proton reactions at 3.5 GeV beam kinetic energy

were analyzed with the goal to prepare a clean sample of $pp \longrightarrow pp\eta/\omega$ events. During the experiment about 1.77×10^9 events were collected. Out of this number, about 1.17×10^9 events were triggered by the M3 minimum bias trigger which requires at least three charged particles to hit the META detector. From these M3 triggered events we obtain the ensemble of events used for the analysis by requiring four fully reconstructed charged particle tracks in the detector.
In exclusive studies, the number of particles produced is essential to decide whether an event possibly belongs to a specific reaction channel. Therefore, the first step in the exclusive analysis is to define the criteria for accepting a reconstructed particle trajectory in order to determine the number of particles produced in each event.
In section 3.1 the selection of reconstructed particle trajectories is presented. In the following sections, the building of the real event ensemble and setting up of mass hypotheses (section 3.2) as well as the different methods for the verification of event and mass hypotheses (section 3.3) are discussed. Finally (section 3.4), the pp missing mass spectrum (in the reaction $pp \longrightarrow pp + missing\ mass$) is shown. For the events under study, the pp missing mass is equivalent to the invariant mass of $\pi^+\pi^-\pi^0$. The production of ω and η mesons and their subsequent decay into $\pi^+\pi^-\pi^0$ lead to two significant peaks in the pp missing mass spectrum.

3.1 Track selection

There are three main parameters which allow to judge the quality of a reconstructed track. These parameters are:

1. χ^2 of the inner segment track fit
2. χ^2 of the outer segment track fit
3. χ^2 of the Runge-Kutta track fit

No selection is done on the quality parameters of reconstructed tracks due to two reasons:

1. The χ^2 distributions differ considerably between real data and simulations. A selection based on the χ^2 values would introduce losses, the corrections of which are subject to systematic uncertainties.

2. A cut on the χ^2 values does not improve the signal-to-background ratio in the final spectrum significantly.

Figure 3.2 shows the three χ^2 distributions for real data and for simulations. The deviations between the χ^2 distributions are visible in the figure. In real data, events belonging to the reaction $pp \longrightarrow pp\pi^+\pi^-\pi^0$ were selected using the tof-momentum PID algorithm together with the π^0 missing mass cut (see sections 3.3.2 and 3.3.3). In simulations, events of the reactions $pp \longrightarrow pp\omega/\eta$ were produced according to phase space with the subsequent decay of ω/η mesons into $\pi^+\pi^-\pi^0$. The tof-momentum PID and π^0 missing mass algorithms were also applied. For the details of the simulation see chapter 5.

Figure 3.3 shows the pp missing mass spectrum for three event samples:

Sample 1: includes events where tracks undergo no quality selection (all events)

Sample 2: includes events where all three χ^2 values of every track lie within the best 90% of the corresponding χ^2 distribution

Sample 3: includes events where all three χ^2 values of every track lie within the best 80% of the corresponding χ^2 distribution

As can be seen in figure 3.3(b), the selection on the quality parameters of the tracks does not lead to a significant improvement in the signal-to-background ratio in the final spectrum.

Since the selection of reconstructed tracks based on their quality parameters would lead to systematic uncertainties as mentioned before, while not improving the signal-to-background ratio in the final spectra, no such cuts on the track quality are applied during the data analysis.

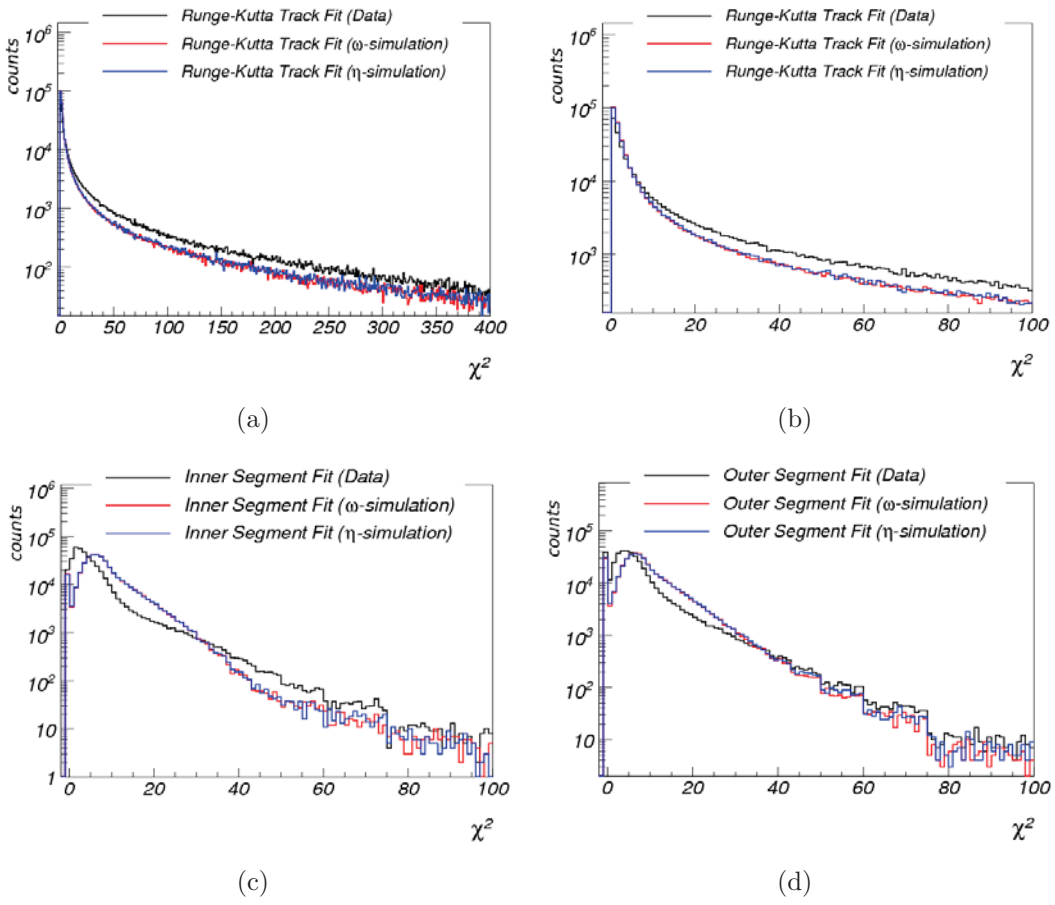

Figure 3.2: χ^2 distributions of segment and track fits. a) Runge-Kutta track fit. b) Runge-Kutta track fit (zoomed). c) Inner segment fit. d) Outer segment fit. The black curves show the corresponding distribution for real data, while the red and blue curves show the distributions for simulations of the reactions $pp \longrightarrow pp\omega \longrightarrow pp\pi^+\pi^-\pi^0$ and $pp \longrightarrow pp\eta \longrightarrow pp\pi^+\pi^-\pi^0$, respectively.

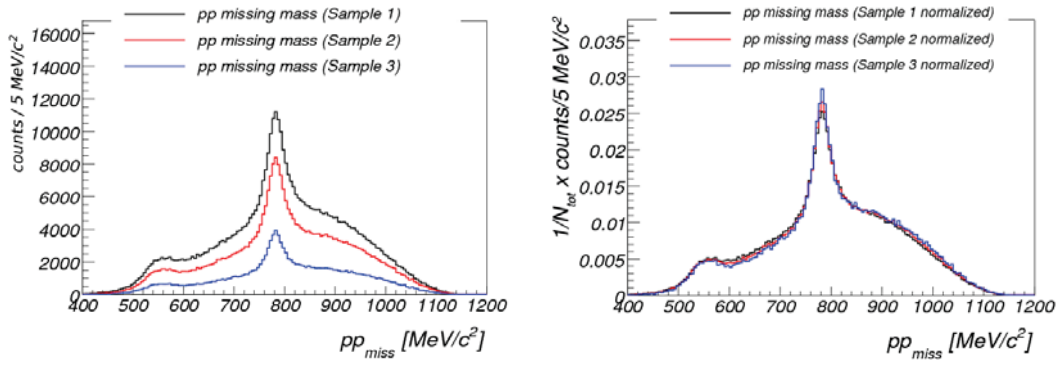

(a) (b)

Figure 3.3: pp missing mass spectrum for three event samples: a) counts / (5 MeV/c^2) and b) all curves normalized to unity. The black line represents the spectrum from sample 1 (all events). The red and blue lines represent the spectra from samples 2 and 3 respectively. The spectra were obtained after applying the tof-momentum PID algorithm and the π^0-missing-mass-cut event selection method (see 3.3.2 and 3.3.3).

3.2 Event ensemble

Every event which contains exactly three positively- and one negatively-charged tracks is included in the event ensemble. For each event, three hypotheses for the identity of the positively charged tracks are considered as shown in table 3.1.

Track	1	2	3	4	missing track
Charge	+	+	+	-	neutral
Hypothesis 1	p	p	π^+	π^-	π^0
Hypothesis 2	p	π^+	p	π^-	π^0
Hypothesis 3	π^+	p	p	π^-	π^0

Table 3.1: Table of the three event hypotheses assumed for each event in the event ensemble.

In the next step(s), different algorithms are applied to find out the correct event hypothesis. PID algorithms allow for the identification of the positive pion, while event selection algorithms (π^0-missing-mass-cut and kinematic fit p-value cut) use kinematics to select the events which include two protons, one π^+, one π^-, and one undetected π^0.

3.3 Particle identification and event selection

The verification of mass and event hypotheses are the main tasks of the data analysis. The algorithms include two PID methods (using energy loss or time of flight information) for the mass hypothesis verification and two event selection methods (missing mass cut or kinematic fit) for the event hypothesis verification. The application of event selection methods is essential for the selection of the final states "$pp\pi^+\pi^-\pi^0$", while the usage of PID methods is optional since most of the wrong mass hypotheses are rejected by the event selection methods (due to kinematics). In the following subsections the PID and event selection methods are discussed in detail.

3.3.1 PID via characteristic energy loss

Charged particles passing through matter lose energy mainly by electromagnetic interaction with the medium. For particles other than electrons, the mean rate of energy loss is given by the Bethe-Bloch equation[N$^+$10]. An approximated form of the Bethe-Bloch equation (neglecting the density effect) is given by equation 3.1,

$$-\left\langle \frac{dE}{dx} \right\rangle = Kz^2 \frac{Z}{A} \frac{1}{\beta^2} \left[\frac{1}{2} ln \frac{2m_e c^2 \beta^2 \gamma^2 T_{max}}{I^2} - \beta^2 \right] \tag{3.1}$$

where

$$T_{max} = \frac{2m_e c^2 \beta^2 \gamma^2}{1 + 2\gamma m_e/M + (m_e/M)^2}$$

is the maximum energy which can be transfered to a free electron in a single collision, and

ze	is the charge of the incident particle,
Z	is the atomic number of the absorber (medium),
A	is the atomic mass of the absorber,
β	is the velocity of the incident particle (v/c),
γ	is the relativistic gamma of the incident particle,
I	is the mean excitation energy of the absorber,
M	is the incident particle mass,
$m_e c^2$	is the electron mass $\times$ c^2,
$K = 4\pi N_A r_e^2 m_e c^2$	is a constant (see [N$^+$10]).

Charged particles –apart from electrons– traversing the MDCs lose energy along their trajectories at a mean rate given by equation 3.1. This information is used

–together with the momentum information– to identify such particles. Figure 3.4 shows the track energy loss in the MDCs versus the reconstructed momentum for: a) negatively charged tracks and b) positively charged tracks. Tracks with negative polarity are dominated by negative pions while those with positive polarity are dominated by protons and positive pions. The solid curves in figure 3.4 show the mean rate of energy loss for pions and protons calculated using equation 3.1.

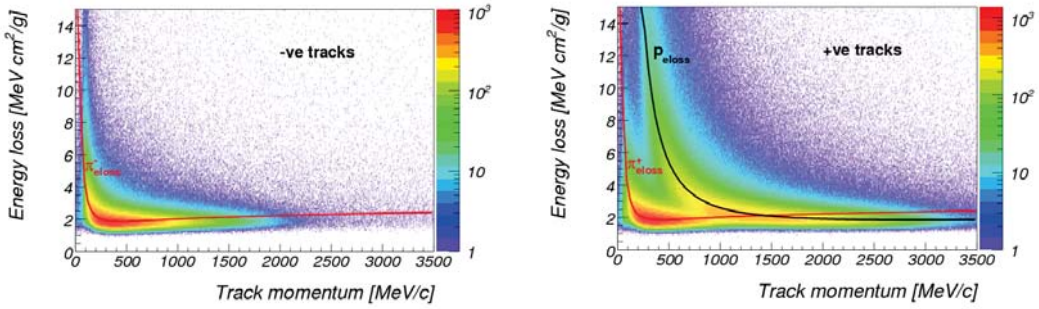

(a) (b)

Figure 3.4: Energy loss versus momentum of: a) negatively charged tracks and b) positively charged tracks. The solid curves are calculated using the Bethe-Bloch formula. Negative tracks are dominated by π^-. Positive tracks are dominated by protons and π^+.

The deposited energy along a charged particle trajectory follows a Landau distribution [Sau]. Figure 3.5 shows the distribution of deposited energy by negatively charged tracks at four different momenta. The solid lines in figure 3.5 represent the result of fitting the spectra using a Landau function. The results of such Landau fits over the momentum range of 80-2000 MeV/c are summarized in figure 3.6. The magenta curves in figure 3.6(b) represent a parametrization of $\sigma(p)$ by two polynomial functions.

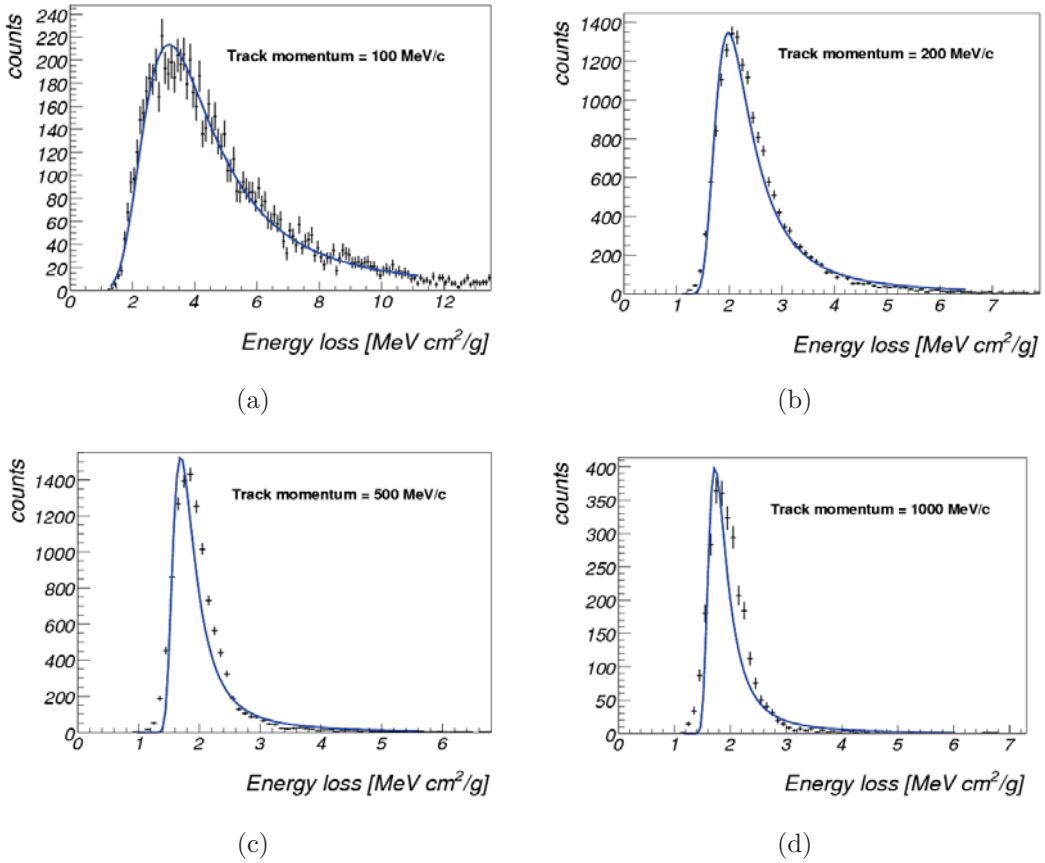

Figure 3.5: Distribution of deposited energy by negatively charged tracks. The blue lines represent a Landau fit to the distributions. Tracks are selected within a momentum window of 1 MeV/c.

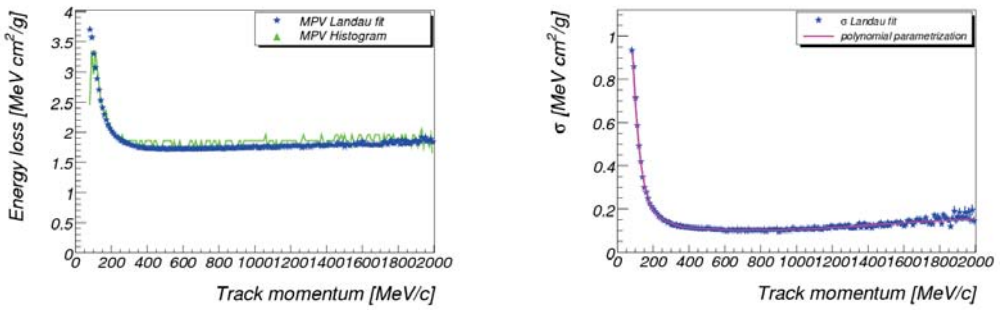

(a) (b)

Figure 3.6: Results of the Landau fit to the energy loss distribution of negatively charged tracks as a function of momentum (blue points). a) The most probable value (MPV)- and b) σ of the fit. The green curve in (a) shows the value of energy loss at which the fitted histogram is at maximum. The magenta curve in (b) is a polynomial parameterization of $\sigma(p)$.

Since negatively charged tracks are dominated by negative pions, the results of figure 3.6 summarize the momentum dependence and the properties of the distribution of energy deposited by negative pions in the MDCs. Moreover, positive pions should exhibit the same energy loss behavior as negative ones. Hence, the results of figure 3.6 hold as well for describing the energy loss of positive pions in the MDCs. The results of figure 3.6 are used to define the region inside the dE/dx versus momentum plot in which most of the pions are expected to be. At each momentum value between 80 and 2000 MeV/c, the selection region covers from $MPV - 3\sigma$ to $MPV + 12\sigma$. In a Landau distribution, such range corresponds to 90% of the area under the curve.
The pion selection region is shown in figure 3.7. Rather than declaring each particle inside the selection region to be a π^+ (which is not true since above 600 MeV/c, protons have a similar rate of energy loss as pions), particles outside the selection region are excluded from being a π^+. Tracks inside the selection region maybe a π^+ or a proton.

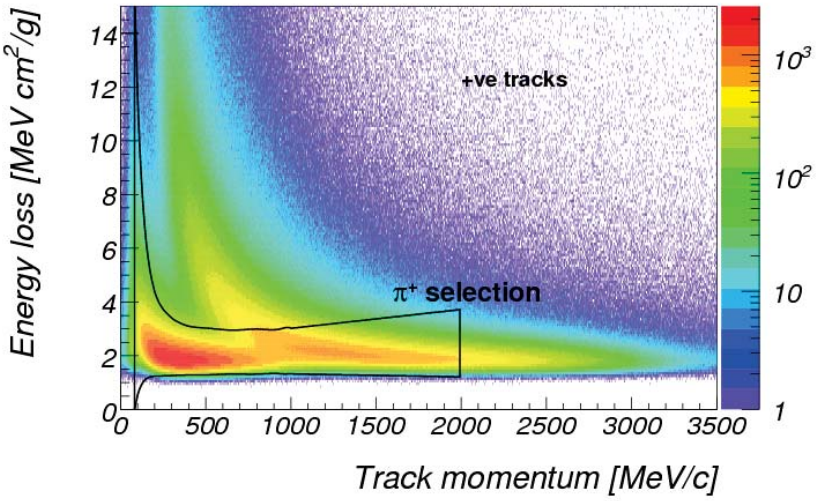

Figure 3.7: Selection region of positive pions. Particles outside the selection region are excluded from being a π^+, while those inside maybe a π^+ or a proton.

At low momenta (< 600 MeV/c) protons have a much higher energy loss than pions. Therefore, one can define a lower boundary in the dE/dx versus momentum plot below which particles are excluded from being a proton. To define such a lower boundary, again the momentum dependence of the MPV and σ of the proton

energy loss distribution must be known. To obtain this information, the energy loss distribution of positively charged tracks is fitted at different momentum values between 200 and 1500 MeV/c using two Landau functions. The parameters of the first Landau function are initialized to the values obtained for negative pions. For the second Landau function, only the MPV is initialized to the value expected by the Bethe-Bloch formula for protons with the other parameters left uninitialized.
Figure 3.8 shows such energy loss distributions of positively charged tracks at two different momenta and the result of the double Landau fit (blue line).

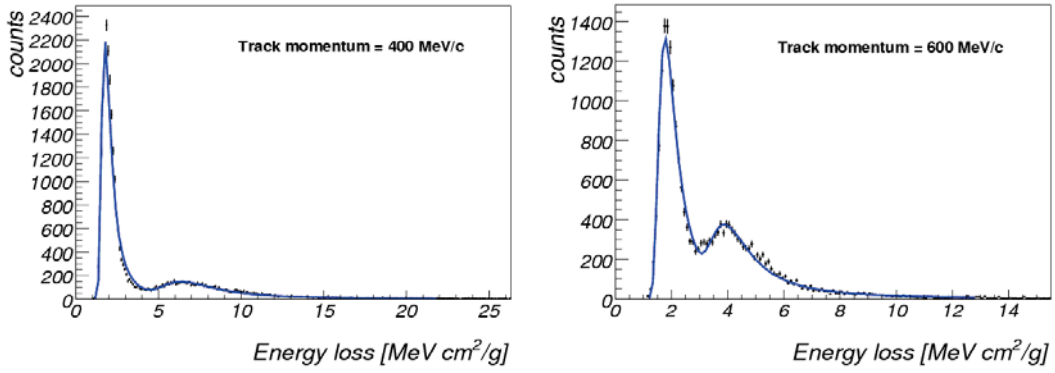

(a) (b)

Figure 3.8: Distribution of deposited energy by positively charged tracks. The blue lines represent a double Landau fit to the distributions. Tracks are selected within a momentum window of 1 MeV/c.

Above 1500 MeV/c, protons dominate the spectrum. Hence, the energy loss distributions above 1500 MeV/c are fitted using only one Landau function.
The results of the Landau fits for protons in the range of 200-3500 MeV/c are summarized in figure 3.9. As in the case of negative pions, both MPV(p) and σ(p) are parameterized using two polynomial functions (magenta curves).

Using this information, the lower boundary for the selection of protons is defined at $MPV - 3\sigma$, while the upper boundary is defined at $MPV + 210\sigma$. Such range includes 99.5% of the area below a Landau distribution.
Figure 3.10 shows the lower boundary for the selection of protons together with the π^+ selection region. Tracks depositing energy below the proton boundary are excluded from being a proton.

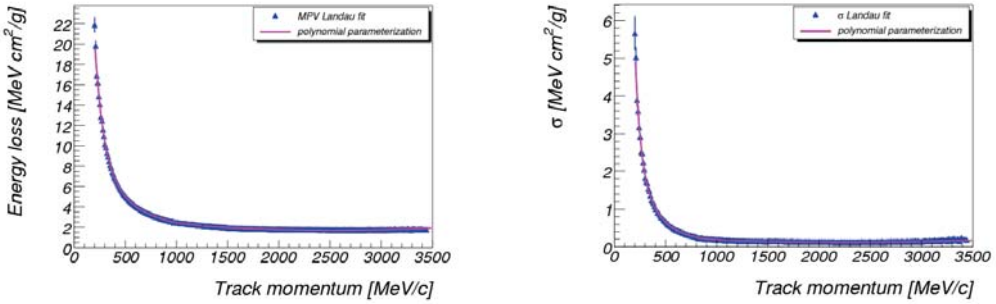

(a) (b)

Figure 3.9: Results of the Landau fit for protons as a function of momentum. a) The most probable value (MPV) and b) σ of the fit. The magenta curves show a polynomial parameterization of MPV(p) andσ(p).

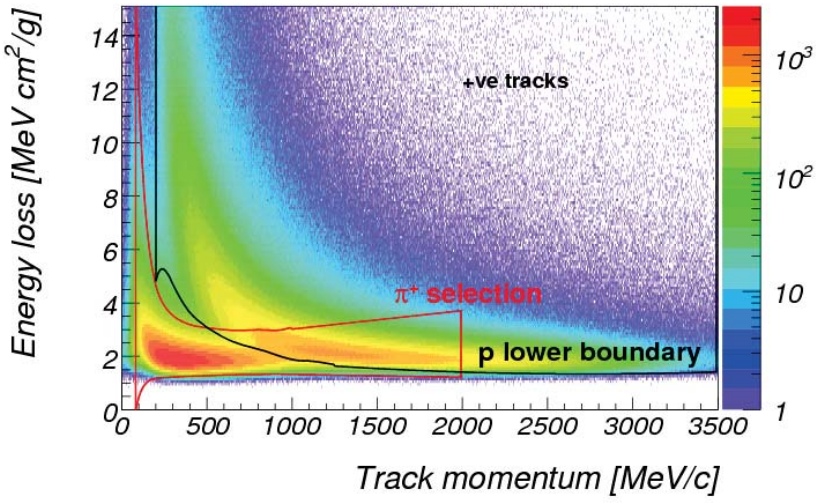

Figure 3.10: Lower boundary for the selection of protons. Tracks below the proton selection boundary are excluded from being a proton.

As mentioned in section 3.2, every event containing three positively charged tracks and one negatively charged tracks is included in the event ensemble. Moreover, for each event in the ensemble, three hypotheses for the ID of the positively charged particles are considered. Applying the dE/dx PID method rejects a huge number of events (not containing one π^+ and two protons). Additionally, for most of the remaining events, only one hypothesis is left over. Only for a small fraction of events, two or three hypotheses are not rejected by the dE/dx selection. Table 3.2 summarizes the result of applying the dE/dx selection on the number of events and the number of hypotheses per event.

	Event ensemble	dE/dx selection	Ratio
1 hypothesis	23072372	11453668	49.6%
2 hypotheses		990775	4.3%
3 hypotheses		469993	2.0%
		Total	55.9%

Table 3.2: Number of events with one, two, and three non rejected hypotheses after the application of the dE/dx selection.

3.3.2 PID via mass reconstruction using time of flight

The momentum **p** of a relativistic particle is related to its rest mass **m** and speed β by the relation:

$$p = \frac{m\beta}{\sqrt{1-\beta^2}}$$

or alternatively :

$$m^2 = \frac{(1-\beta^2)p^2}{\beta^2} \tag{3.2}$$

The track fitting algorithms reconstruct the momentum and trajectory of a charged particle traversing the MDC's. When such particles hit the META detector, their hit time is measured. This time is called the time of flight (tof). It is the difference between the time of the META hit and the trigger/reaction time *i.e.* it is the time needed by the particle to travel from the target to the META wall. Knowing the time of flight of a particle and the length of its trajectory from the target to the META wall, one can calculate its speed β. Together with the reconstructed momentum, equation 3.3.2 is used to determine the mass of the particle. Figure

3.11 shows the distribution of the calculated masses (squared) for particles in the event ensemble which hit the META detector. The distribution is peaked at two

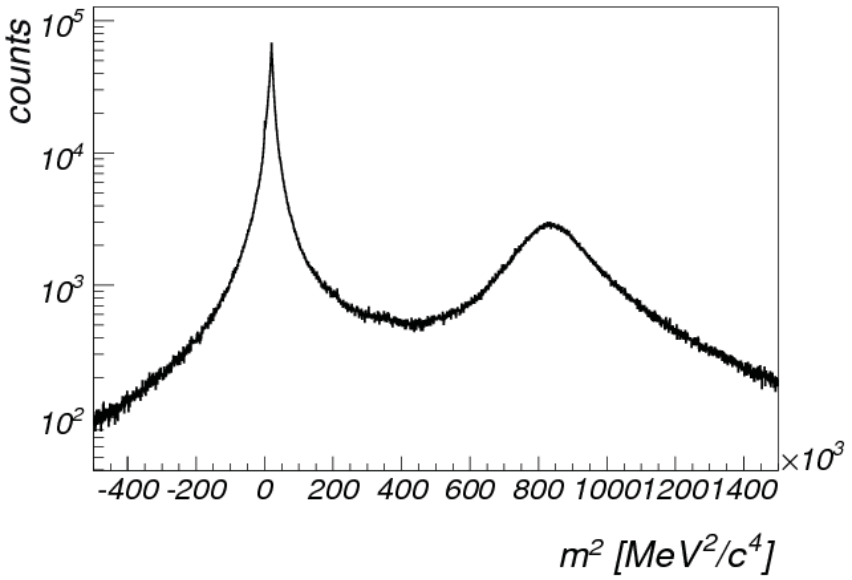

Figure 3.11: The distribution of mass determined using equation 3.3.2 for particles in the event ensemble hitting the META detector. The distribution is peaked at the position of the pion and of the proton mass.

points corresponding to the square of the pion mass (about 20 000 MeV^2/c^4) and the square of the proton mass (about 880 000 MeV^2/c^4). Based on this distribution, two cuts are applied to select pions and protons.
Particles whose determined mass lies between $-280\,000\ MeV^2/c^4$ and $320\,000\ MeV^2/c^4$ are identified as pions. Those whose reconstructed mass lies between $400\,000\ MeV^2/c^4$ and $1\,600\,000\ MeV^2/c^4$ are identified as protons. Since there is no overlap between the two selection windows, the number of hypotheses per event after applying the tof-momentum PID algorithm is always one.

To check the purity of the method, figure 3.12 shows the dE/dx versus momentum plot for positive pions and for protons identified using the tof-momentum PID algorithm. The plots show a very low level of misidentification.

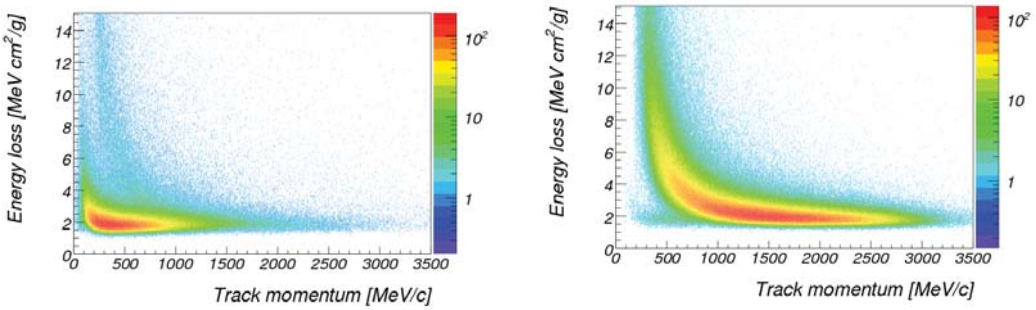

(a) (b)

Figure 3.12: The dE/dx vs momentum distribution for particles identified via the tof-momentum PID algorithm as a: a) positive pion. and b) proton. Both figures show a very low level of misidentified particles.

3.3.3 Event selection via π^0 missing mass cut

The missing mass technique is used to select events in which –besides the detected particles– one additional particle of a known mass is produced. One calculates the 4-vector difference between the sum of the incoming particles (beam + target) and the sum of the detected outgoing particles. The invariant mass of such difference vector is called the missing mass.
Figure 3.13 shows the missing mass (squared) distribution for events, in which two protons, one positive pion, and one negative pion were identified using the dE/dx PID method. The distribution exhibits two peaks: one peak at zero corresponding to the reaction $pp \longrightarrow pp\pi^+\pi^-$ and another peak at about $18.2\times10^3\ MeV^2/c^4$ (square of the π^0 mass) corresponding to the reaction $pp \longrightarrow pp\pi^+\pi^-\pi^0$.

Events/hypotheses in which the missing mass lies outside the range of 480-36300 MeV^2/c^4 are rejected by the missing mass cut. The basis of selection of this window is explained in section 8.2.1.

As mentioned in section 3.2, for each event in the event ensemble, three mass hypotheses for the mass of the positively charged particles are considered. PID methods are used to verify the correct mass hypotheses and reject the wrong ones. However, applying the π^0 missing mass cut implies kinematical constraints on the particles in an event which lead to the rejection of most of the wrong mass hypotheses without the need for using PID algorithms. Table 3.3 summarizes the result of

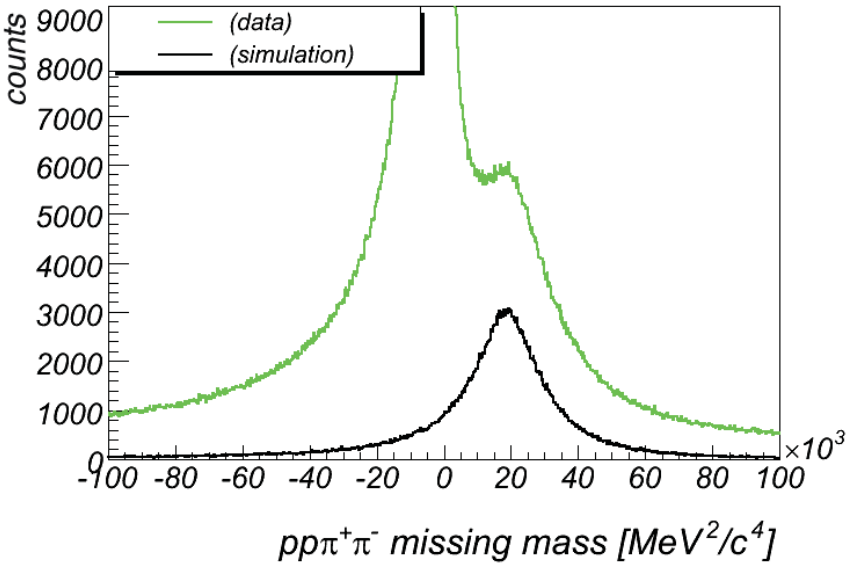

Figure 3.13: The $pp\pi^+\pi^-$ missing mass distribution in: real data (green) and in simulations of the reaction $pp \longrightarrow pp\pi^+\pi^-\pi^0$ (black). The distribution in real data exhibits two peaks: one peak at zero corresponding to the reaction $pp \longrightarrow pp\pi^+\pi^-$ and another peak at about 18.2×10^3 MeV^2/c^4 (square of the π^0 mass) corresponding to the reaction $pp \longrightarrow pp\pi^+\pi^-\pi^0$. The two protons and the positive pion were identified using the dE/dx PID method.

applying the π^0 missing mass cut on the events of the event ensemble on the number of accepted events and hypotheses per event.

	Event ensemble	π^0 missing mass	Ratio
1 hypothesis	23072372	1080741	4.684%
2 hypotheses		45732	0.198%
3 hypotheses		6936	0.030%
		Total	4.912%

Table 3.3: The result of applying the π^0 missing mass cut on the number of events in the event ensemble and on the number of hypotheses per event. The cut rejects more than 95% of the events in the event ensemble. For about 95% of accepted events, only one hypothesis is not rejected by the cut.

The π^0 missing mass cut leaves 95% of events with only one hypothesis for the identity of the tracks. As a qualitative check for the purity of such method, figure 3.14 shows the dE/dx vs momentum distribution of positive pions and of

protons in events selected using the π^0 missing mass cut. The figure shows that the

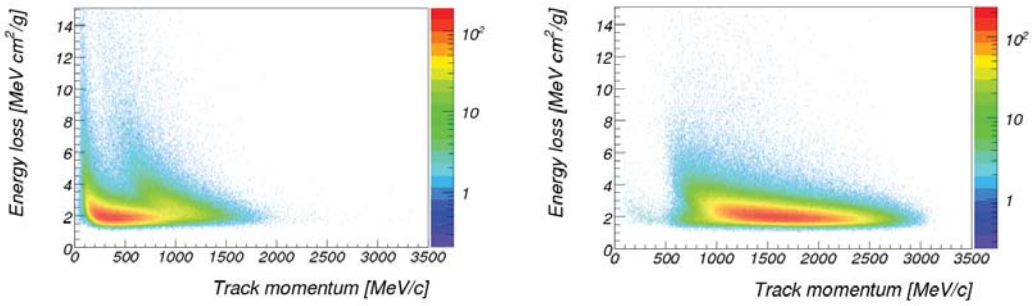

(a) (b)

Figure 3.14: The dE/dx vs momentum distribution for particles identified via the π^0 missing mass cut as a: a) positive pion. and b) proton. The impurity of the identification is visible in plot (a). A small fraction of protons is being identified as a positive pion (note the logarithmic scale in the plot).

identification of pions and protons via the missing mass method is correct in most of the cases. Only for a small fraction of events, protons are misidentified as positive pions and vice versa.

To estimate the amount of events in which particles are misidentified, the dE/dx selection is applied in addition to the π^0 missing mass cut. The results are summarized in table 3.4. The reduction in the number of events in which only one hypothesis is accepted is about 14%. However, this number includes the inefficiency of the dE/dx selection. The coverage of the dE/dx distribution by π^+ and proton dE/dx cuts is 90% and 99.5% respectively (see 3.3.1). Accordingly, the inefficiency of the dE/dx selection in events with two protons and one positive pion can be estimated to be about 11%. Subtracting this number from the previous reduction ratio, the fraction of events accepted by the π^0 missing mass cut in which particles are misidentified can be estimated to be about 3%.

3.3.4 Event selection via kinematic fit p-value cut

The kinematic fit is an established method for improving the finite resolution of experimental measurements. With the help of the knowledge of the measurement error, measured track parameters (such as momentum, θ, and ϕ) are modified such that certain physics constraints are fulfilled. The physics constraints may be *e.g.*

	Event ensemble	dE/dx + π^0 missing mass	Ratio
1 hypothesis	23072372	930178	4.032%
2 hypotheses		22187	0.096%
3 hypotheses		3370	0.015%
		Total	4.142%

Table 3.4: The result of applying the dE/dx- and π^0 missing mass selection on the number of events in the event ensemble and on the number of hypotheses per event. The application of the dE/dx selection in addition to the π^0 missing mass cut reduces the number of events in which only one hypothesis is accepted by about 14%. The number of events with two or three accepted hypotheses is reduced by about a factor of two.

energy and momentum conservation or the known mass of a missing particle. More details about the kinematic fit are discussed in chapter 4.

For each (re)fitted event, the fit returns a χ^2 value which can be translated into a p-value. The p-value is equivalent to the probability of the event to belong to the assumed reaction hypothesis. The p-value distribution for all events in the event ensemble is shown in figure 3.15.

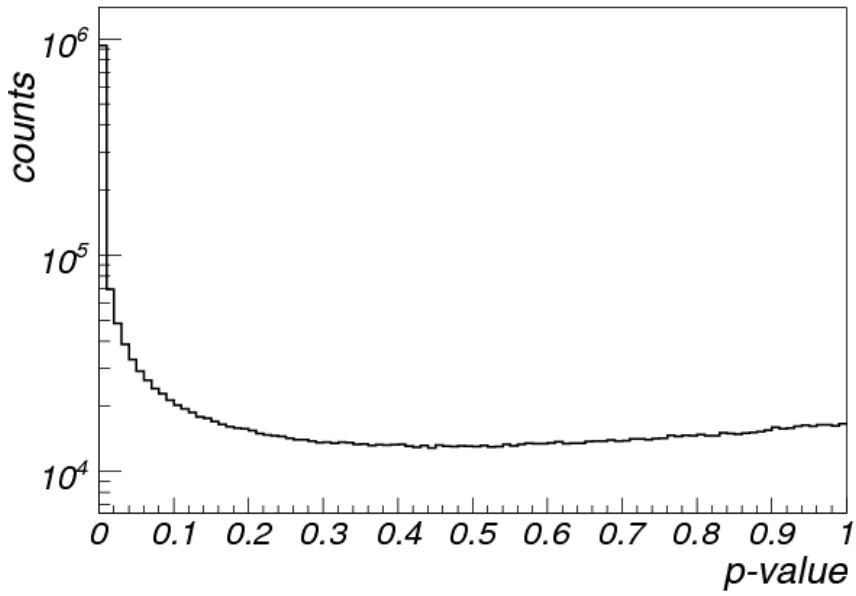

Figure 3.15: The kinematic fit p-value distribution for all event in the event sample. The distribution is peaked near to zero and is fairly flat beyond about 0.16.

As will be discussed in chapter 4, the p-value of events belonging to the fitted reaction hypothesis should be equally distributed in the range from zero to one. Event belonging to other reactions should have a small p-value and thus result in a peak near to zero as shown in figure 3.15. Selecting events with a p-value, for example, higher than 16% allows for the rejection of most of the events not belonging to the assumed reaction hypothesis.
In table 3.5, the number of accepted events/mass hypotheses per event after applying the kinematic fit on events in the event ensemble and a p-value cut at 16% is shown. As in section 3.3.3, figure 3.16 shows the dE/dx versus momentum plot for positively

	Event ensemble	Kine. fit (p-value cut)	Ratio
1 hypothesis	23072372	1062550	4.605%
2 hypotheses		64253	0.278%
3 hypotheses		15422	0.067%
		Total	4.951%

Table 3.5: The result of applying the kinematic fit and a p-value cut at 16% on the number of events in the event ensemble and on the number of hypotheses per event. The numbers are comparable with those in table 3.3. Here, no PID or missing mass cut is applied.

charged particles identified by the kinematic fit (p-value cut at 16%). The plots show a low misidentification level. Table 3.6 summarizes the result of applying the dE/dx selection in addition to the kinematic fit p-value cut at 16%. The number of events in which only one hypothesis survives the p-value cut is reduced by about 13%. Assuming the inefficiency of the dE/dx selection to be about 11%, the fraction of events in which particles are misidentified is about 2%.

Besides improving the resolution, the kinematic fit (and p-value cut) provides a method to identify protons and pions in events of the reaction: $pp \longrightarrow pp\pi^+\pi^-\pi^0$. Such events could, in turn, be used to train and test the various PID methods.

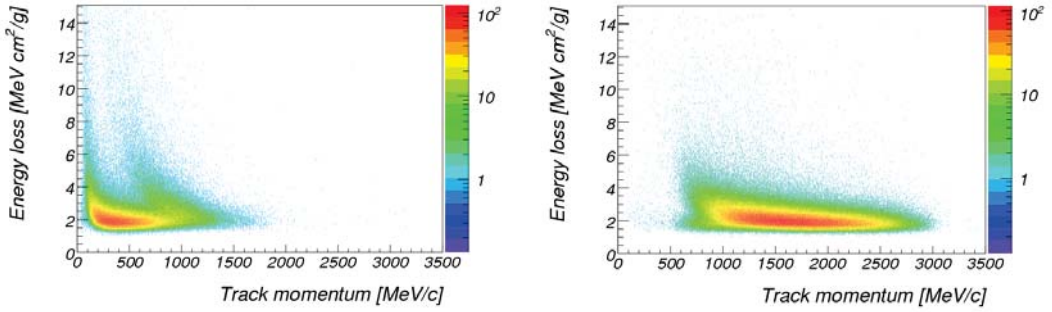

(a) (b)

Figure 3.16: The dE/dx versus momentum distribution for particles identified using the kinematic fit p-value cut as a: a) positive pion. and b) proton. A small fraction of the particles is misidentified (note the logarithmic scale in the plots).

	Event ensemble	dE/dx + kine. fit (p-value cut)	Ratio
1 hypothesis	23072372	926931	4.017%
2 hypotheses		26800	0.116%
3 hypotheses		6793	0.029%
		Total	4.163%

Table 3.6: The result of applying the dE/dx selection in addition to the kinematic fit with a p-value cut at 16% on the number of events in the event ensemble and on the number of hypotheses per event. The dE/dx selection reduces the number of events with only one accepted hypothesis by about 13%. The number of events with two or three accepted hypotheses is reduced by more than a factor of two.

3.4 The proton-proton missing mass spectrum

After the verification of the reaction and mass hypotheses using the methods described in section 3.3, events belonging to the reaction channel $pp \longrightarrow pp\pi^+\pi^-\pi^0$ can be selected. Those events include events of the reactions $pp \longrightarrow pp\eta$ and $pp \longrightarrow pp\omega$ with the subsequent decay of η and ω mesons into $\pi^+\pi^-\pi^0$. The branching ratios for the decay of η and ω mesons into $\pi^+\pi^-\pi^0$ are 22.74% and 89.2% [N$^+$10], respectively. Plotting the proton-proton missing mass distribution for all events belonging to the reaction $pp \longrightarrow pp\pi^+\pi^-\pi^0$, one observes a continuous distribution starting at the sum of the masses of the three pions (about 413 MeV/c^2) up to the kinematic limit given by the beam energy and acceptance of the spectrometer (about

1160 MeV/c^2). On top of such smooth distribution, two peaks corresponding to the reactions $pp \longrightarrow pp\eta$ and $pp \longrightarrow pp\omega$ can be observed at the position of the η and ω meson masses (547.853 MeV/c^2 and 782.65 MeV/c^2 [N$^+$10] respectively).
Figure 3.17(a) shows the pp missing mass distribution for events selected using the π^0 missing mass cut. The black curve is for events selected using the cut without any further mass verification method. The red curve shows the spectrum when applying the dE/dx selection for mass verification in addition to the π^0 cut. The blue curve shows the spectrum when applying the tof-momentum selection in addition to the π^0 cut. The application of the tof-momentum PID method reduces the counts

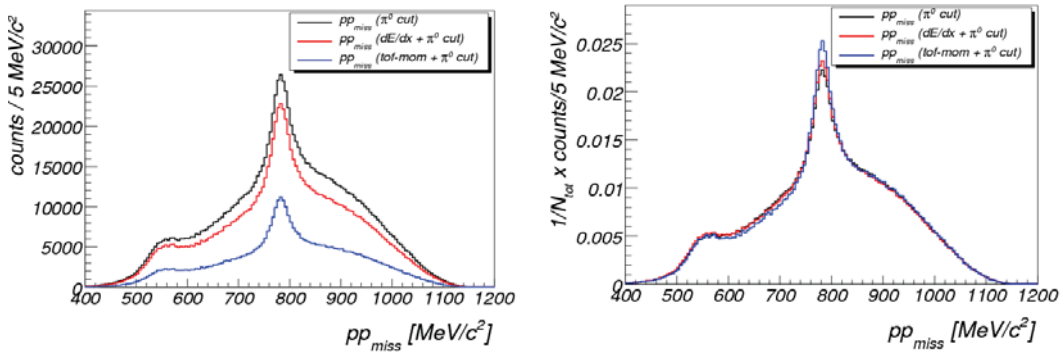

(a) (b)

Figure 3.17: pp missing mass spectrum for events selected using the π^0 missing mass cut. a: counts per 5 MeV/c^2. b: all curves are normalized to unity. The black curve is for all selected events. The red curve is for events which additionally passed the dE/dx selection. The blue curve is for events which passed the tof-momentum selection in addition to the π^0 cut.

in the spectrum by more than a factor of two (compare black and blue curves in figure 3.17(a)). This reflects the inefficiency of the META detector including the matching between a META hits and MDC tracks. The dE/dx selection results in a much lower count loss.
In figure 3.17(b), the three curves of figure 3.17(a) are normalized to unity. The shape of the three curves is essentially the same. The tof-momentum identification leads to a slightly higher signal-to-background ratio which, however, does not justify the high yield loss.

Figure 3.18 shows similar plots to those of figure 3.17 for events selected using the kinematic fit + p-value cut at 16%. Concerning the background shape and the

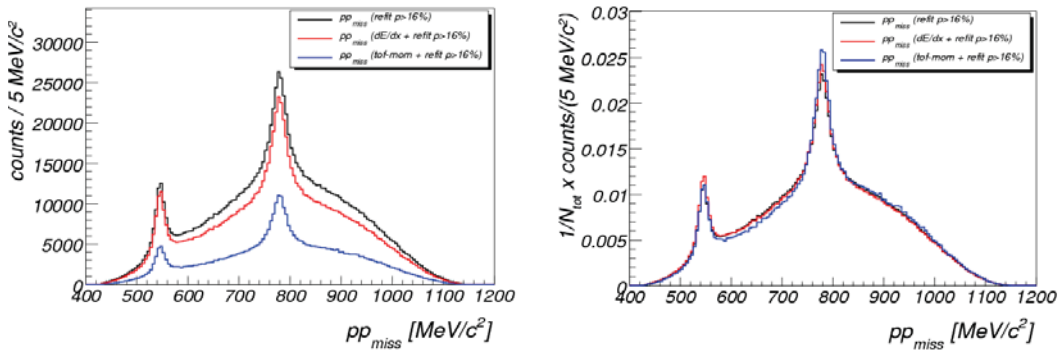

(a) (b)

Figure 3.18: pp missing mass spectrum for events selected using the kinematic fit p-value cut. a: counts per 5 MeV/c^2. b: all curves are normalized to unity. The black curve is for all selected events. The red curve is for events which additionally passed the dE/dx selection. The blue curve is for events which passed the tof-momentum selection in addition to the p-value cut.

count losses due to the two PID methods, the results are similar to those using the π^0 missing mass cut. However, concerning the η meson peak at 447 MeV/c^2, the signal to background ratio is considerably enhanced using the kinematic fit. A direct comparison between the pp missing mass spectrum of events selected via the π^0 missing mass cut and that of events selected using the kinematic fit and p-value cut is not shown here. This will be discussed is chapter 4.

Integrating the number of counts inside the two peaks in the pp missing mass spectrum yields the number of reconstructed η and ω mesons. After acceptance correction (chapter 5) and the absolute normalization (chapter 7), this number can be translated into the production cross section of the ω and η mesons.

4

Kinematic fit

The kinematic fit is a well established method for improving the resolution of experimental measurements [BST61][Rus06][Sie10]. In this chapter, the basic concepts and formulas in kinematic fitting are introduced (section 4.1). In section 4.2, the results of applying the kinematic fit on experimental data and simulation are presented.

4.1 Introduction

The kinematic fit uses physics constraints to modify the measured track[1] parameters such that the physics constraints are fulfilled. The knowledge of the measurement error is essential in order to know how far measured quantities can be modified. The result of the kinematic fit is a modified set of track parameters. Quantities (*e.g.* missing or invariant mass of two particles) reconstructed using the modified parameters usually have a better resolution than using original parameters.
In the HADES experiment, the track parameters (1/p,θ,ϕ) are chosen when applying the kinematic fit where p is the momentum of the particle, θ and ϕ are its polar and azimuthal angles, respectively.

Consider a reaction with n detected particles in the final state. Let x^m be a $3n$-component vector of the measured track parameters of the n particles, x a $3n$-component vector of modified track parameters, and M an n-component vector of the masses of the n particles.

[1] A track means a particle trajectory as far as geometrical quantities are described, *e.g.* curvature. If physical quantities are involved, *e.g.* momentum, a track is equivalent to a particle.

Physics constraints, such as *e.g.* the mass of an undetected particle or the conservation of energy and momentum can be represented by an equation $H(x, M) = 0$, where $H(x, M)$ is a vector of length r equal to the number of constraints.
Let δx^m be a $3n$-component vector of errors of the measured track parameters, one may write: $\chi^2 \equiv \Phi(x) = (x - x^m)^T G^{-1}(x - x^m)$ where G^{-1} is the error matrix:

$$G^{-1} = \left\langle \delta x^m \cdot \delta x^{mT} \right\rangle = \begin{pmatrix} \sigma_{11}^2 & k_{12} & k_{13} & \dots & k_{1n} \\ k_{21} & \sigma_{22}^2 & k_{23} & \dots & k_{2n} \\ k_{31} & k_{32} & \sigma_{33}^2 & \dots & k_{3n} \\ . & . & . & \dots & . \\ . & . & . & \dots & . \\ . & . & . & \dots & . \\ k_{n1} & k_{n2} & k_{n3} & \dots & \sigma_{nn}^2 \end{pmatrix}$$

with σ_{ii}^2 being the dispersion of the x_i^m variable, and k_{ij} the correlation between the errors of the x_i^m and x_j^m variables.

The minimum of Φ is obviously zero at $x = x^m$. However, due to the measurement error, the physics constraints are -in general- not fulfilled by the measured parameters, so that $H(x^m, M)$ is usually different from zero. Nevertheless, one may use the method of Lagrange multipliers to find the minimum of Φ fulfilling the constraints. We construct $\Lambda(x, \lambda) = \Phi(x) + 2\lambda \cdot H(x, M)$ and try to solve equation 4.1.

$$\nabla_{x,\lambda} \Lambda(x, \lambda) = 0 \tag{4.1}$$

Solving equation 4.1 returns (x, λ) at which $\Lambda(x, \lambda)$ is at its minimum. Note that $\nabla_\lambda \Lambda(x, \lambda) = 0$ implies that $H(x, M) = 0$. Consequently, solving equation 4.1 returns the minimum of $\Phi(x)$ at which the physics constraints are fulfilled. The value of $\Phi(x)$ is the χ^2 value of the fit.
The χ^2 value is a measure of the *goodness-of-fit*. If the errors of the measured track parameters are gaussiansian and if the event hypothesis is true, then the χ^2 distribution follows the known χ^2 probability density function (f_r) with the number of degrees of freedom equal to the number of constraints (r).
In such case, the $p-$value, given by the probability to find a χ^2 value higher than the measured one ($p = \int_{\chi^2}^{\infty} f_r(z)dz$), will be uniformly distributed between zero and one [N$^+$10]. The $p-$value reflects the degree of compatibility of the data with the assumed hypothesis. Reactions not fulfilling the hypothesis, either by wrong masses or wrong missing particle, lead to a high χ^2 value, and accordingly, a low $p-$value. Measured data (also referred to as real data) always contain more than one type of exclusive reactions. Therefore, when plotting the distribution of the $p-$value for

real data, the spectrum is peaked near to zero. This peak corresponds mainly to events not belonging to the assumed hypothesis.

4.1.1 The error matrix

As discussed before, the knowledge of the error matrix G^{-1} is essential for using the kinemtical fit method. The error matrix is in general a $3n \times 3n$ matrix with the variances of measured quantities on the diagonal and the correlation between them in the off-diagonal elements. Simulations including the various detector and reconstruction effects are used to determine the elements of the error matrix. Here, two assumptions are made. The first assumption is that no correlation between the errors of the track parameters of any two different tracks exists. This means that the error matrix is composed of n 3×3 matrices on the diagonal. The second assumption is that the errors of the parameters of a given track are independent. This means that the remaining off-diagonal elements in the error matrix vanish.
The first assumption is true, especially for the kind of reactions under study in which the particle density is very low. However, simulations show that the second assumption is only valid for the azimuthal angle error ($\delta\phi$). The errors of the momentum and polar angle measurements are strongly correlated.

Figure 4.1 shows the correlation between the errors of the three track parameters for protons in the range ($1750\ MeV/c < p < 1800\ MeV/c$; $40^\circ < \theta < 50^\circ$; $30^\circ < \phi < 40^\circ$). The plots show a strong correlation between $\delta\theta$ and δp. No significant correlation is visible between $\delta\theta$ and $\delta\phi$, and between $\delta\phi$ and δp. The correlation between the errors of the polar angle and momentum measurements is due to the configuration of the HADES magnetic field. The toroidal field is configured such that particles get a *kick, i.e* a strong deflection, in the direction of the polar angle. The momentum of the particle is determined mainly by the change in its polar angle when crossing the magnetic field. Therefore, any error in the determination of the polar angle of the inner track segment (*i.e.* the polar emission angle of the particle) leads to an error in the determination of the amount of angle change and accordingly to an error in the determined momentum.

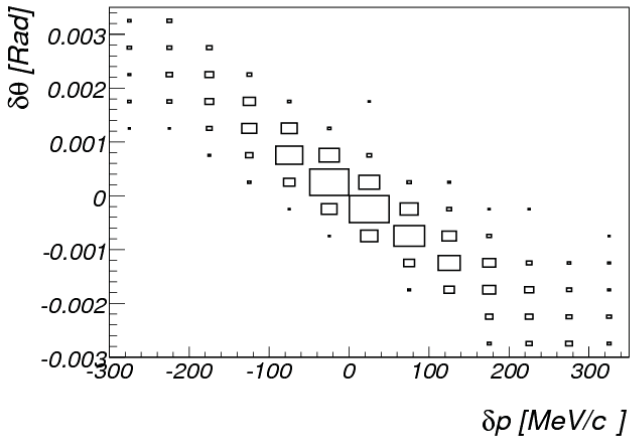

(a)

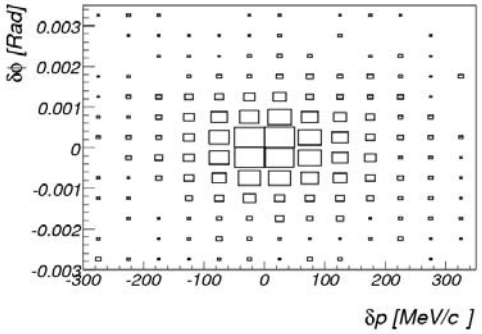

(b)

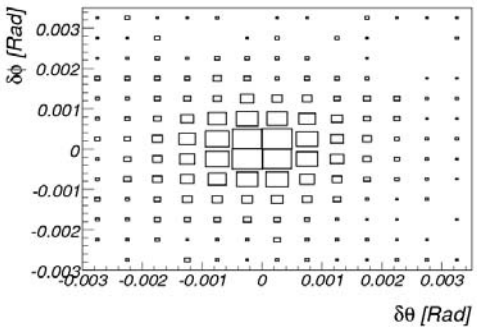

(c)

Figure 4.1: The correlation between the errors of the three measured track parameters. Simulated are protons in the momentum range of $1750 - 1800\ MeV/c$, polar angle range of $40° - 50°$, and azimuthal angle range of $30° - 40°$. a) The difference between simulated and reconstructed particle's polar angle ($\delta\theta$) versus the difference between simulated and reconstructed particle's momentum (δp). The plot shows a strong correlation between $\delta\theta$ and δp. b) The difference between simulated and reconstructed particle's azimuthal angle ($\delta\phi$) versus the difference between simulated and reconstructed particle's momentum (δp). c) The difference between simulated and reconstructed particle's azimuthal angle ($\delta\phi$) versus the difference between simulated and reconstructed particle's momentum ($\delta\theta$). Plots b) and c) show no significant correlation between $\delta\phi$ and δp and between $\delta\phi$ and $\delta\theta$ respectively.

4.2 Results

In the following subsections, the results of applying the kinematic fit on real and simulated data are presented. The fit is applied with one constraint on the mass of the undetected particle (missing mass = π^0 mass). Real data consist of all events of the event ensemble (recall chapter 3) which were not rejected by the dE/dx PID method. The simulated events are only of the reaction $pp \longrightarrow pp\omega \longrightarrow pp\pi^+\pi^-\pi^0$. For details of the simulation see chapter 5. In 4.2.1 and 4.2.2, the distributions of the pull quantities and of the p-value are discussed. In subsection 4.2.3, the $pp-$ and $pp\pi^+\pi^-$−missing mass spectra are compared before and after applying the kinematic fit.

4.2.1 Pull distributions

Pull quantities are used to control the results of applying a kinematic fit [Rus06]. The pull of the $i-$th fitted track parameter is defined as:

$$\text{pull}_i = \frac{x_i^m - x_i^f}{\sqrt{\sigma^2(x_i^m) - \sigma^2(x_i^f)}}$$

where x_i^f is the modified value of $i-$th quantity after the fit, $\sigma^2(x_i^m)$ is the $i-$th diagonal component of the error matrix of measured data, and $\sigma^2(x_i^f)$ is the $i-$th diagonal component of the error matrix after the fit.
If the errors are properly taken into account in the error matrix and if there is no systematic shift of measured parameters, the pull distributions should be centered around zero with a variance equal to one.

Figures 4.2 and 4.3 show the pull distributions for protons in real data and in simulations respectively.

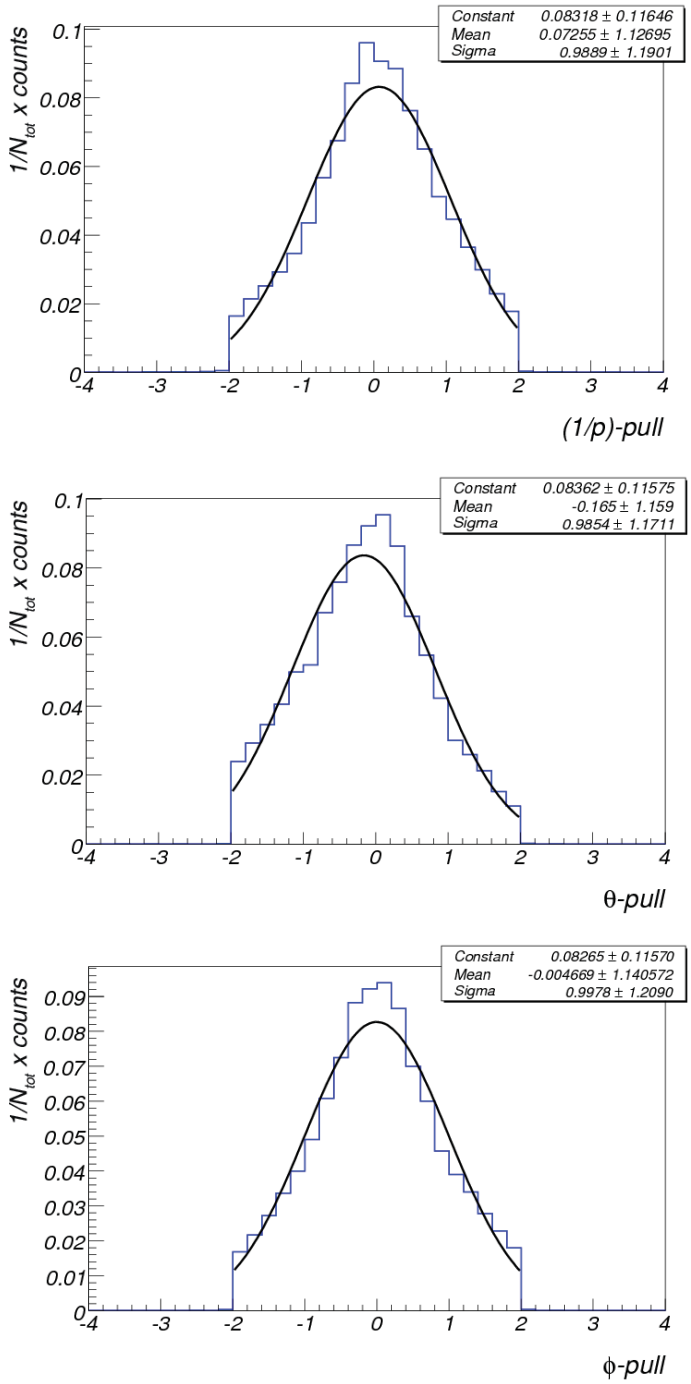

Figure 4.2: The distributions of the pull quantities of protons in real data for kinematic fits with $\chi^2 < 4$. σ of the three distributions is approximately one. The black lines represent Gaussian fits to the distributions.

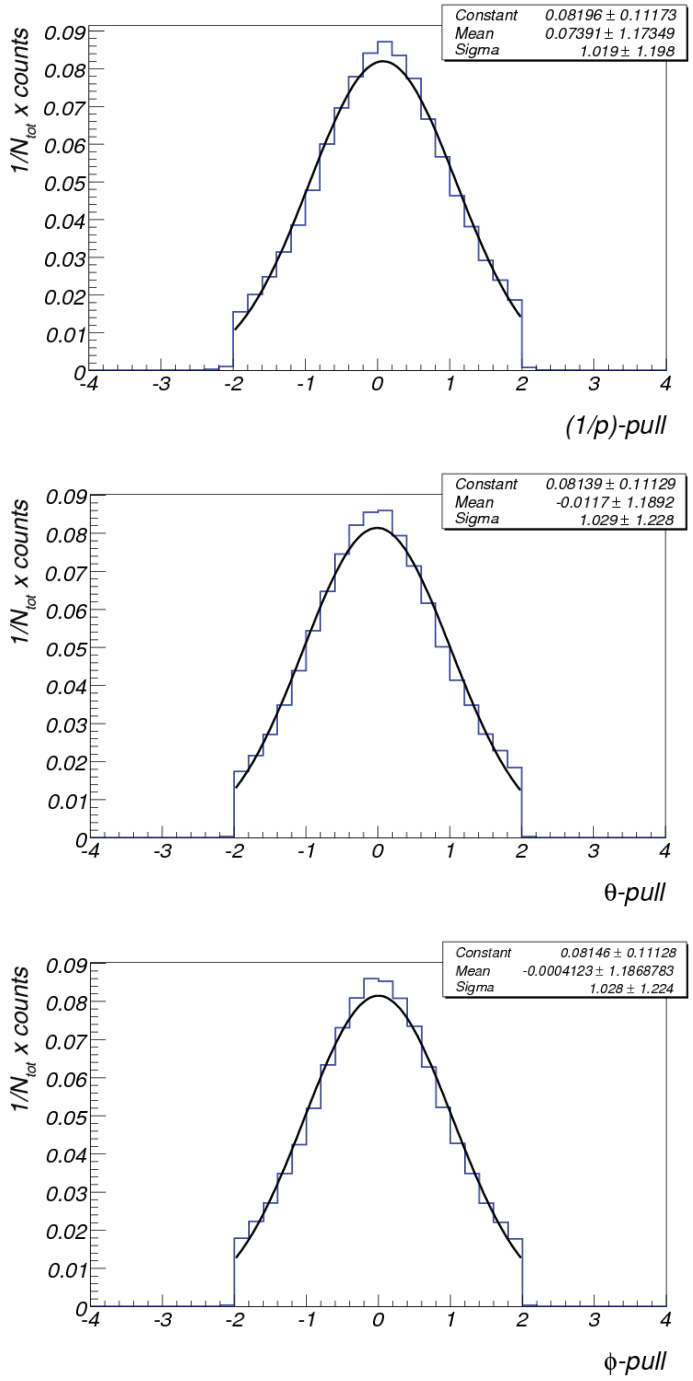

Figure 4.3: The distributions of the pull quantities of protons in simulated data for kinematic fits with $\chi^2 < 4$. σ of the three distributions is approximately one.The black lines represent Gaussian fits to the distributions.

4.2.2 p-value distributions

As mentioned in section 4.1, in the case of Gaussian distributed errors and if the assumed reaction hypothesis is true, the $p-$value will be uniformly distributed between zero and one. However, when applying the kinematic fit on real data, it is usually not possible to obtain a pure sample of events belonging to a specific reaction. Hence, the $p-$value distribution of real data is usually peaked near to zero, mainly due to background processes *i.e.* reactions other than the assumed reaction hypothesis.

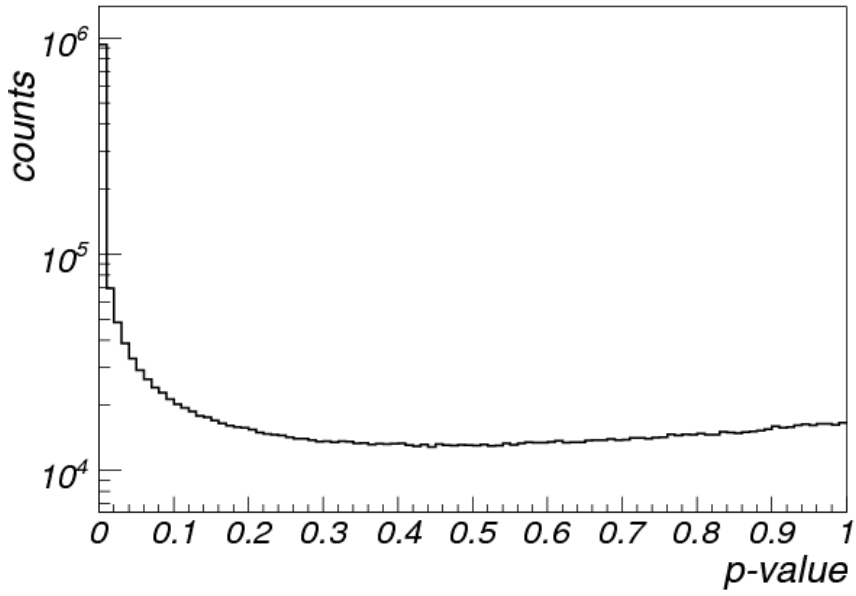

Figure 4.4: The kinematic fit $p-$value distribution for all event in the event ensemble. The distribution is peaked near to zero and is fairly flat beyond about 0.16.

Figure 4.4 shows the $p-$value distribution when applying the kinematic fit to the events of the event ensemble (recall section 3.2). The distribution is peaked near to zero and is approximately flat beyond $p \approx 0.16$. Applying a cut at 16% on the $p-$value allows for rejecting most of the background events. This is illustrated in section 4.2.3.

The peak near to zero in the $p-$value distribution is mainly due to background events. However, also other effects contribute to such peak. Figure 4.5 shows the $p-$value distribution after applying the kinematic fit to simulated events of the reaction: $pp \longrightarrow pp\omega \longrightarrow pp\pi^+\pi^-\pi^0$. The details of the simulation are described in chapter 5. The simulated events are reconstructed using the same reconstruction

chain as for real data. The distribution of the p-value in the simulation is also peaked near to zero and is almost flat starting from $p \approx 0.09$. Four main effects contribute to the low $p-$value peak in the simulation. These are:

1. The correlation between $\delta\theta$ and $\delta(\frac{1}{p})$ not taken into account in the error matrix.

2. Non-Gaussian errors due to the large fluctuations in the processes of energy loss and the corresponding multiple scattering.

3. The decay of charged pions into muons and neutrinos with the decay muons misidentification as the parent pions.

4. Misidentification of protons as pions and vice versa.

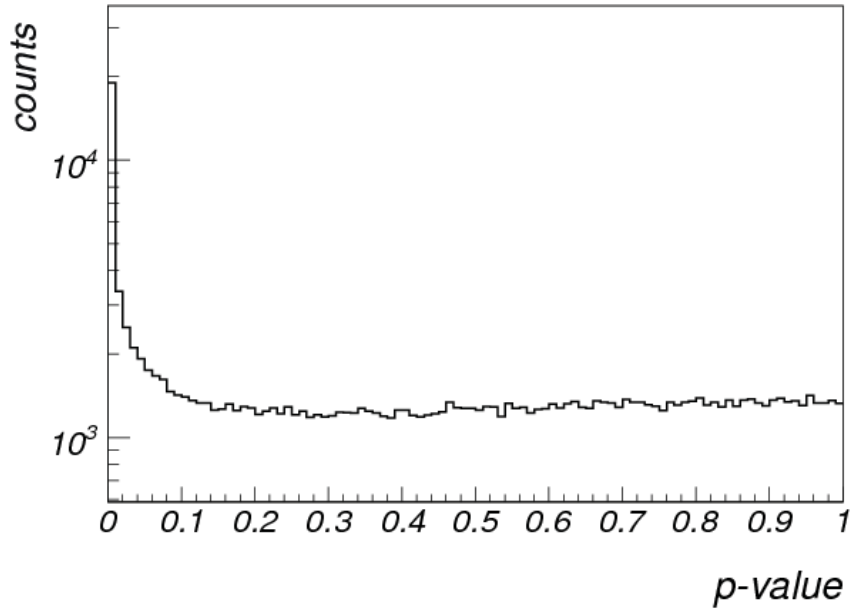

Figure 4.5: The kinematic fit $p-$value distribution for simulated events of the reaction $pp \longrightarrow pp\omega$. The distribution is peaked near to zero and is fairly flat beyond about 0.09.

When applying the acceptance correction (will be discussed in chapter 5), the same $p-$value cut applied in real data is also applied to the simulations. This guarantees the rejection of approximately the same fraction of true events in both cases.

4.2.3 Missing mass spectra

In this section, the result of applying the kinematic fit on real data are presented. Firstly, the results of applying the kinematic fit to events which were selected using the π^0 missing mass cut are presented. The only constraint to the fit is that the missing mass of $pp\pi^+\pi^-$ must be equal to the π^0 mass. In figure 4.6(a), three distributions of the missing mass are shown:

1. Black line: The $pp\pi^+\pi^-$ missing mass distribution of all events. The protons and positive pion were identified using the dE/dx PID method. The distribution shows a peak at zero and another peak at the square of the π^0 mass. The π^0 selection region is indicated by the two vertical lines.

2. Red line: For events selected via the π^0 cut in which the kinematic fit converged: the distribution of the $pp\pi^+\pi^-$ missing mass calculated using the measured (non modified) track parameters of the four particles. As can be seen from the difference between the red and black curves, the kinematic fit partially rejects background events with low missing mass values.

3. Blue line: For events selected via the π^0 cut in which the kinematic fit converged: the distribution of the $pp\pi^+\pi^-$ missing mass calculated using the modified (fitted) track parameters of the four particles. The modified track parameters fulfill the missing mass constraint, and hence, the missing mass distribution is almost a delta function at the position of the π^0 mass.

Without any cut on the $p-$value, the kinematic fit improves the η signal resolution in the pp missing mass spectrum of all $pp \longrightarrow pp\pi^+\pi^-\pi^0$ events without changing the shape of the background. Figure 4.6(b) shows a comparison between the shape of the pp missing mass spectrum obtained using the π^0 missing mass cut and the dE/dx particle identification method with and without the application of the kinematic fit. As can be seen in the figure, the kinematic fit does not change the background shape while it improves the mass resolution of the η meson peak significantly. The η meson peak is almost invisible using the π^0 and dE/dx cuts alone. Only after the application of the kinematic fit, a reliable determination of the counts inside the peak is possible. On the other hand, the kinematic fit does not lead to any significant improvement in the resolution of the ω meson peak. This is due to the different $Q-$ values of the two reactions ($pp \longrightarrow pp\eta$ and $pp \longrightarrow pp\omega$)

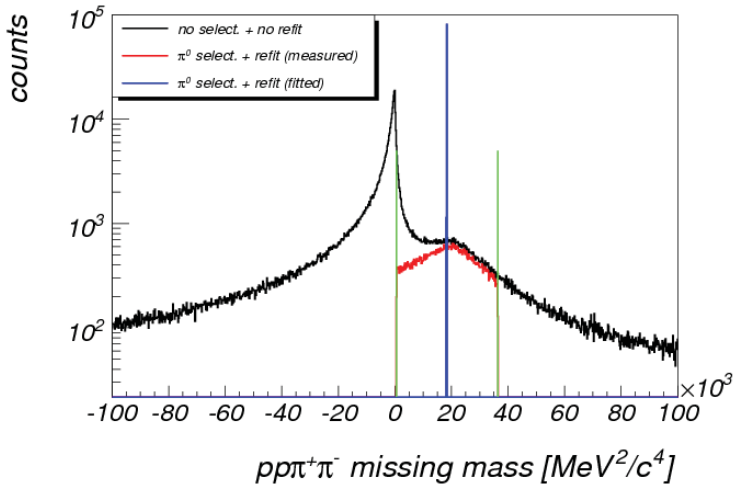

(a) The $pp\pi^+\pi^-$ missing mass distribution: for all events (black). For events selected using π^0 cut and having a converging kinematic fit (mass calculated using measured values (red) and using fitted values (blue)).

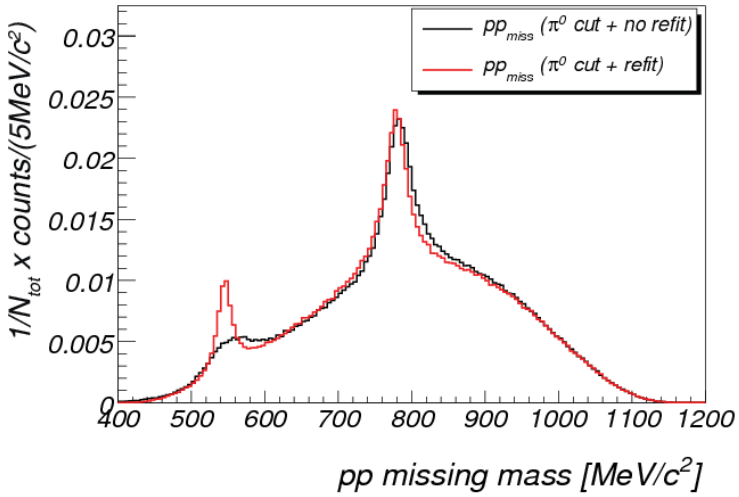

(b) The pp missing mass spectrum. The black curve is obtained using the π^0 missing mass cut and dE/dx selection without applying a kinematic fit. The red line is obtained after applying the kinematic fit in addition to the π^0 cut and the dE/dx selection. The kinematic fit leads to a significant improvement in the signal to background ratio in the region of the η peak.

Figure 4.6

which implies different momentum distributions of the protons and consequently different errors of the measurement.

Instead of applying the π^0 missing mass cut, one may select events using the $p-$value cut as discussed in chapter 3. Figure 4.7(a) shows the $pp\pi^+\pi^-$ missing mass distribution again for three cases:

1. Black line: for all events in which two protons, one π^+, and one π^- were identified using the dE/dx PID method.

2. Red line: for events in which two protons, one π^+, and one π^- were identified using the dE/dx PID method and the kinematic fit converged with a $p-$value larger than 0.16.

3. Blue line: for events in which two protons, one π^+, and one π^- were identified using the dE/dx PID method and the kinematic fit converged with a $p-$value larger than 0.16. The missing mass was calculated using the modified track parameters after the fit and is therefore sharply peaked at the π^0 mass.

As can be seen from the red curve in figure 4.7(a), the $p-$value cut leads to the rejection of most of the background events without using the π^0 cut. However, the missing mass range of accepted events extends to regions far away from the π^0 mass. In figure 4.7(b), three distributions of the pp missing mass are compared:

1. The black curve: obtained by applying the kinematic fit to events selected using the π^0 missing mass cut and the dE/dx PID method without the use of any cut on the $p-$value.

2. Red line: obtained as the black line but using a $p-$value cut of 16% in addition to the π^0 and dE/dx selections.

3. Blue line: obtained using a $p-$value cut of 16% and the dE/dx selection without the application of the π^0 missing mass cut.

As can be seen from the figure, the red curve, corresponding to the π^0 cut in addition to the $p-$value cut exhibit the highest signal to background ratio. The blue curve, corresponding to no π^0 cut, shows a high level of background to the right of the η peak.

Figure 4.8 shows a comparison of four (non-normalized) pp missing mass distributions:

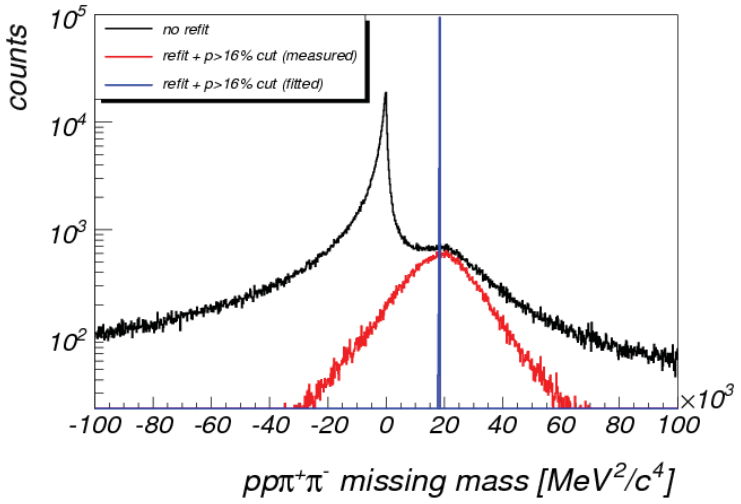

(a) The $pp\pi^+\pi^-$ missing mass distribution: for all events (black). For events having a converging kinematic fit with $p < 0.16$ (mass calculated using measured values (red) and using fitted values (blue)).

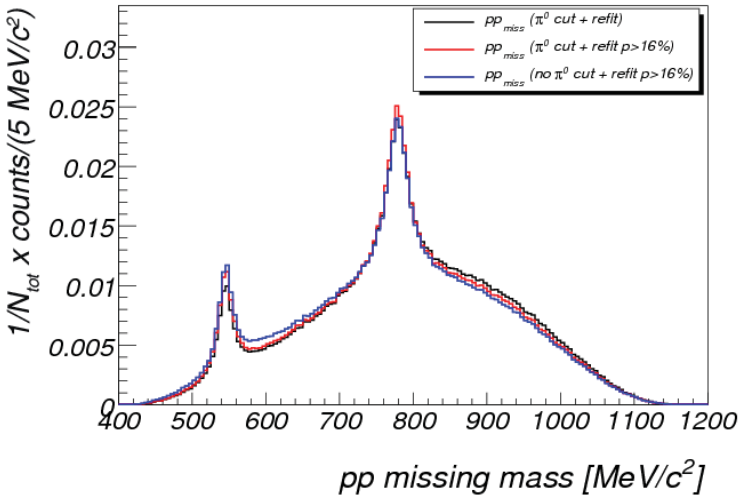

(b) The pp missing mass spectrum after the kinematic fit. The black curve is obtained using the π^0 missing mass cut and dE/dx selection in addition to kinematic fit. The red curve is obtained after applying a $p-$value cut of 16% in addition to the π^0 cut and dE/dx selection . The blue curve is obtained by applying a $p-$value cut of 16 % in addition to the dE/dx selection without using the π^0 missing mass cut. All curves are normalized to unity.

Figure 4.7

- Magenta curve: obtained by applying the kinematic fit to all events of the event ensemble without using the π^0 missing mass cut or a p-value cut.
- Blue curve: obtained by applying the kinematic fit and a p-value cut at 16%. The p-value cut leads to a huge reduction of the background as compared with the magenta curve.
- Black curve: obtained by applying the kinematic fit with no p-value cut on events selected using the π^0 missing mass cut. The π^0 missing mass cut reduces the background by a similar amount as the p-value cut at 16% (compare the blue and black curves). Both curves coincide above 800 MeV/c^2. At lower masses, the π^0 missing mass cut removes more background events than the p-value cut at 16%. Especially around 580 MeV/c^2 (to the right of the η peak) the π^0 missing mass cut removes a large fraction of the background events.
- Red curve: obtained by applying the kinematic fit to events selected using the π^0 missing mass cut and in addition applying a p-value cut at 16%. The combination of both cuts leads to a further reduction of the background.

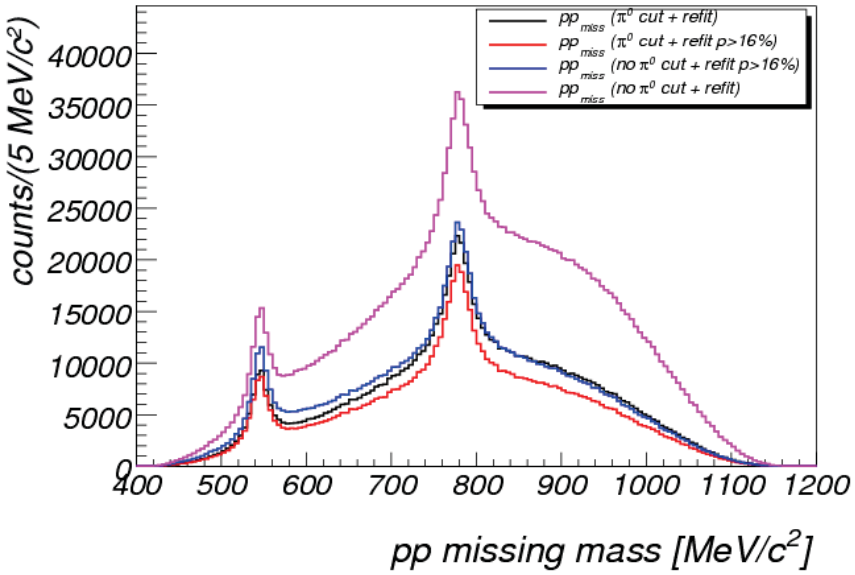

Figure 4.8: The pp missing mass spectrum after the kinematic fit. The magenta curve is obtained by applying the kinematic fit to all events. The blue curve is obtained by applying the kinematic fit to all events and a p-value cut of 16%. The black curve is obtained by applying the kinematic fit with no p-value cut on events selected using the π^0 missing mass cut. The red curve is obtained by applying the kinematic fit and a p-value cut of 16% on events selected using the π^0 missing mass cut.

4.3 Conclusion

In the previous sections, the various results of the kinematic fit algorithm were presented. The application of the kinematic fit is essential for improving the resolution at the η meson mass region. This can be seen in figure 4.6(b). In the same figure, one can also see that the kinematic fit does not affect the shape of the background. In addition, figure 4.7(b) shows that the application of a π^0 missing mass cut and a $p-$value cut leads to better results. Finally, a more complete determination of the error matrix will also lead to better results of the kinematic fit algorithm.

5

Acceptance correction

In this chapter, the correction of measured data for the effects of the spectrometer acceptance *i.e.* the determination of yield losses due to the geometrical setup and efficiency of the spectrometer is discussed. The term *acceptance* is used throughout this work to denote the product of reconstruction efficiency and geometrical acceptance.

For particles which can be detected and identified by one or more types of detectors, the solid angles covered by the active volumes of the detectors define the geometrical acceptance of the spectrometer for those specific particles. The geometrical acceptance can still be a function of *e.g.* particle's momentum and charge.

The reconstruction efficiency is the probability of reconstructing and identifying a particle traversing the active volume of the detectors *i.e.* traveling inside the geometrical acceptance of the spectrometer. The reconstruction efficiency includes the efficiency of the detectors and the efficiencies of the track reconstruction and the particle identification algorithms. It is a function of the particle type, momentum and angles.

If more than one particle are detected in an event, the reconstruction efficiency is -in general- not given by the simple multiplication of single particle efficiencies but may depend on the relative momenta between the particles. Accordingly, the acceptance of a spectrometer is a function of the specific reaction under study. For the same spectrometer, different reactions involving different number of particles in the final state and different kinematical relations between the produced particles correspond to different acceptances.

Therefore, for every reaction under study, the acceptance must be determined as a

function of all possible degrees of freedom (DOF) of the particles in the final state. The number of DOF in the reactions analyzed in this work is discussed in section 5.2.2.

5.1 Steps of acceptance determination

To determine the acceptance of HADES for a specific type of reactions, the following steps are performed:

5.1.1 Event generation

Using the "Pluto: A Monte Carlo Simulation Tool for Hadronic Physics"[F$^+$07] event generator, a large number of events of the reaction under study is produced. The particles in the final state of the reaction are distributed according to phase space calculations. By doing this, a homogeneous distribution of events over all regions of the kinematically allowed phase space is obtained.
One might also include certain models in the particles' production or decay. This will be discussed in more details in section 5.2.

5.1.2 Detector simulation

In the second step, the "GEANT Detector Description and Simulation Tool"[BCG] is used to simulate the interaction of the particles produced in the reactions with the various components of the spectrometer. GEANT simulates various effects like *e.g.* particle decays, electromagnetic interactions and hadronic interactions. Using HADES software for detector response simulation (digitizer), the output of GEANT is translated into hits in the various detectors of the spectrometer similar to the output in the case of measured data.

5.1.3 Particle reconstruction

In this step, the simulated particle trajectories are reconstructed with the help of the same software used for reconstructing the real particles. In this way, one accounts for the systematic effects due to the different algorithms used during the reconstruction of measured data to a large extent. The systematic effects cancel each other when applying the acceptance correction to data.

5.1.4 Acceptance matrix

Finally, the phase space of the final state particles is discretized into several bins such that the expected acceptance variation inside one bin is small enough to be neglected. Then the events reconstructed in step 5.1.3 are sorted according to their respective phase space bin. The acceptance matrix contains, for each phase space bin, the number of reconstructed events inside that specific bin.

Since in step 5.1.1, the events are produced according to a homogeneous phase space density, the acceptance $\mathbb{A}$ for a given phase space bin is obtained according to equation 5.1

$$\mathbb{A} = \frac{n_{rec}}{n_{tot}} \times \frac{\mathrm{vol}_{tot}}{\mathrm{vol}_{bin}} \tag{5.1}$$

where

n_{rec}	is the number of reconstructed events
n_{tot}	is the total number of simulated events
vol_{bin}	is the volume of the bin
vol_{tot}	is the total volume of the allowed phase space

5.2 Model dependent acceptance correction

To obtain the acceptance matrix of HADES for the reactions studied in this work, the model-independent method described in section 5.1 can not be used. This is due to the existence of acceptance holes and due to the large number of degrees of freedom in the final state of the reactions. Both reasons are discussed in more detail in the following sections.

5.2.1 Acceptance holes

Acceptance holes are those parts of phase space which are not accessible by the HADES spectrometer. HADES has zero acceptance for any particle that is emitted from the target region with a laboratory polar angle less than approximately 15°. This means that, one can not fully reconstruct any configuration of final state particles where one or more charged particles are emitted below 15° in the polar angle. In order to correct for such losses, one has to rely on models that describe the reaction under study. When the measured integrated yield is corrected by the simulated integrated acceptance, one assumes that the model describes nature correctly.

The basic model used for the extrapolation to the full phase space -in general- assumes flat phase space distributions for the production and decay of particles. However, before using phase space calculations for the full acceptance correction, differential cross section studies are performed in the measured parts of phase space. If the output of the differential cross section distributions deviates from the phase space calculations, the following steps are performed:

- The deviations of the differential distributions from the phase space calculations are parametrized.
- In the step of event generation (see 5.1.1), the distributions of events are modified such that, the new distributions reflect the parameterization derived from the differential studies.
- The same parametrization is also used in the non-measured regions of the phase space and all steps described in section 5.1 are repeated.

5.2.2 Degrees of freedom (DOF)

In this work, reactions with 5 particles in the final state[1] are studied. Since the mass of each particle is known, momentum DOF are the relevant ones. Hence, we have -in general- 15 DOF in such final states. However, since the momenta of the beam particles are known, one can eliminate 4 degrees of freedom due to the energy and momentum conservation. Hence, the number of DOF in exclusive reactions with 5 particles in the final state is 11.

If chosen properly, one can also integrate over a further DOF (the azimuthal angle ϕ). The integration over ϕ is allowed, because the beam and target used during the experiment are non-polarized which implies a ϕ-symmetry of the results. Hence, the effective number of DOF for the exclusive reactions studied in this work is 10.

As discussed in 5.1.4, when correcting the measured yields, they are sorted according to their respective phase space bins. The dimensions of such space are the total number of effective DOF. Assuming that each dimension is divided into 3 bins, the total number of bins would be $3^{10} = 59049$ bins. As will be shown in chapter 9, the number of reconstructed events with an ω meson produced is about 80000,

[1] $p + p \longrightarrow pp\pi^+\pi^-\pi^0$

those with an η meson produced are about 35000. This statistics is too low to fill a matrix of 59049 bins.

In order to overcome the problem of low statistics, we again rely on models describing the decay of short living particles to reduce the effective number of DOF. Hence, the number of particles in the final state is reduced from 5 to 3. Consequently, the effective number of degrees of freedom becomes 4[1].
In the case of ω-meson decay, we apply a model of the hadronic 3-body decays of light vector mesons[LL09] which agrees very well with experimental measurements by the ASTERIX collaboration[W$^+$93]. For the decay of η mesons, we take the experimental result obtained by the crystal barrel collaboration [A$^+$95] on the η-decays into three pions.

5.2.2.1 Chosen DOF

Our final choice of kinematical degrees of freedom are not the momenta of single particles, but rather invariant masses and angles. Table 5.1 shows the DOF selected in this work. Here, η is used as an example. For ω mesons, the same table applies.

Table 5.1: Overview of the selected DOF

DOF		Description	
I	$cos\theta^{\eta}_{CM}$	the cosine of the angle -relative to the beam axis- of η in the reaction center-of-mass frame (C.M.). This is a common observable in theoretical calculations.	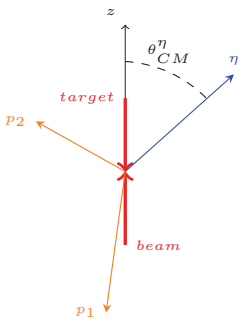

Continued on next page

[1]The reactions are then reduced to $p + p \longrightarrow pp\omega/\eta$ instead of $p + p \longrightarrow pp\pi^+\pi^-\pi^0$

Table 5.1 – continued from last page

DOF		Description	
II	$cos\theta^p_{pp}$	the cosine of the angle -relative to the beam axis- of p_1 in the rest frame of $p_1 + p_2$. In particle production according to phase space, this observable is uniformly distributed.	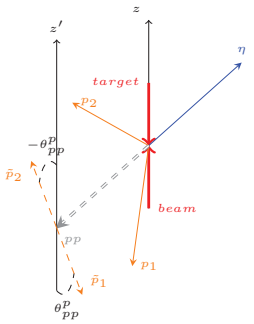
III	$M_{p_1\eta}$	The invariant mass of $\eta + p_1$. Used together with $M_{p_2\eta}$ or M_{pp} to make Dalitz plots (search for resonant production, final state interactions, etc.).	
IIIa	$M_{p_2\eta}$	The invariant mass of $\eta + p_2$.	
IV	M_{pp}	The invariant mass of $p_1 + p_2$.	

The acceptance correction is done in 4 dimensions (two invariant masses and two angles). The choice of the protons in II, III, IIIa is arbitrary. Therefore, for any calculation involving these quantities, the quantity is calculated twice, each time using one of the two protons. This leads to a symmetry of specific results.

5.3 The HADES acceptance

In this section, the spectrometer acceptance as a function of some of the DOF described in section 5.2.2.1 is shown. Step 5.1.1 is performed based on phase space calculations and the distributions of events reconstructed in step 5.1.3 is checked.

Table 5.2 and 5.3 show the comparison of the event distributions in step 5.1.1 and after step 5.1.3 for the case of η and ω mesons respectively. In appendix A a complete set of plots is given for reference purposes.

Table 5.2: The acceptance of η mesons as a function of different observables. The figures show the number of simulated events in 4π (Pluto input) and the corresponding number of reconstructed events (HADES acceptance) as a function of the selected observable.

DOF	Pluto input	HADES acceptance
$cos\theta^{\eta}_{CM}$	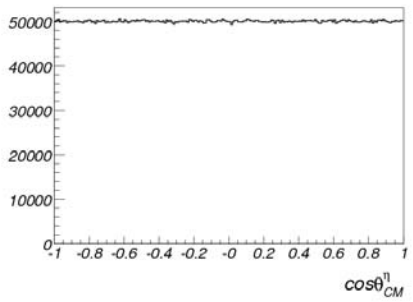	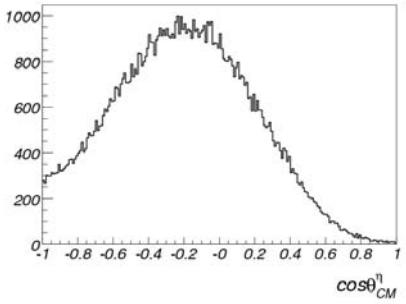
$cos\theta^{p}_{pp}$	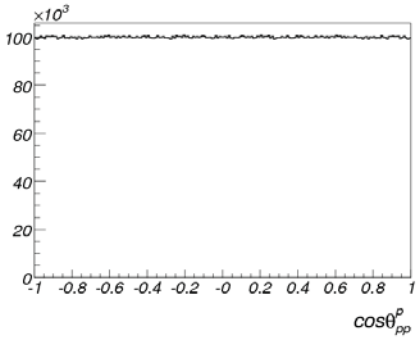	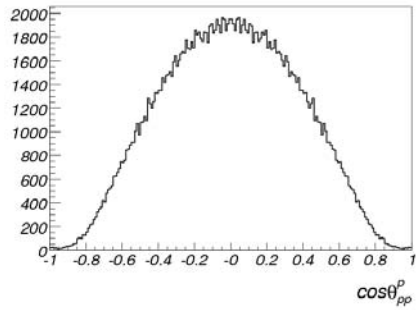
$M^2_{p\eta}$	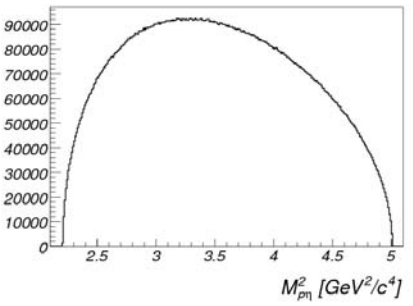	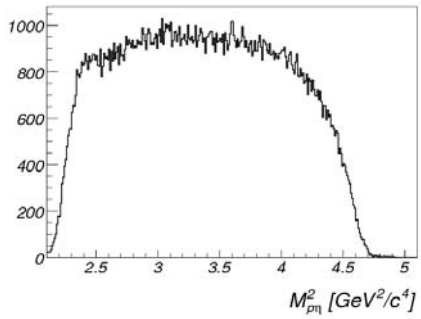

Continued on next page

Table 5.2 – continued from last page

DOF	Pluto input	HADES acceptance
M^2_{pp}	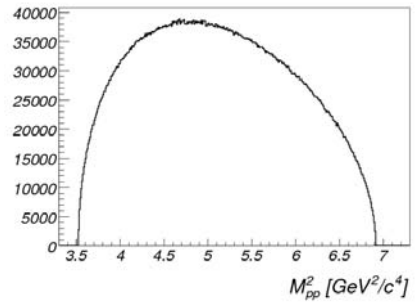	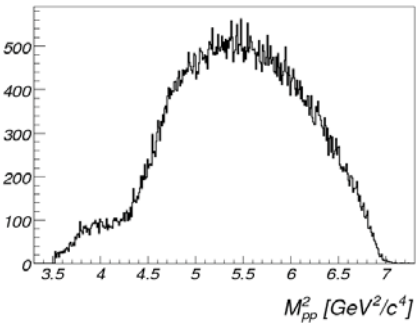
$cos\theta^p_{pp}$ versus $cos\theta^\eta_{CM}$	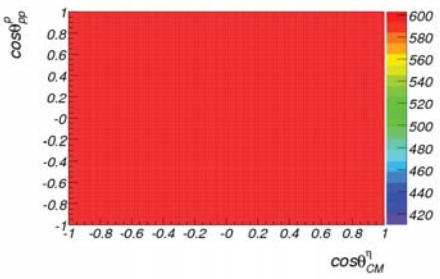	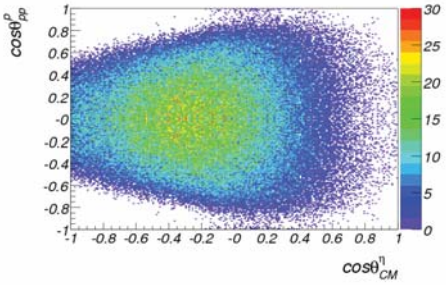
M^2_{pp} versus $M^2_{p\eta}$	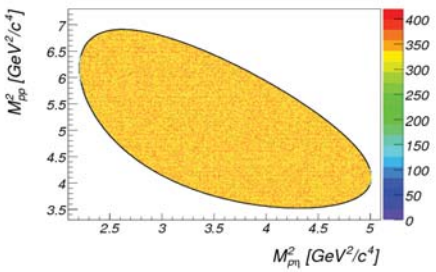	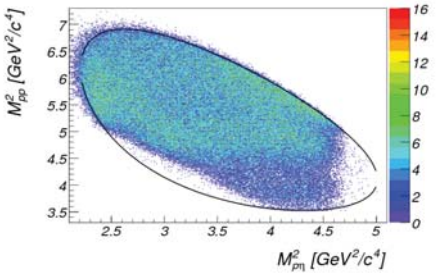

Table 5.3: The acceptance of ω mesons as a function of different observables. The figures show the number of simulated events in 4π (Pluto input) and the corresponding number of reconstructed events (HADES acceptance) as a function of the selected observable.

DOF	Pluto input	HADES acceptance
$cos\theta^{\omega}_{CM}$	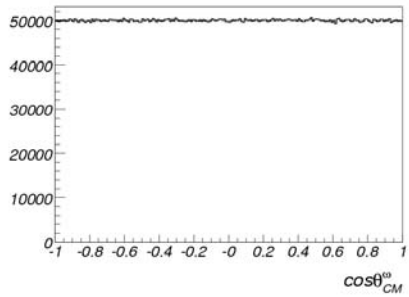	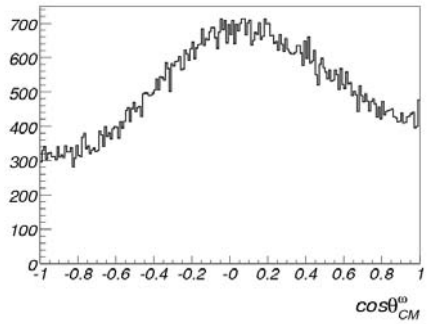
$cos\theta^{p}_{pp}$	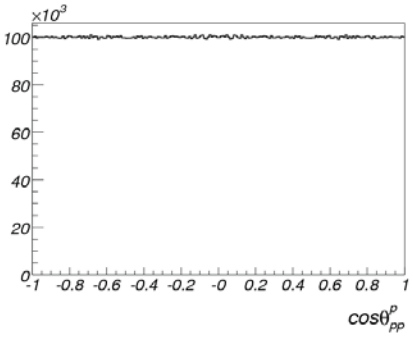	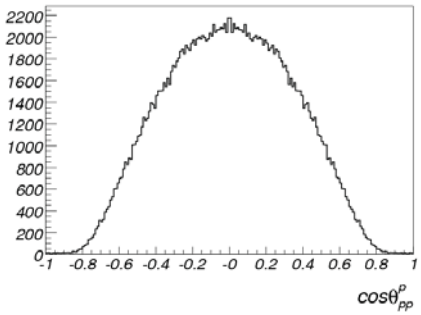
$M^2_{p\omega}$	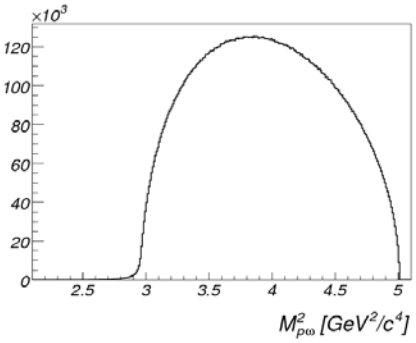	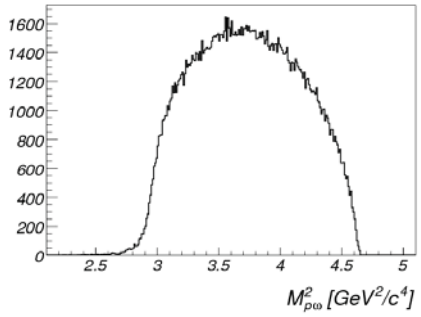

Continued on next page

Table 5.3 – continued from last page

DOF	Pluto input	HADES acceptance
M^2_{pp}	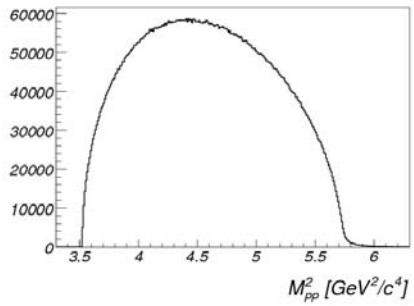	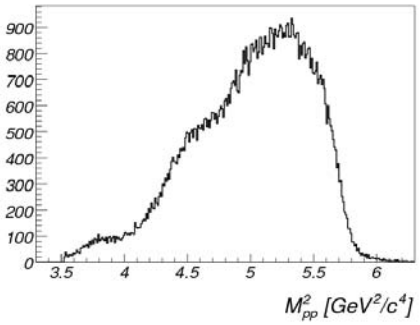
$cos\theta^p_{pp}$ versus $cos\theta^\omega_{CM}$	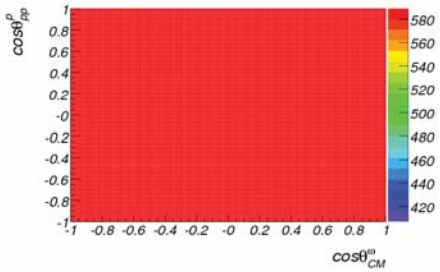	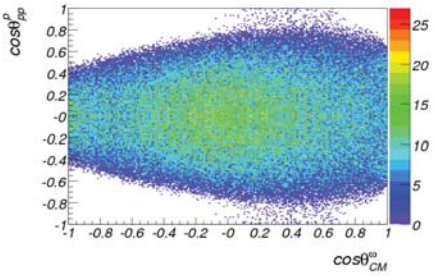
M^2_{pp} versus $M^2_{p\omega}$	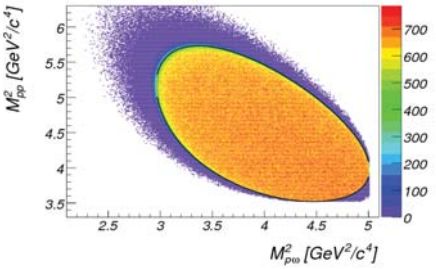	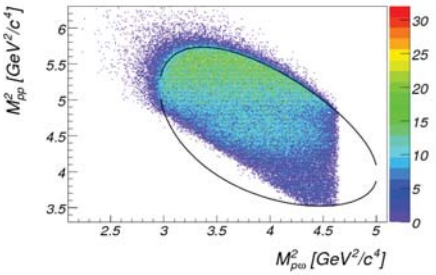

The plots in tables 5.2 and 5.3 and in more details A.1 and A.2 include regions of the accessible phase space with zero acceptance. In order to ensure that these acceptance holes do not affect the ability of HADES to reconstruct angular distributions deviating from the flat phase space ones, studies of the HADES acceptance for various input distributions are presented in the next chapter.

6

Acceptance studies

In this chapter, the ability of HADES to reconstruct various distributions of the particles produced in the reactions under study[1] is discussed. In chapter 5 section 5.3, it was shown that the HADES acceptance[2] does not cover all regions of the phase space accessible by the particles in the final state of the reactions. This leads to the question whether the regions of vanishing acceptance affect the obtained results *i.e.* the reconstructed distributions. Looking at the Dalitz plots (M^2_{pp}versus$M^2_{p\eta}$ and M^2_{pp}versus$M^2_{p\omega}$) one can easily conclude that any $p\eta$ or $p\omega$ resonance with a mass higher than 2.15 GeV/c^2 can not be detected, but the influence of the regions of vanishing acceptance on the reconstructed angular distributions needs further investigations.

In the following sections, the effect of the zero acceptance regions on the reconstruction of angular distributions in $\theta^{\eta/\omega}_{CM}$ and θ^{p}_{pp} is shown. This includes qualitative analyses addressing the shape of the reconstructed distribution as well as quantitative analysis addressing the determined cross sections. The procedure is explained in detail for the case of the ω.

6.1 Studies of ω meson production

To estimate the effect of the regions of vanishing acceptance on the reconstruction of angular distributions in the case of ω mesons, three types of simulations are done:

[1] $pp \longrightarrow pp\eta/\omega$

[2] Acceptance is defined as the product of reconstruction efficiency and geometrical acceptance.

- **SimFlat:** phase space production: this serves as a reference for the other two simulations
- **SimCos8:** production of ω and protons according to strongly anisotropic angular distributions which are peaked in the region of low or vanishing acceptance
- **SimCos2:** production of ω and protons according to slightly anisotropic angular distributions

For the strong anisotropic distribution, we implement a function $f_{II}(\theta) = 1 + 4cos^8(\theta)$ and for the slightly anisotropic distribution, we implement a function $f_{III}(\theta) = 1 + cos^2(\theta)$ where θ denotes θ^{ω}_{CM} and θ^{p}_{pp}. Both functions have their maximum at $cos\theta = \pm 1$ where the value of f_{II} reaches 5 times its value at $cos\theta = 0$, whereas that of f_{III} reaches only 2 times its value at $cos\theta = 0$. Moreover, f_{II} varies very slowly with $|cos\theta|$ but then increases rapidly near $cos\theta = 1$, while f_{III} starts to increase much earlier.
In full phase space (4π), the distribution of the angles introduced in section 5.2.2.1 is isotropic for SimFlat (phase space production). Dividing the distribution of angles from SimCos8 or SimCos2 (anisotropic production) by the distribution from SimFlat yields the original anisotropic shapes. For the reconstructed events, all such distributions are modified by the acceptance of the spectrometer. Therefore, to obtain the real distribution in 4π, the distribution of reconstructed events is divided by that of reconstructed events from SimFlat and thereby is corrected for the spectrometer acceptance. However, the regions of vanishing acceptance and the non homogeneity of the acceptance may modify these *corrected* spectra. These effects are investigated with the help of SimCos8 and SimCos2.

In SimFlat, SimCos8 and SimCos2, the population of events in the Dalitz plot is homogeneous. Hence, one can integrate over the Dalitz variables and consider only the two angles.

6.1.1 SimCos8: strong anisotropic distributions

In figure 6.1(a), the ratio of SimCos8 to SimFlat is shown as a function of $cos\theta^{\omega}_{CM}$ both in 4π (Pluto) and inside HADES acceptance. The distribution in 4π is given by the blue curve. The red curve represents the distribution as reconstructed inside

the HADES acceptance. The figure shows that the shape of the reconstructed distribution is similar to the input one. Figure 6.1(b) shows the ratio of the red curve in figure 6.1(a) to the blue one. The ratio of both curves doesn't vary considerably. Hence, even if the real data exhibit such a strong anisotropic angular distribution, the reconstructed one would reflect the real distribution fairly well. However, the ratio of both curves is less than one which means that the fraction of non reconstructed events in SimCos8 –relative to the total number in 4π– is larger than the fraction of non reconstructed events in SimFlat. This is due to the fact that in SimCos8 the distribution of events is peaked in the region of vanishing acceptance.

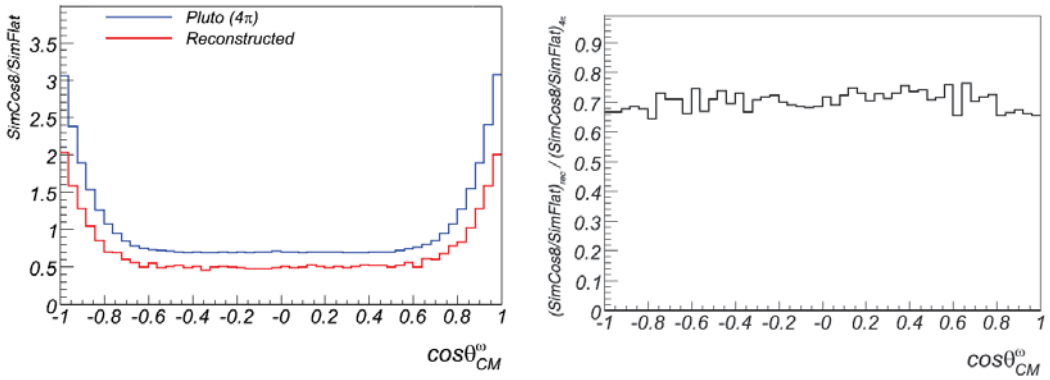

(a) Angular distribution of ω: reconstructed (red) and input (blue)

(b) Ratio of the two curves of fig. 6.1(a)

Figure 6.1

The white area in figure 6.2(a) shows the region of vanishing acceptance. The figure shows that only for $|cos\theta^{p}_{pp}| \leq 0.4$, the whole range of $cos\theta^{\omega}_{CM}$ is covered. If the ω angular distribution is determined only in the range of $|cos\theta^{p}_{pp}| \leq 0.4$, the two curves of figure 6.1(a) overlap as shown in figure 6.2(b).

Figure 6.2(a) also shows that no region of $cos\theta^{\omega}_{CM}$ covers the whole range of $cos\theta^{p}_{pp}$. One can only obtain reliable information about the distribution of particles as a function of $cos\theta^{p}_{pp}$ in the range $cos\theta^{p}_{pp} \leq 0.6$. This range is too narrow to conclude about the distribution up to $|cos\theta^{p}_{pp}| = 1$. Nevertheless and for the sake of completeness, figure 6.3(a) shows the ratio of SimCos8/SimFlat integrated over the whole phase space and in figure 6.3(b) the same ratio for $0 \leq cos\theta^{\omega}_{CM}| \leq 0.9$

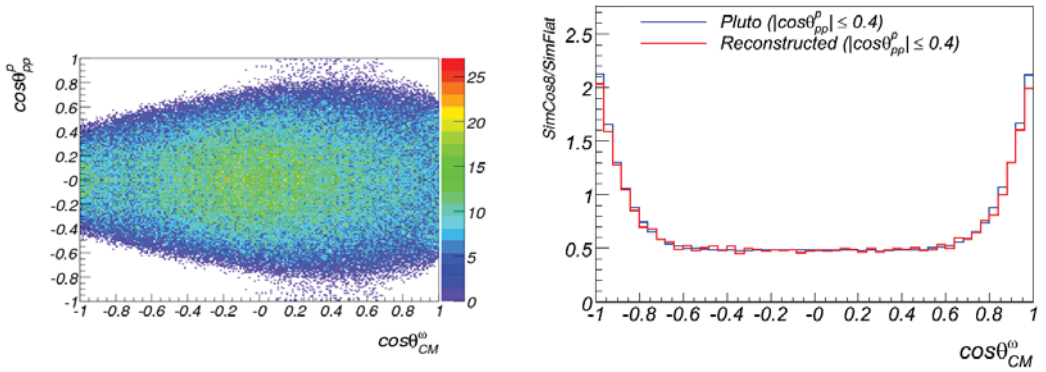

(a) Number of reconstructed events as a function of $cos\theta^{p}_{pp}$ versus $cos\theta^{\omega}_{CM}$. The corresponding input distribution (Pluto) can be found in table 5.3. Note the range of $cos\theta^{p}_{pp}$ for which the whole range of $cos\theta^{\omega}_{CM}$ is covered.

(b) Angular distribution of ω for $cos\theta^{p}_{pp} \leq 0.4$: reconstructed (red) and input (blue)

Figure 6.2

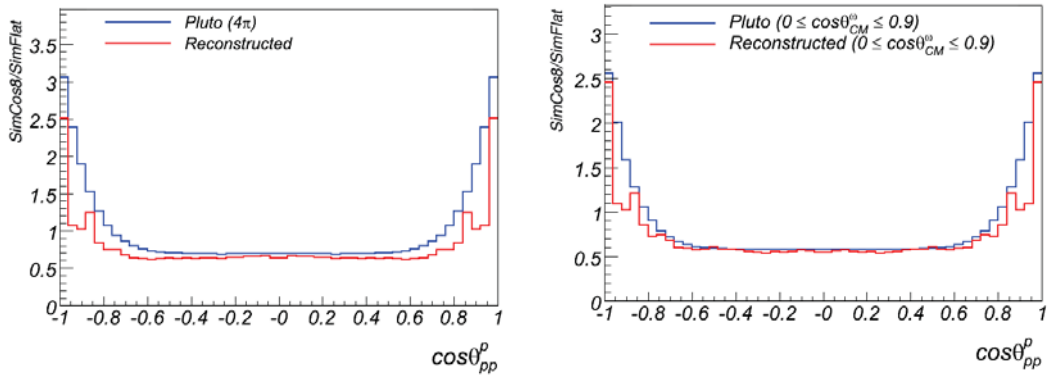

(a) Proton angular distribution: input (blue) versus reconstructed (red).

(b) Proton angular distribution (selected range): input (blue) versus reconstructed (red).

Figure 6.3

6.1.2 SimCos2: slightly anisotropic distributions

As mentioned before, the function f_{II} is almost flat near to zero and increases rapidly towards one. f_{III} was also introduced which starts increasing already at zero. In this section, we check whether HADES acceptance allows to differentiate between both functions.
In figure 6.4(a),the ratio of SimCos2 to SimFlat is shown as a function of $cos\theta^{\omega}_{CM}$ both in 4π and inside HADES acceptance. Also, in figure 6.4(b), the ratio of the blue curve of figure 6.4(a) to the red one is plotted.

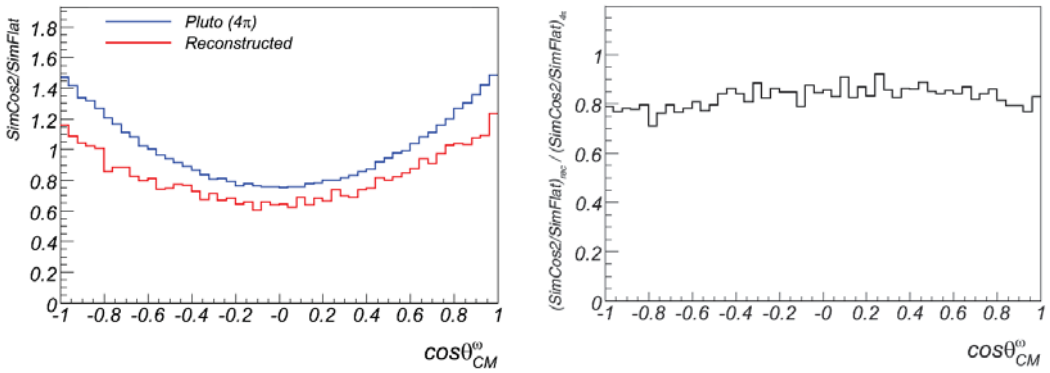

(a) Angular distribution of ω: reconstructed (red) and input (blue)

(b) Ratio of the two curves of fig. 6.4(a)

Figure 6.4

As in the case of SimCos8, the ratio in figure 6.4(b) doesn't vary considerably, which means that reconstructed angular distributions reflect the input/real distribution. If events were selected within the range $|cos\theta^{p}_{pp}| \leq 0.4$, the distribution shown in figure 6.5 is obtained which overlaps with the input distribution in the same range.

In figure 6.6, the ratio of SimCos2/SimFlat as a function of $cos\theta^{p}_{pp}$ is plotted. Although the input function f_{III} varies over the whole range, figure 6.6(b) shows that such variation can be reliably reproduced only in the range of $cos\theta^{p}_{pp} \lesssim 0.7$.

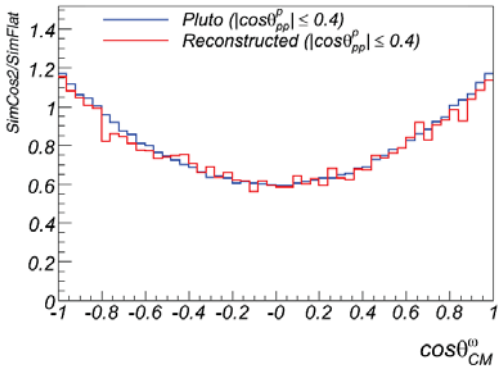

Figure 6.5: Angular distribution of ω for $cos\theta^p_{pp} \leq 0.4$: reconstructed (red) and input (blue).

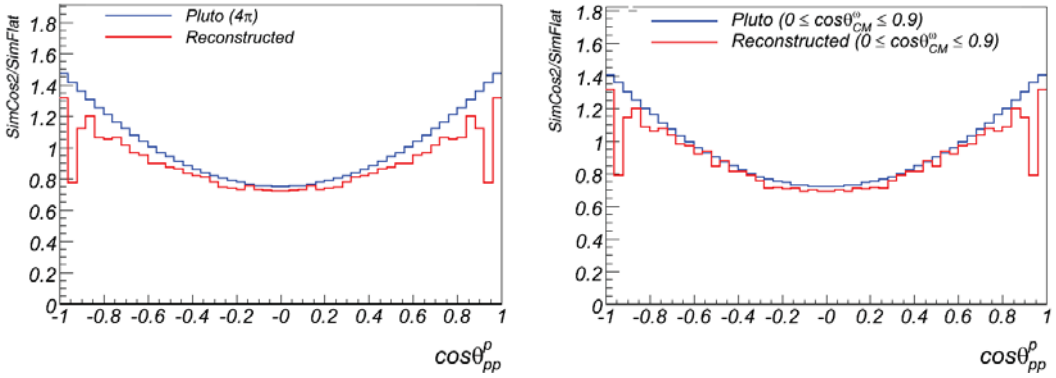

(a) Proton angular distribution: input (blue) versus reconstructed (red)

(b) Proton angular distribution (selected range): input (blue) versus reconstructed (red).

Figure 6.6

6.2 Studies of η meson production

Studying the acceptance of η mesons and the ability to reconstruct various angular distributions yields similar results to the results of section 6.1 for ω mesons. The shape of the reconstructed η angular distribution is similar to the input one. When choosing the proper range of θ^p_{pp}, the input and reconstructed curves almost overlap. A small difference to the ω case is however, that the acceptance of η in the forward direction is very small. This means that one should rely on the backward part of the spectrum ($cos\theta^\eta_{CM} \lesssim 0.8$) when reconstructing the angular distribution. For θ^p_{pp} the result is very similar to the case of ω where one can reliably reconstruct the

distribution in the range of ($|cos\theta^p_{pp}| \lesssim 0.7$).

Figures 6.7, 6.8 and 6.9 show similar plots to those of section 6.1 in the case of η mesons.

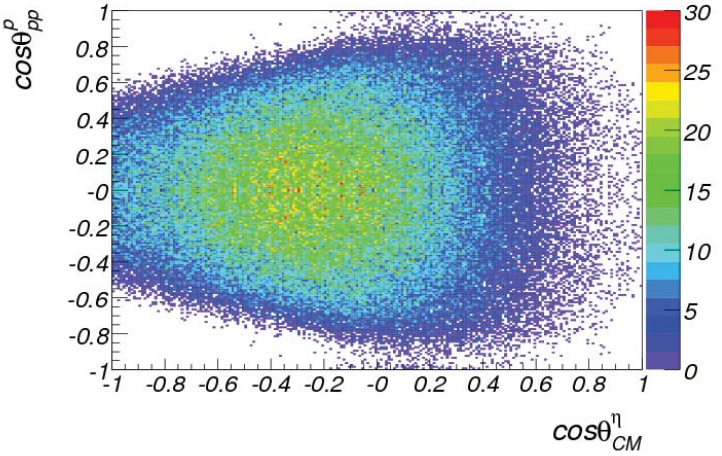

Figure 6.7: Number of reconstructed events as a function of $cos\theta^p_{pp}$ versus $cos\theta^\eta_{CM}$. The corresponding input distribution (Pluto) can be found in table 5.2. Note the range of $cos\theta^p_{pp}$ for which the backward range of $cos\theta^\eta_{CM}$ is totally covered.

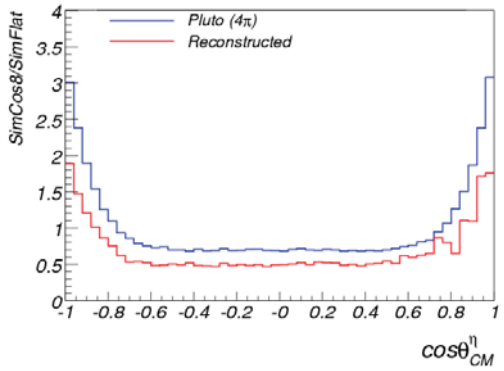

(a) Angular distribution of η: reconstructed (red) and input (blue).

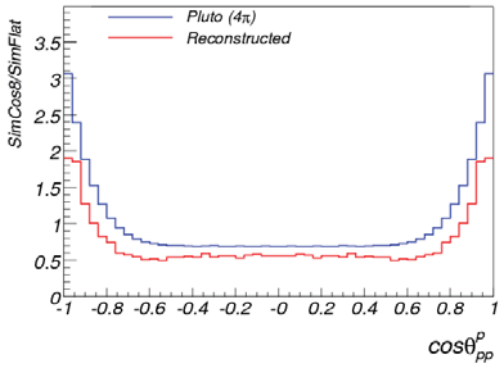

(b) Proton angular distribution: input (blue) versus reconstructed (red).

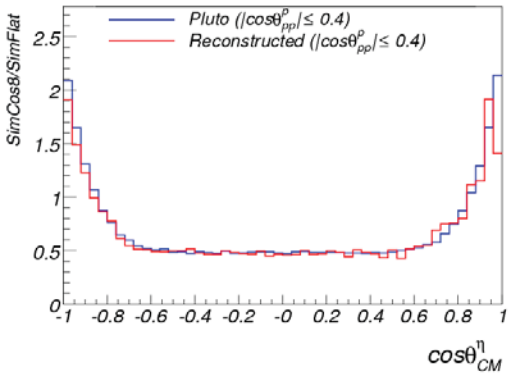

(c) Angular distribution of η (selected range): reconstructed (red) and input (blue).

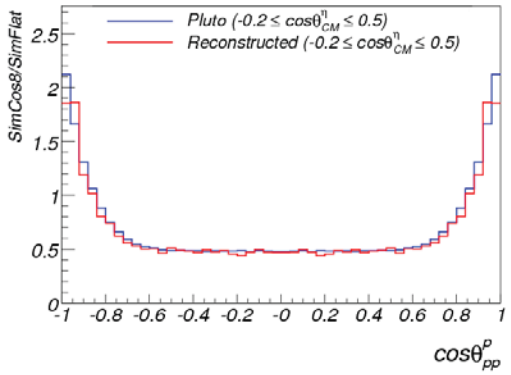

(d) Proton angular distribution (selected range): input (blue) versus reconstructed (red).

Figure 6.8

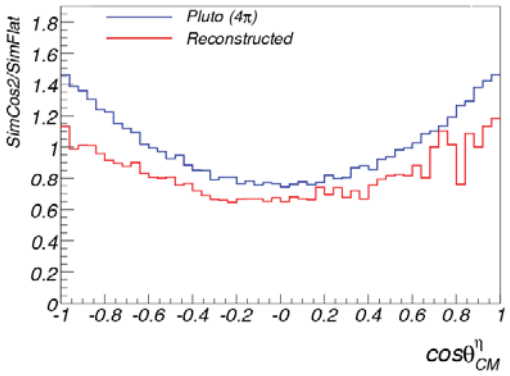

(a) Angular distribution of η: reconstructed (red) and input (blue).

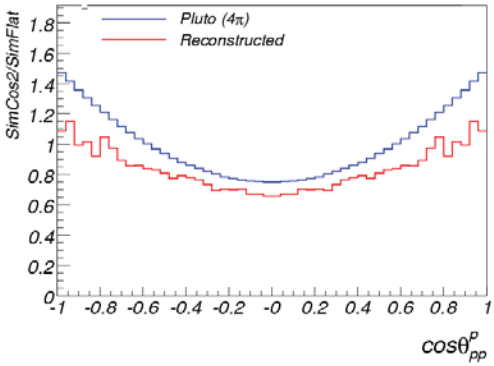

(b) Proton angular distribution: input (blue) versus reconstructed (red).

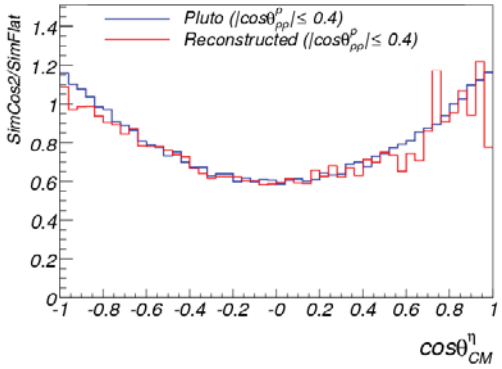

(c) Angular distribution of η (selected range): reconstructed (red) and input (blue).

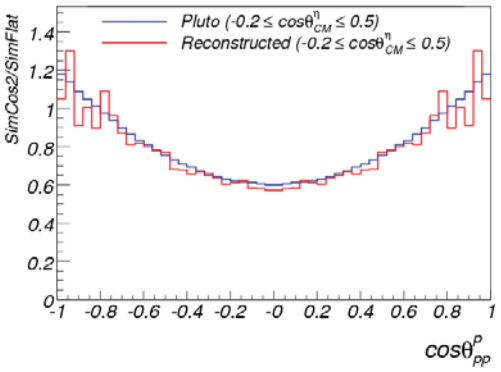

(d) Proton angular distribution (selected range): input (blue) versus reconstructed (red).

Figure 6.9

6.3 Conclusion

Sections 6.1 and 6.2 show that HADES is able to reliably reconstruct the angular distributions of ω/η mesons in the center-of-mass of the reactions $pp \longrightarrow pp\omega/\eta$ regardless of the angular distribution of protons. It was also demonstrated that the integration over regions of zero acceptance might lead to a wrong determination of the yield. For this reason, we check in this section if the acceptance as a function of the two Dalitz masses versus the ω/η production angle contains regions with zero acceptance.

Figure 6.10 shows the acceptance of HADES for the reaction $pp \longrightarrow pp\omega$ as a function of $M^2_{p\omega}$ versus $cos\theta^{\omega}_{CM}$ and M^2_{pp} versus $cos\theta^{\omega}_{CM}$.

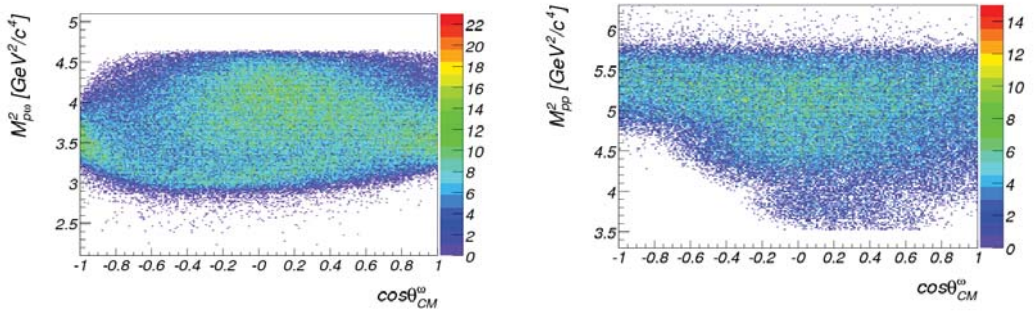

(a) Number of reconstructed events as a function of $M^2_{p\omega}$ versus $cos\theta^{\omega}_{CM}$. The corresponding input distribution (Pluto) can be found in table A.2.

(b) Number of reconstructed events as a function of M^2_{pp} versus $cos\theta^{\omega}_{CM}$. The corresponding input distribution (Pluto) can be found in table A.2.

Figure 6.10

As can be seen from figure 6.10(a), the range of $0 \leq cos\theta^{\omega}_{CM} \leq 1$ is almost fully covered at any value of $M^2_{p\omega}$. However, figure 6.10(b) shows that the same range is only fully covered for values of M^2_{pp} higher than 4 GeV^2/c^4. Accordingly, for the reconstruction of the angular distribution of ω mesons in the center of mass, we choose the forward hemisphere and select the protons within the ranges: $|cos\theta^{p}_{pp}| \leq 0.4$ and $M^2_{pp} \geq 4\ GeV^2/c^4$. One should note that the physics implies that angular distributions in the center of mass are symmetric around zero. Hence, it is enough to measure them in one hemisphere.

Figure 6.11 shows the acceptance of HADES as a function of $M^2_{p\eta}$ versus $cos\theta^{\eta}_{CM}$ and M^2_{pp} versus $cos\theta^{\eta}_{CM}$. The backward hemisphere is almost fully covered for all

values of $M^2_{p\eta}$. However, it is only covered for values of M^2_{pp} greater than about 5.5 GeV^2/c^4. Accordingly, we reconstruct the angular distribution of η mesons in the backward hemisphere selecting protons in the ranges $|cos\theta^p_{pp}| \leq 0.4$ and $M^2_{pp} \geq 5.5\ GeV^2/c^4$.

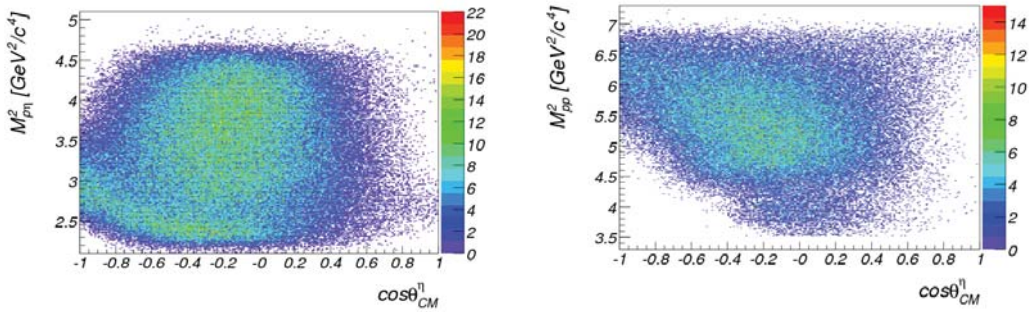

(a) Number of reconstructed events as a function of $M^2_{p\eta}$ versus $cos\theta^\eta_{CM}$. The corresponding input distribution (Pluto) can be found in table A.1.

(b) Number of reconstructed events as a function of M^2_{pp} versus $cos\theta^\eta_{CM}$. The corresponding input distribution (Pluto) can be found in table A.1.

Figure 6.11

As discussed in sections 6.1 and 6.2, the reconstruction of the proton angular distribution is restricted to the range $|cos\theta^p_{pp}| \lesssim 0.7$. The missing information about the distribution in the range between $0.7 \geq |cos\theta^p_{pp}| \leq 1$ lead to an uncertainty in the obtained results of the total and differential cross sections. The results are presented in chapter 9.

7

Cross section determination and absolute normalization

In chapter 5, the correction of measured yields for the effects of spectrometer acceptance was presented. In this chapter, further corrections and normalization factors which are applied in order to determine the cross section for a given reaction are discussed. The factors are summarized as follows.

1. Downscaling factor
2. Branching ratio
3. Proton-proton elastic reaction cross section
4. Trigger efficiency

In the following sections, each of these corrections is discussed in detail.

7.1 Downscaling factor

The setup of the HADES experiment includes several trigger schemes. Each one of the different schemes is designed to select a specific type of physics reactions. Depending on the cross section and importance of the specific reaction, its corresponding trigger is suppressed by a certain factor called the "downscaling factor". When analyzing the collected data, events triggered by a certain trigger scheme are selected. Then, the determined yields are corrected for the corresponding downscaling factor.

7.2 Branching ratio

The aim of this thesis is to determine differential and total cross sections for the reactions $pp \longrightarrow pp\omega/\eta$. However, the $\omega/\eta-$mesons are not reconstructed directly. Instead, they are reconstructed via their decay into $\pi^+\pi^-\pi^0$. Hence, the ratio of the total number of produced $\omega/\eta-$mesons to the number of reconstructed ones is equal to the reciprocal of the branching ratio into the $\pi^+\pi^-\pi^0$ decay channel. The branching ratios are published and updated yearly by the particle data group [N$^+$10].

7.3 Normalization to the elastic cross section

To determine the cross section of a given reaction, one has to precisely know the beam flux during the experiment. Alternatively, one can normalize the measured yields to another - well-known - reaction cross section. For proton-proton reactions measured by HADES, the cross section for a given reaction ($\sigma_{4\pi}^{reaction}$) is normalized to the proton-proton elastic reaction cross section as given by equation 7.1.

$$\sigma_{4\pi}^{reaction} = \mathbb{N}_f^{el} \times N_{4\pi}^{reaction} \tag{7.1}$$

where

$N_{4\pi}^{reaction}$	is the corresponding (corrected) number of events
$\mathbb{N}_f$	is the elastic normalization factor

and $\mathbb{N}_f$ is given by equation 7.2.

$$\mathbb{N}_f = \frac{\sigma_{4\pi}^{el}}{N_{4\pi}^{el}} = \frac{\sigma_{acc}^{el}}{N_{acc}^{el}} \tag{7.2}$$

where

$\sigma_{4\pi}^{el}$	is the cross section for the elastic interaction
$N_{4\pi}^{el}$	is the (corrected) number of elastic events
σ_{acc}^{el}	is the fraction of the cross section within the geometrical acceptance.
N_{acc}^{el}	is the corresponding number of elastic events

The right part of equation 7.2 represents the correction of elastic events for the geometrical acceptance. In equation 7.1, $N_{4\pi}^{reaction}$ includes the corrections for

geometrical acceptance, reconstruction efficiency, downscaling, and branching ratios. Whereas, in equation 7.2, N_{acc}^{el} only includes the correction for downscaling and reconstruction efficiency. In the following subsection,the determination of the normalization factor is discussed.

7.3.1 Determination of the elastic normalization factor[1]

7.3.1.1 Determination of N_{acc}^{el}

To determine N_{acc}^{el},the events triggered by the dedicated elastic scattering trigger scheme (M2) are analyzed. The known reaction kinematics (refer to [Rus06]) impose certain constraints on the angles of the scattered protons in an elastic process. Equations 7.3 and 7.4 must be fulfilled for the outgoing protons in elastic scattering.

$$|\phi_1 - \phi_2| = \pi \tag{7.3}$$

$$cot\theta_1 \times cot\theta_2 = \gamma_{cm}^2 \tag{7.4}$$

where

ϕ_1, ϕ_2	are the laboratory azimuthal angles of the two protons.
θ_1, θ_2	are the laboratory polar angles of the two protons.
γ_{cm}	is the relativistic gamma of the center-of-mass system -of the two protons- relative to the laboratory system.

Figure 7.1 shows the distribution of M2 triggered events -for a sample of files- as a function of $|\phi_1 - \phi_2|$ and $cot\theta_1 \times cot\theta_2$. A clear peak is visible at the expected position according to equations 7.3 and 7.4 with a large signal-to-background ratio. Integrating the peak of figure 7.1 does not give the value of N_{acc}^{el} directly. One still needs to correct the obtained value for the spectrometer efficiency. In order to determine the efficiency of the spectrometer for elastic reactions, PLUTO is used to generate elastic events which are then run through the full simulation and reconstruction chain. The ratio of the reconstructed number to the input one -within HADES geometrical acceptance- gives the efficiency of the spectrometer for the reconstruction of elastic events. Figure 7.2 shows the PLUTO output (brown line) and the reconstructed distribution (red curve) as a function of $cos\theta_{cm}$.

[1]The determination of the elastic normalization factor was done by A. Rustamov

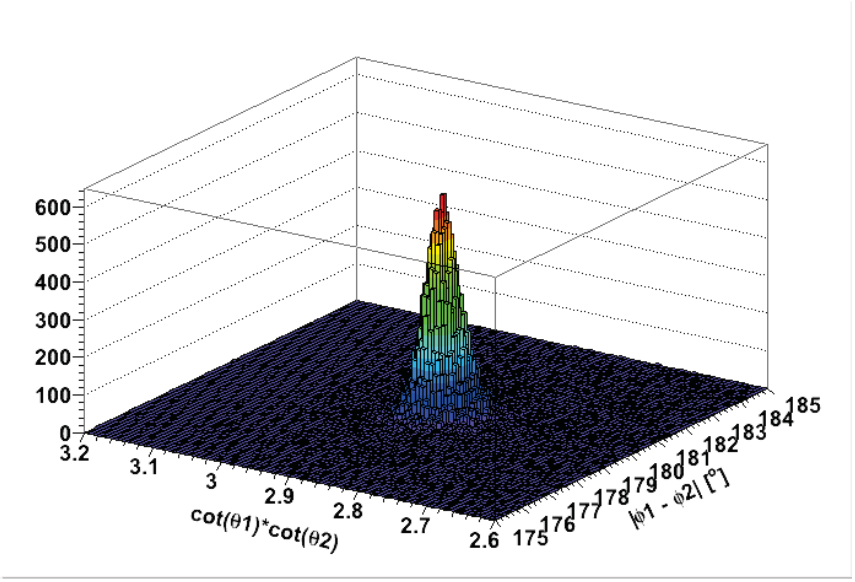

Figure 7.1: The distribution of elastic events (for a sample of files) as a function of $|\phi_1 - \phi_2|$ and $cot\theta_1 \times cot\theta_2$. A clear peak is visible at the expected position.

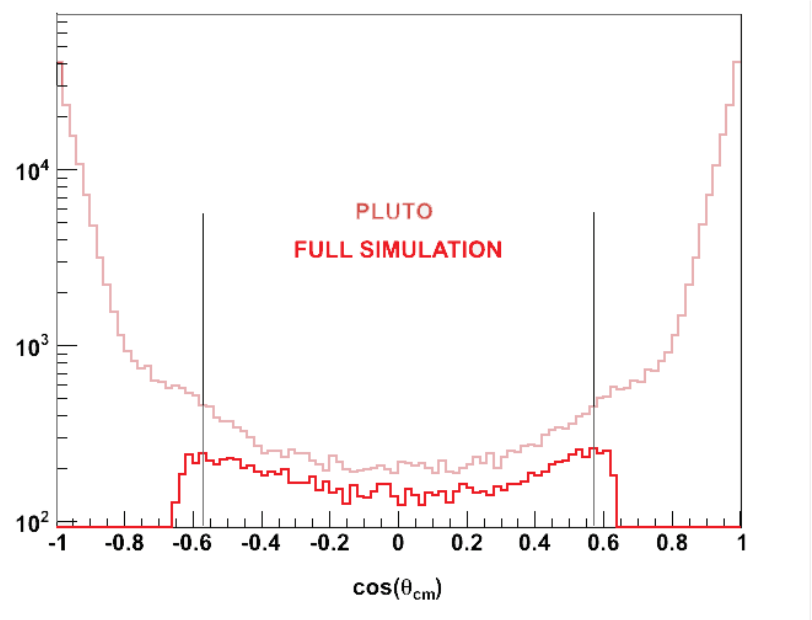

Figure 7.2: The distribution of elastic events –as a function of the cosine of the center of mass angle– in PLUTO (brown) compared to reconstructed events (red). The efficiency factor is calculated in the region between the two vertical lines.

Knowing the number of reconstructed events and the efficiency factor, one can calculate N_{acc}^{el}.

7.3.1.2 Determination of σ_{acc}^{el}

The proton-proton data analyzed in this work were collected at beam kinetic energy of 3.5 GeV. This beam energy corresponds to a beam momentum (P_L) of 4.34 GeV/c. In figure 7.3, the output of PLUTO for the distribution of elastic events at $P_L = 4.34$ GeV/c (black curve) is shown as a function of the center of mass angle. In the same figure, measurements of the elastic scattering cross section published by Kammerud *et. al.* [K$^+$71] are presented. The measured data points were collected at beam momenta of 4.0 (light green) and 4.5 GeV/c (grey).

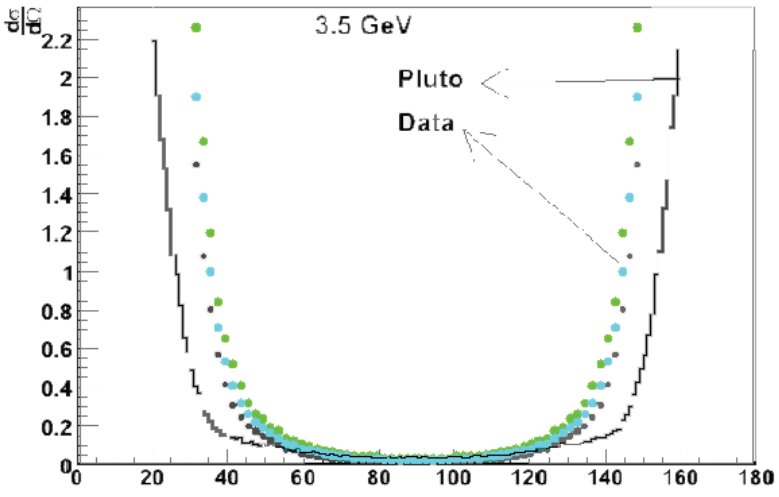

Figure 7.3: The cross section of proton-proton elastic interactions as a function of the c.m. angle. The green points were measured at a beam momentum of 4.0 GeV/c while the grey points were measured at a beam momentum of 4.5 GeV/c. The light blue points represent the mean value of both measurements. The solid line show the result of the cross section extrapolation as implemented in Pluto.

Obviously, the PLUTO extrapolation to $P_L = 4.34$ GeV/c does not fit into the measurements trend. For this reason, instead of relying on PLUTO for the estimation of σ_{acc}^{el}, the mean value of both measurements (light blue points) is taken as a first approximation of the cross section distribution at $P_L = 4.34$ GeV/c.

Integrating the mean curve within the range of center of mass angles covered by the HADES experiment ($55° \leq \theta_{cm} \leq 125°$) yields the first approximation to the value of σ_{acc}^{el}.
A more precise value of σ_{acc}^{el} should be obtained by studying the systematic behavior of the proton-proton elastic cross section in the range of beam momenta of few GeV/c. This would allow for gaining a better approximation to the elastic cross section at a beam momentum of 4.34 GeV/c.

7.4 Relative trigger efficiency

In the scope of this work, only events containing 4 charged tracks (p, p, π^+, and π^-) were selected and analyzed. All of these events were triggered by the minimum bias trigger scheme of HADES (M3 trigger). The M3 scheme triggers whenever three or more particles hit the TOF and/or TOFino scintillators (recall chapter 2). As mentioned in section 7.3, the elastic events were triggered by a different trigger scheme, namely the M2 trigger. The M2 trigger requires two or more charged particles to hit the TOF/TOFino wall.

Since the data yields of events triggered by the M3 scheme are normalized to the number of elastic events which are triggered by the M2 scheme, one should eventually correct for the efficiency difference of both schemes. However, in section 7.4.1, it is shown that the triggering efficiency for a single particle is very close to 100%.
Assuming the single particle triggering efficincy to be 99%, the efficiency of the M2 trigger must be higher than 98% and that of M3 trigger must be higher than 97%. Moreover, the efficiency of M3 trigger for events containing more than 3 charged tracks (as the type of events analyzed in this work) is even higher. Therefore, one can conclude that the possible correction factor due to the relative efficiency of M2 and M3 triggers is less than 2%. This factor is added to the systematic errors discussed in chapter 8.

7.4.1 Trigger efficiency of TOF/TOFino scintillators

The TOF and TOFino detectors of HADES are made of plastic scintillators which produce a signal whenever a charged particle deposits enough energy in the scintillating rods to overcome the threshold.

Figure 7.4 shows a typical spectrum of the measurement of an **A**nalog to **D**igital **C**onverter (ADC) connected to one of the TOFino rods. The spectrum starts at ADC value of 70. Lower values are rejected by the threshold. The blue line represents a fit to the spectrum using a combined function (exponential+Landau). The exponential function is used to describe the noise at the beginning of the spectrum, while the Landau function describes the energy deposition by the particles hitting the rod. The red line represents the Landau distributed part of the spectrum.

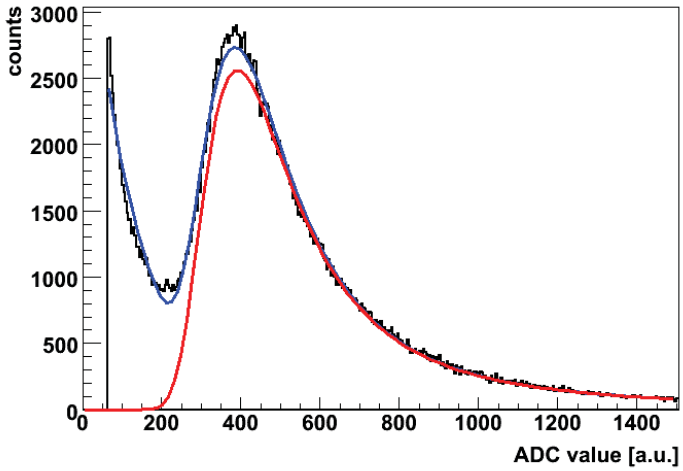

Figure 7.4: ADC spectrum for an ADC connected to one of the TOFino rods. Values less than 70 are rejected by the applied threshold. The blue line represents a fit by a model function using a combination of an exponential decay to account for the measurement noise and a Landau distribution to describe the energy deposition of real particles. The red line shows the Landau distributed part of the spectrum starting far above the threshold value of 70.

As can be seen from the figure the threshold of 70 is far below the starting point of the Landau distribution. This means that no real particle is rejected by the threshold since the signal of real particles is always higher than the threshold. Therefore, the assumption of a single particle efficiency of 99% is justified.

8

Yield determination and systematic errors

In chapter 3, the steps performed to obtain the pp missing mass spectrum in the reaction $pp \longrightarrow pp\pi^+\pi^-\pi^0$ were described. The spectrum contains two peaks corresponding to the reactions $pp \longrightarrow pp\eta$ and $pp \longrightarrow pp\omega$. In section 8.1, the steps performed to subtract the background below the two peaks and to determine the number of reconstructed η/ω mesons are presented. In section 8.2, a discussion of the systematic errors is given.

8.1 Background subtraction and yield determination

As discussed in chapter 5, the yield determination and background subtraction must be done in different bins of the $pp\pi^+\pi^-\pi^0$ phase space separately. The shape of the background and of the η/ω signals and the signal-to-background ratio change significantly between different phase space bins.
Figure 8.1 shows examples of the pp missing mass spectrum in two different angular ranges of the missing mass ($\pi^+\pi^-\pi^0$) system (forward and backward directions). The shape of the η/ω signals, the shape of the background, as well as the signal-to-background ratios differ considerably between the two examples.

The background subtraction is done in several steps:

1. The shapes of the pp missing mass spectra resulting from the reactions:

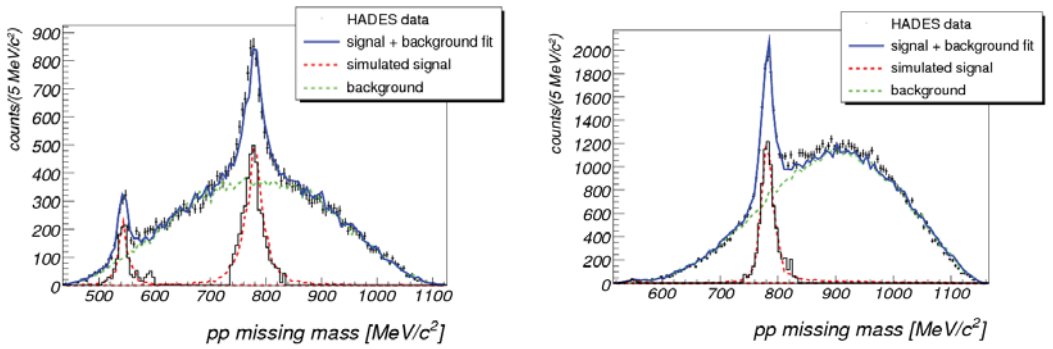

(a) (b)

Figure 8.1: pp missing mass spectrum in two $cos\theta_{cm}^{mm}$ intervals. (a) in backward direction ($-1 < cos\theta_{cm}^{mm} < -0.8$). (b) in forward direction ($0.8 < cos\theta_{cm}^{mm} < 1$). The shape of the η/ω signals, the shape of the background, as well as the signal-to-background ratios differ considerably in the two examples.

$pp \longrightarrow pp\eta \longrightarrow pp\pi^+\pi^-\pi^0$, $pp \longrightarrow pp\omega \longrightarrow pp\pi^+\pi^-\pi^0$, and $pp \longrightarrow pp\pi^+\pi^-\pi^0$ (direct) are determined in all phase space bins using events generated with PLUTO which are subjected to the detector filter and the standard reconstruction chain (see section 5.1).

2. The pp missing mass spectra in real data are determined in all phase space bins.

3. For each phase space bin, the following steps are performed:

   (a) The function $f_1(pp_{miss})$ given by the yield of the $pp \longrightarrow pp\pi^+\pi^-\pi^0$ (direct) missing mass spectrum simulated in step 1, is scaled in order to fit the pp missing mass spectrum of real data in the ranges $pp_{miss} < 500\ MeV/c^2$ and $pp_{miss} > 830\ MeV/c^2$. Both ranges exclude the region of the η/ω signals.

   (b) $f_1(pp_{miss})$ is not always enough to describe the whole background in the pp missing mass spectrum of real data. Therefore, an additional function f_2 is used to fit the difference between f_1 and the background in the real spectrum in the ranges of $pp_{miss} < 500\ MeV/c^2$ and $pp_{miss} > 830\ MeV/c^2$. f_2 is a polynomial of fourth order. The sum of f_1 and f_2 is the combined background function f_3.

(c) With the parameters of f_3 kept fixed, the functions f_η and f_ω given by the yield of the $pp \longrightarrow pp\eta$ and $pp \longrightarrow pp\omega$ missing mass spectra simulated in step 1 are scaled to fit the spectrum in the region of the η and ω peaks respectively.

(d) After step 3c, the parameters of the functions f_3, f_η, and f_ω are roughly known. As a last step, the whole range of the pp missing mass spectrum is fitted using the combined function $f_{tot} = f_3 + f_\eta + f_\omega$. The functions f_η and f_ω, f_3, and f_{tot} are given by the red, green, and blue lines in figure 8.1, respectively.

(e) The yield of the η/ω signal is obtained either by integrating the yield of the pp missing mass spectrum above f_3 (black lines figure 8.1), or by integrating the scaled functions f_η and f_ω respectively.

8.2 Systematic errors

In section 8.1, the steps performed to obtain the data yield in various phase space bins were described. The systematic errors of the determined yields are discussed in this section. There are four main sources of systematic errors.

1. The π^0 missing mass cut.
2. The kinematic fit (p-value cut).
3. The background subtraction procedure.
4. The normalization to the elastic cross section.

In the following subsections, the first three sources are discussed. The contribution to the systematic error by the fourth item is independent of this analysis and may be obtained from the original measurement of the elastic cross section [K$^+$71].

8.2.1 π^0 missing mass cut

Figure 8.2 shows the distribution of the four particles missing mass in events with two protons, one positive pion, and one negative pion. A peak at the square of the π^0 mass is visible on top of a huge background (due to the reaction $pp \longrightarrow pp\pi^+\pi^-$).

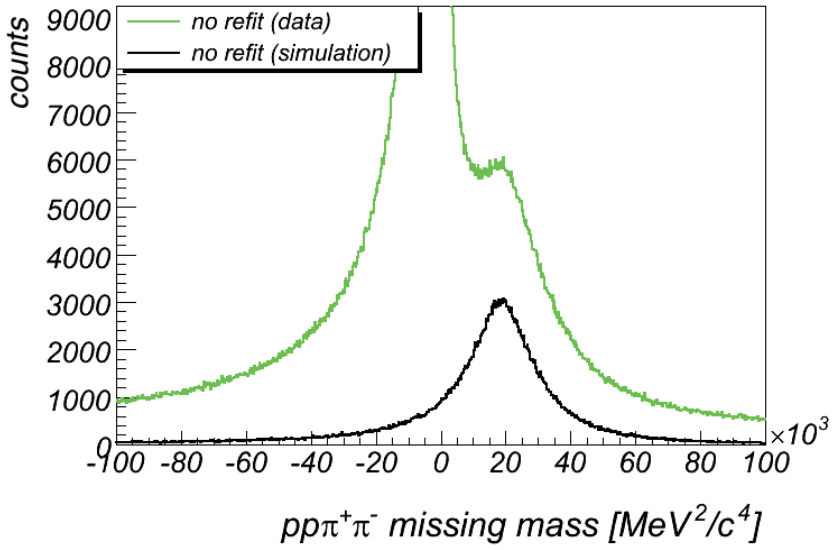

Figure 8.2: The $pp\pi^+\pi^-$ missing mass distribution in real data (green) and in simulations (black). A peak at the square of the π^0 mass is visible in the real distribution on top of a huge background.

The black curve in the same figure represents the $pp\pi^+\pi^-$ missing mass distribution in simulations of the reaction $pp \longrightarrow pp\pi^+\pi^-\pi^0$.

In order to define the limits of a π^0 selection cut, the results of the kinematic fit are used. Figure 8.3 shows the distribution of the $pp\pi^+\pi^-$ missing mass in events accepted by the kinematic fit and having a p-value higher than 20% for both real and simulated events.

As indicated by the black lines in the plots, the main part of the distributions follows a Gaussian function. The mean values of both distributions are similar, while their widths are different (almost 18% less in the case of the simulation). The plots show also longer tails than given by the Gaussian fit. Particularly, the distribution in the case of real data has a significant tail on the left side of the peak. This is obviously due to the huge background visible in figure 8.2 which is peaked at zero.

The low and high values of the π^0 missing mass cut are defined in both cases as $\mu - 1.65\sigma$ and $\mu + 1.65\sigma$ respectively, where μ is the mean value of the Gaussian fit. To estimate the systematic error due to the π^0 cut, let A be the ratio of the area below the Gaussian fit of the $pp\pi^+\pi^-$ missing mass distribution in real data to the area of the experimental distribution. And let B be the same ratio in the case of

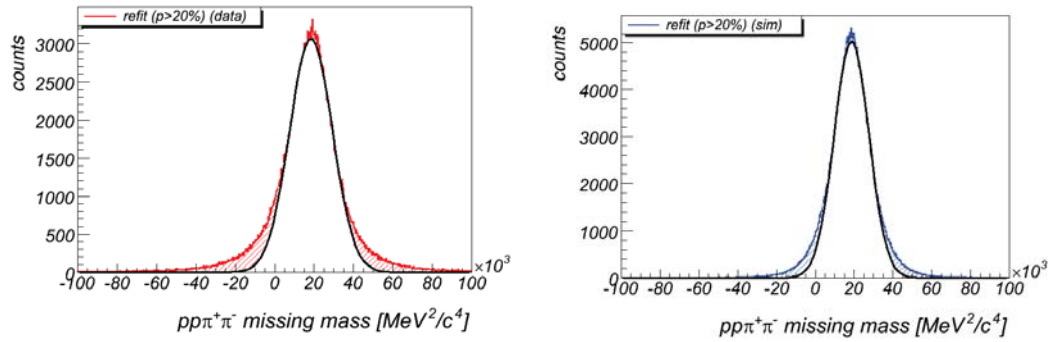

(a) (b)

Figure 8.3: The $pp\pi^+\pi^-$ missing mass distribution for events accepted by the kinematic fit and having a p-value higher than 20%: a) Real data. b) Simulation. The black lines represent a Gaussian fit to the spectra. Both spectra show tails on both sides of the peak. The tail on the left side of the peak in the real data is bigger than that on the right side. This is due to the huge background visible in figure 8.2.

simulation. The systematic error -in percent- due to the π^0 cut is estimated to be:

$$Err_{\pi^0} = \frac{1}{2} \times \left(1 - \frac{A}{B}\right) \times 100 \approx \pm 3\%$$

8.2.2 The kinematic fit p-value cut

As discussed in chapter 4, the kinematic fit leads to a significant improvement of the experimental resolution. A cut is applied to the p-value returned by the fit in order to reject a large fraction of the background sitting at low p-values. Figure 8.4 shows a comparison of the pp missing mass distribution obtained using the π^0 missing mass cut only and using the kinematic fit in addition to the π^0 missing mass cut.

Based on figure 8.4, one can draw the following conclusions:

- While not significantly affecting the ω meson peak, the kinematic fit is essential to obtain a reliable estimation of the η meson yield (compare the black and red curves).

- The ω meson peak coincides with the maximum of the background distribution. Therefore the systematic error due to the background subtraction in the case of the ω peak is much larger than in the case of the η peak. Hence, to estimate the systematic error due to the p-value cut, the η peak is used.

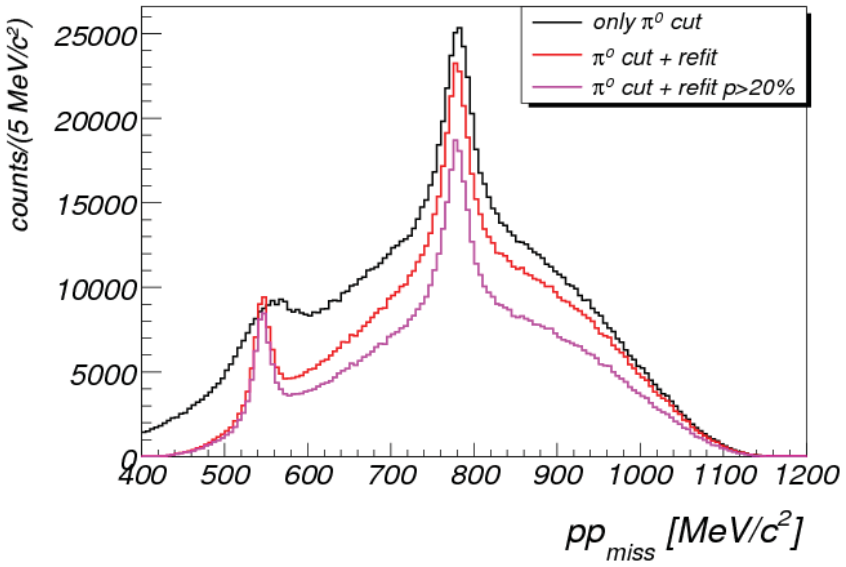

Figure 8.4: The pp missing mass distribution obtained using the π^0 missing mass cut (black), the π^0 cut and kinematic fit (red), and the π^0 cut and kinematic fit with p-value higher than 0.2 (magenta). The use of the kinematic fit leads to a significant improvement of the mass resolution of the η peak, while the p-value cut improves the signal to background ratio.

The p-value cut is set to 20%. Table 8.1 summarizes the number of reconstructed η mesons in real data and simulations using four different p-value cuts. Table 8.1

cut value	n^{η}_{rec} (sim)	n^{η}_{rec} (real)	n^{bg} (real)	S/B (real)	$\frac{real}{sim} \times 10^3$
$p \geq 0$	1926491	35224	66229	0.53	18.28
$p \geq 0.1$	1878175	33758	53036	0.64	17.97
$p \geq 0.2$	1799055	32384	48838	0.66	18.00
$p \geq 0.3$	1687455	30681	44404	0.69	18.18

Table 8.1: The number of reconstructed η mesons (n^{η}_{rec}) in real data and simulations at different p-value cuts. The last column shows the ratio of n^{η}_{rec} in real data to simulations. n^{bg} denotes the integral of the background below the η peak, while S/B is the signal to background ratio.

shows that the ratio of the number of η mesons reconstructed in real data to the number reconstructed in the simulation changes by about 1% when varying this p-value cut. If no cut on the p-value is applied ($p \geq 0$), the ratio changes only by 1.5% to that with a cut applied at 20%. Therefore, the systematic error due to the

p-value cut is estimated to be 0.75% which can be neglected.

8.2.3 Background subtraction

The steps of background subtraction were described in section 8.1. To estimate the systematic error due to the background subtraction, the degree of the polynomial function f_2 used in addition to the function f_1 is varied and the change in the deduced yield is taken as the systematic error. As also discussed in section 8.1, the shape of the background and the signal to background ratio vary considerably between different phase space bins. Accordingly, the systematic error due to the background subtraction is determined in each phase space bin and for each of the η and ω mesons separately. It varies considerably between the various phase space bins and is on average about 5%. The systematic error is added quadratically to the statistical error for differential cross sections so that it can be taken into account when –for example– fitting the angular distribution.

9

Results

In this chapter, the results of analyzing proton-proton interaction data collected by HADES at 3.5 GeV beam kinetic energy are presented. In particular, distributions describing the exclusive production of η and ω mesons are shown. The η and ω mesons were reconstructed in their $\pi^+\pi^-\pi^0$ decay channel. The kinematic fit discussed in chapter 4 was applied on events selected using the π^0 missing mass cut presented in chapter 3. A p-value cut was applied at 20%. No PID algorithm was applied. For a discussion of systematic errors see chapter 8.

9.1 η meson

9.1.1 Dalitz plot

Figure 9.1 shows the acceptance corrected $pp\eta$ Dalitz plot as a function of $M^2_{p_2\eta}$ versus $M^2_{p_1\eta}$ and as a function of M^2_{pp} versus $M^2_{p\eta}$. The plots show an enhancement of the yield close to the $p\eta$ threshold which is due to the contribution of the $N(1535)$ resonance to the production of η. Figure 9.2 shows the number of reconstructed η mesons as a function of $M^2_{p\eta}$. Again, the signal of the production via $N(1535)$ is also visible. Two simulations of this distribution were done to estimate the amount $N(1535)$ contribution to the η production:

1. Simulation of the distribution in case of η production only via $N(1535)$.

2. Simulation of the distribution in case of pure phase space production.

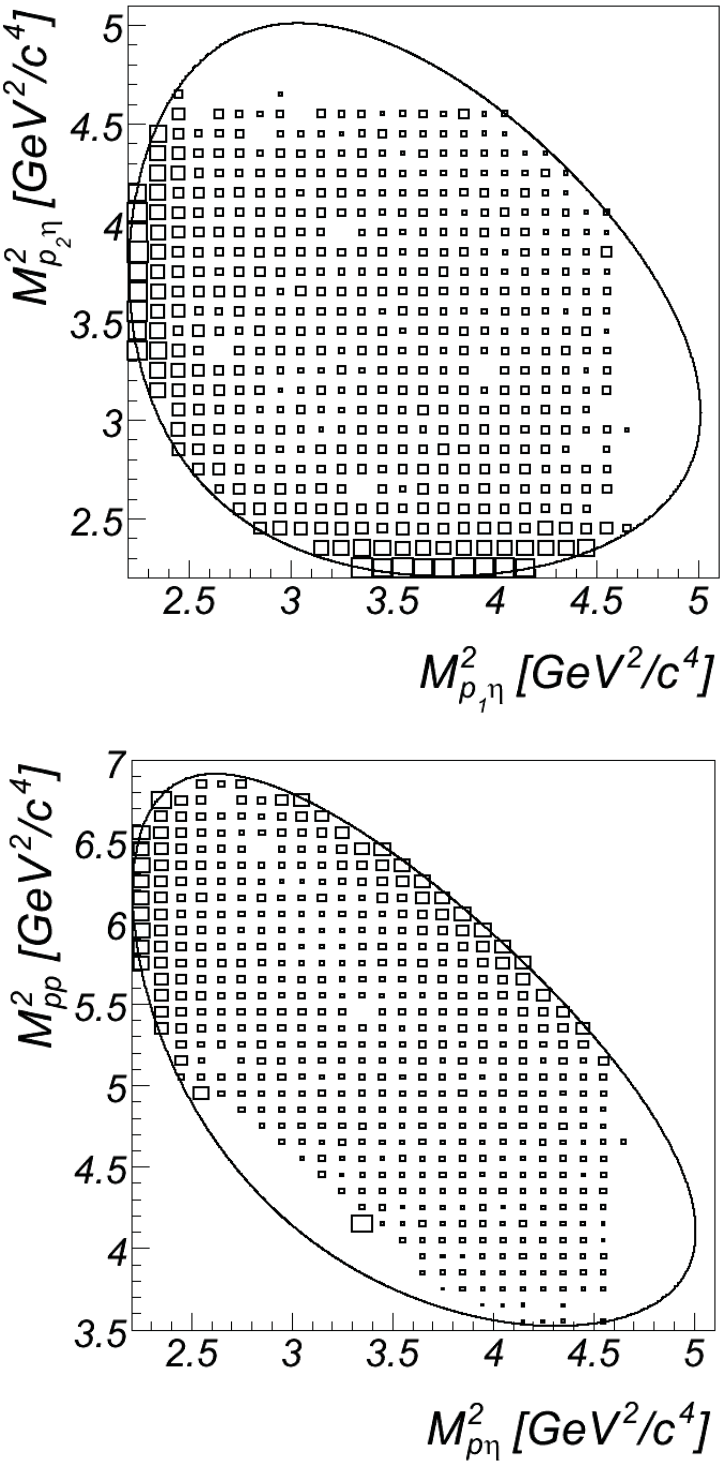

Figure 9.1: $pp\eta$ Dalitz plots. The plots are corrected for acceptance in the regions of non-vanishing acceptance. Bins outside the kinematically allowed phase space (solid curves) and those where the systematic error is larger than the bin content were removed from the plot. The yield enhancement at the $p\eta$ threshold hints to the production via the $N(1535)$ resonance.

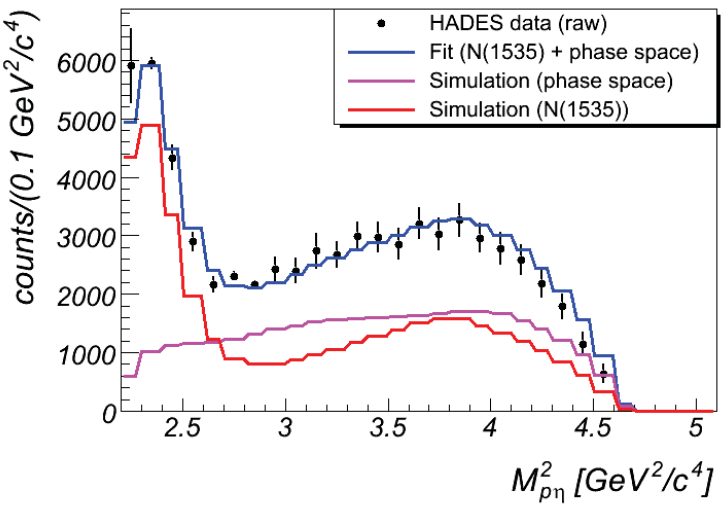

Figure 9.2: Number of reconstructed η mesons as a function of $M^2_{p\eta}$. Each event is included twice with $M^2_{p\eta}$ calculated using the combination of η with each of the two protons. The error bars are dominated by systematic errors due to the background subtraction. The statistical errors are negligible. A clear signal of the $N(1535)$ resonance is observed. The red line indicate the distribution as given by the simulation if η is produced merely via $N(1535)$. The magenta line shows the simulated distribution in case of pure phase space production. The simulated distributions were scaled such that their sum (blue line) fits the measured data.

By scaling both simulated distributions to fit the measured spectrum, the cross section for resonant production was estimated to be 47% of the total cross section.

The resonance contribution to the production is also reflected in the momentum distributions of the η meson and the protons. Figure 9.3 shows a comparison of the number of reconstructed η mesons as a function of P^{η}_{CM} and P^{p}_{pp} in real data and in simulations of pure phase space production (P^{η}_{CM} is the momentum of the η meson in the reaction center of mass system, and P^{p}_{pp} is the momentum of the protons in the rest frame of the two protons.).
Including the production of η via $N(1535)$ in the simulation with the ratio obtained from fitting the data in figure 9.2, the momentum distributions in real data and simulation agree. This is shown in figure 9.4.

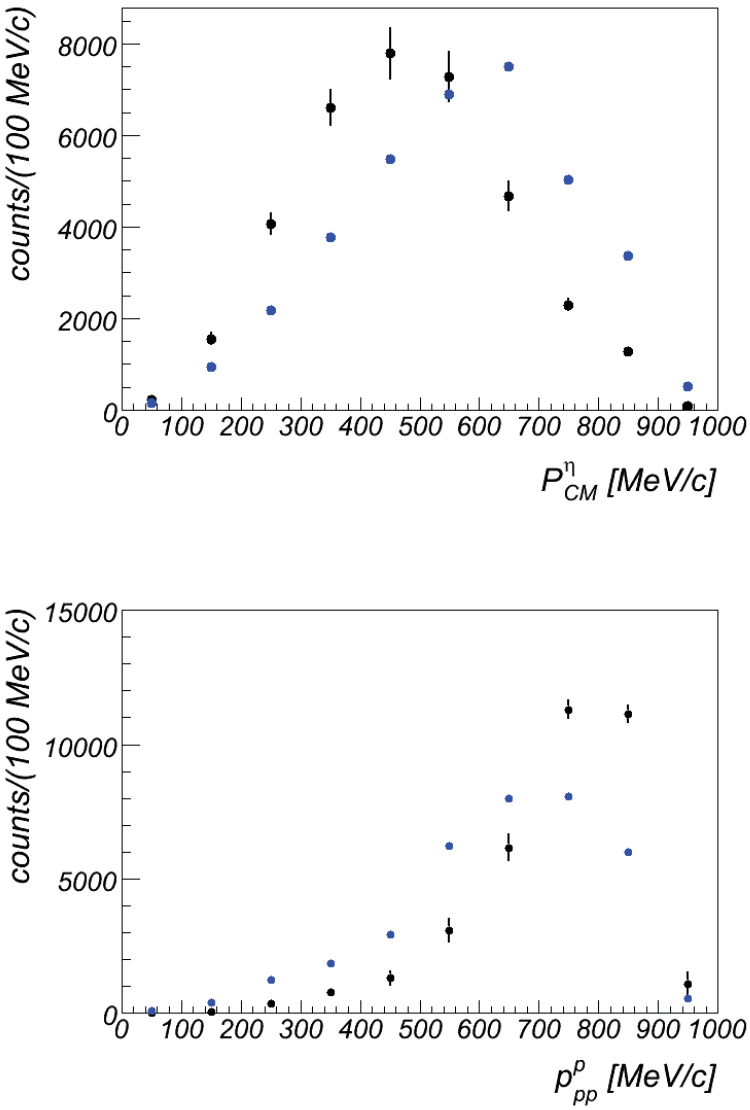

Figure 9.3: Number of reconstructed η mesons as a function of momentum for real data (black points) and for pure phase space simulations (blue points). The simulated distributions differ from the measured ones since the production of η via $N(1535)$ is not taken into account.

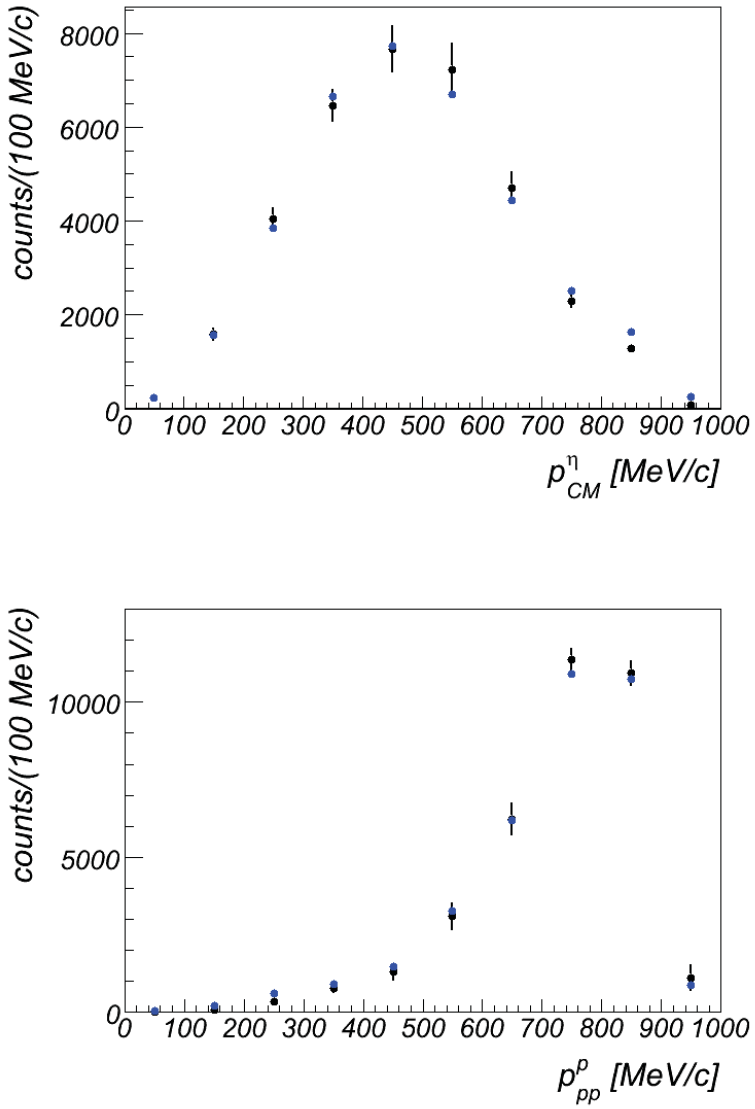

Figure 9.4: Number of reconstructed η mesons as a function of momentum for real data (black points) and for simulations including 47% resonant production (blue points). The simulated distributions agree with the measured ones.

9.1.2 Angular distribution

Figure 9.5 shows the distribution of the center of mass angle of the η meson in two cases:

a) When the square of the invariant mass of η and one of the two protons ($M^2_{p\eta}$) is less than 2.8 GeV^2/c^4. Such selection ensures that most of the η mesons are coming via $N(1535)$.

b) When the square of the invariant mass of η and each of the two protons ($M^2_{p\eta}$) is higher than 2.8 GeV^2/c^4. Such selection ensures that all of the η mesons are coming from non-resonant production.

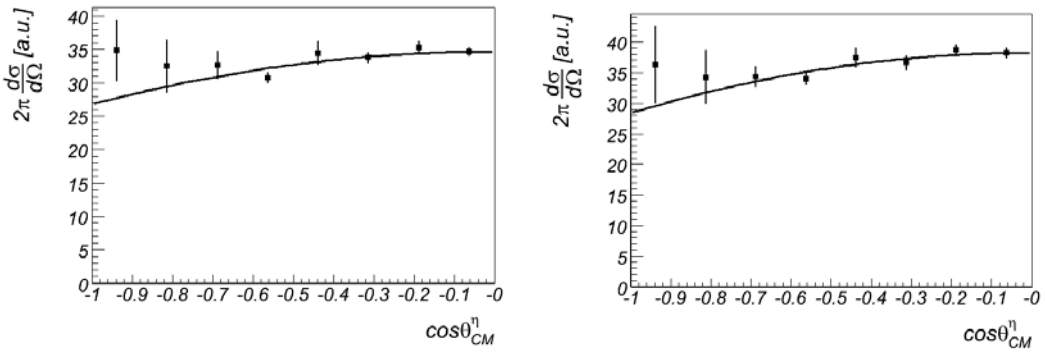

Figure 9.5: The angular distribution of η in the center of mass system. a) for resonant production (selected by asking for one of the protons to fulfill $M^2_{p\eta} \leq 2.8\ GeV^2/c^4$). b) for non resonant production (selected by asking for both of the protons to fulfill $M^2_{p\eta} \geq 2.8\ GeV^2/c^4$). Both plots were fitted using the first two even Legendre polynomials (black curves).

In both pictures, the distribution in the backward hemisphere is plotted since the forward hemisphere is not fully covered. In addition, the data was selected in the ranges of $|cos\theta^p_{pp}| \leq\ 0.4$ and $M^2_{pp} \geq 5.5\ GeV^2/c^4$ which contain almost no regions of vanishing acceptance in the backward hemisphere.
Figure 9.6 shows the integrated distribution of $cos\theta^{\eta}_{CM}$ over the whole range of invariant masses $M^2_{p\eta}$. The three angular distributions in figures 9.5 and 9.6 are slightly anisotropic. The distributions were fitted using the first two even Legendre polynomials. The results of the fits are as follows:

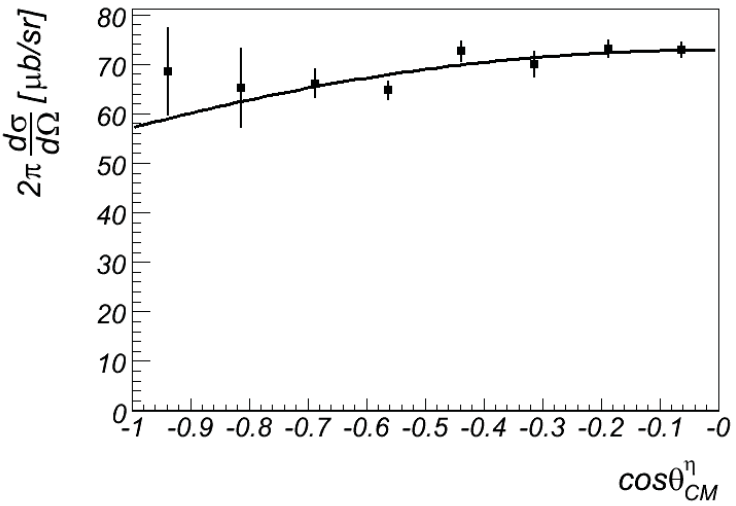

Figure 9.6: The integrated angular distribution of η in the center of mass system. The black curve shows a fit to the distribution using the first two even Legendre polynomials.

- $2\pi \ \frac{d\sigma}{d\Omega} = (32.04 \pm 0.62) \times (P_0 - (0.164 \pm 0.052) \ P_2)$ [a.u.], for the angular distribution in the resonant region.

- $2\pi \ \frac{d\sigma}{d\Omega} = (34.95 \pm 0.67) \times (P_0 - (0.188 \pm 0.054) \ P_2)$ [a.u.], for the angular distribution in the non resonant region.

- $2\pi \ \frac{d\sigma}{d\Omega} = (67.64 \pm 1.2) \times (P_0 - (0.155 \pm 0.05) \ P_2)$ [μb/sr], for the integrated angular distribution.

P_0 is a constant function, so that it gives the height of the distribution. P_2 is a second degree polynomial function, so that it defines the curvature/anisotropy of the distribution. The three fit functions mentioned above are apart from the constant value the same within errors.

About 35 000 η mesons were reconstructed. The total cross section for η production was calculated to be $136.9 \pm 0.9(\text{stat}) \pm 10.1(\text{sys})$ [μb] where stat indicates statistical error and sys indicates systematic error. The result was obtained by integrating all data. Integrating fit result of the angular distribution yields 135.28 [μb] which is within two standard deviations from the previous result.

9.2 ω meson

9.2.1 Dalitz plot

Figure 9.7 shows the acceptance corrected $pp\omega$ Dalitz plot as a function of $M^2_{p_2\omega}$ versus $M^2_{p_1\omega}$ and as a function of M^2_{pp} versus $M^2_{p\omega}$. Although the distributions exhibit deviations from phase space production, they show no significant signal of a resonance, which is also true for figure 9.8 where the number of reconstructed ω mesons as a function of $M^2_{p\omega}$ is shown for real data and for simulations based on phase space production.

Deviations of the measured data with respect to simulations based on phase space distributions should manifest in the momentum distributions. In figure 9.9 we compare the number of reconstructed ω mesons as a function of P^{ω}_{CM} and P^{p}_{pp} in real data and in simulations of pure phase space production. The deviations between the two are an indication of production mechanisms beyond simple phase space.

Figure 9.10 shows the ratio of the two distributions of figure 9.8. The plot shows a slight enhancement at the $p\omega$ threshold which might be a hint to a resonance contribution.

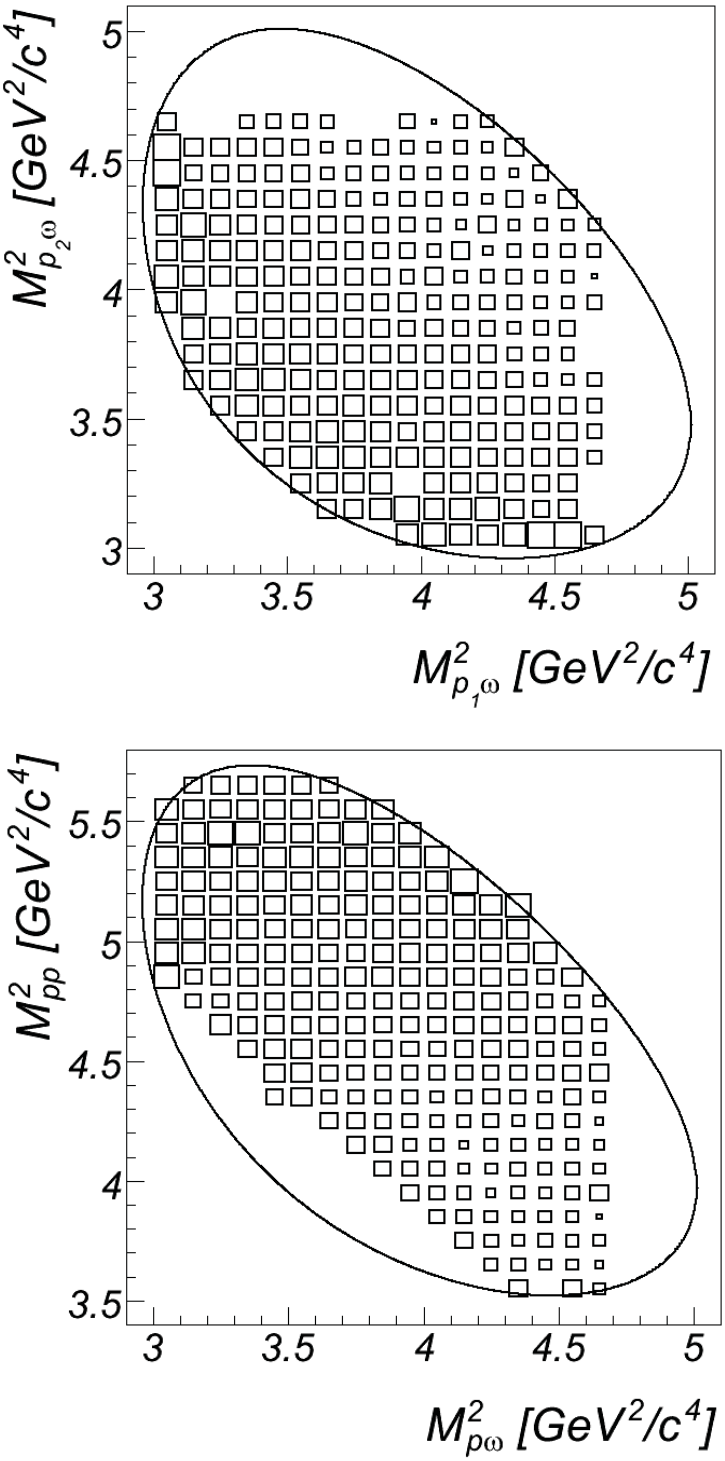

Figure 9.7: $pp\omega$ Dalitz plots. The plots are corrected for acceptance in the regions of non-vanishing acceptance. Bins outside the kinematically allowed phase space (solid curve) and those in which the error is larger than the respective bin content were removed. The distributions exhibit deviations from phase space production. However, they show no significant signal of a resonance.

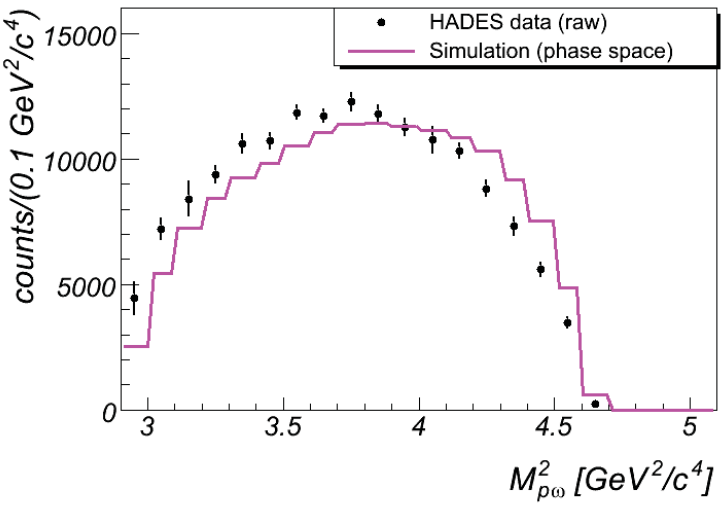

Figure 9.8: Number of reconstructed ω mesons as a function of $M^2_{p\omega}$. Each event is included twice with $M^2_{p\omega}$ calculated using the combination of ω with each of the two protons. The error bars are dominated by systematic errors due to the background subtraction. The statistical errors are negligible. The magenta line shows the distribution as given by simulations based on pure phase space production. The simulated distribution deviates from the measured one indicating a production mechanism beyond simple phase space.

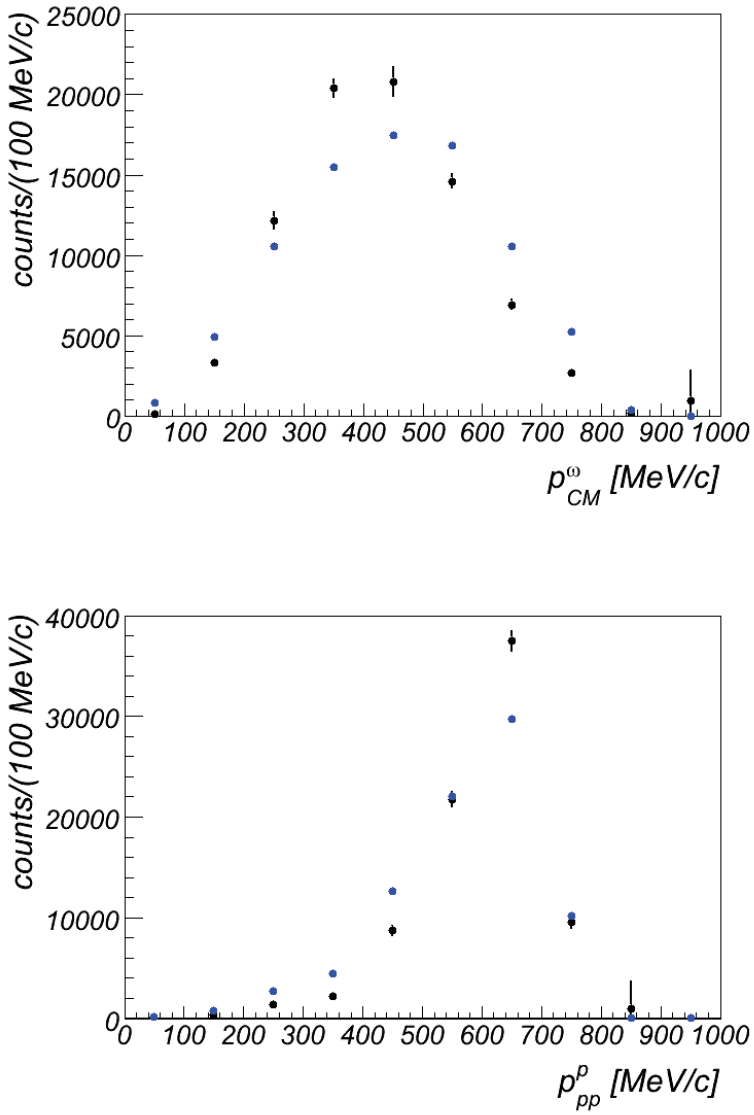

Figure 9.9: Number of reconstructed ω mesons as a function of momentum for real data (black points) and for pure phase space simulations (blue points). The simulated distributions differ from the measured ones indicating a different production mechanism.

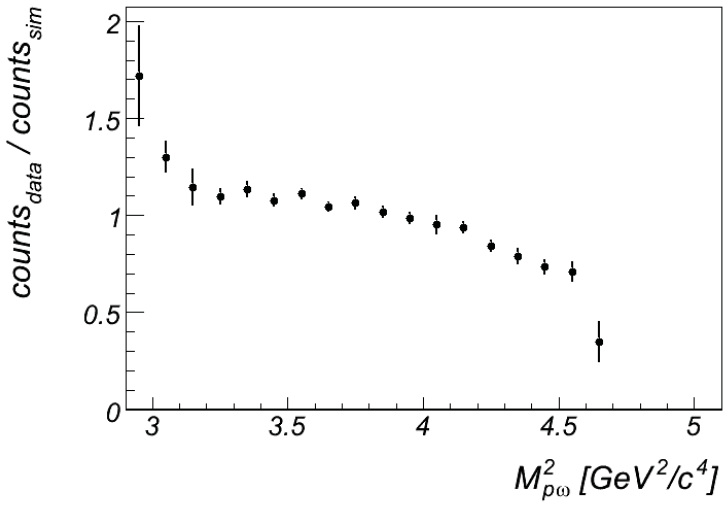

Figure 9.10: Ratio of the number of reconstructed ω mesons as a function of $M^2_{p\omega}$ in real data to the number reconstructed in simulations based on phase space production (arbitrarily scaled). The distribution shows a slight enhancement at the $p\omega$ threshold.

9.2.2 Angular distribution

In contrast to the case of η, the ω meson is well reconstructed in the forward hemisphere. The data were selected within the range $|cos\theta^{p}_{pp}| \leq 0.6$ and $M^2_{pp} \geq 4\ GeV^2/c^4$ which contain almost no region of vanishing acceptance in the forward hemisphere. Figure 9.11 shows the distribution of the center of mass angle of the ω meson in such range. The figure exhibits a small anisotropy, the shape of which suggests the

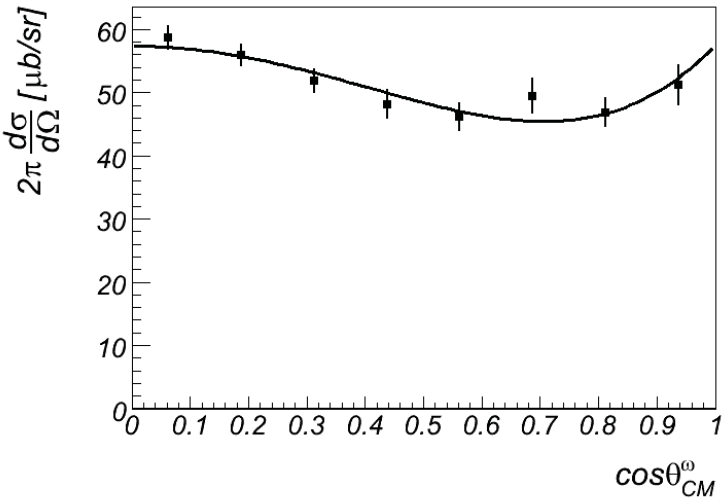

Figure 9.11: The angular distribution of ω in the center of mass system. The black curve shows a fit to the data using the first three even Legendre polynomials. The parameters of the fit are given in the text.

use of the first three even Legendre polynomials for a fit. The result of the fit is:

$$2\pi \ \frac{d\sigma}{d\Omega} = (51.0 \pm 0.84) \times (P_0 - (0.088 \pm 0.042)\ P_2 + (0.21 \pm 0.057) P_4)\ \ [\mu\text{b/sr}]$$

About 80 000 ω mesons were reconstructed. The total cross section for ω production was calculated to be 106.5 ± 0.9 (stat) $\pm$ 7.9 (sys) [μb] where stat indicates statistical error and sys indicates systematic error. The result was obtained by integrating all data. Integrating the angular distribution fit result yields 102.0 [μb] for the total production cross section.

9.3 Summary and conclusion

The production of ω via resonances was observed in photoproduction measurements. While Barth *et. al.* claim the production to take place via $N(1710)$ [B$^+$03], Klein *et. al.* claim it to take place via the $N(1720)$ [K$^+$08]. The width of both resonances is also not precisely settled. The particle data group [N$^+$10] gives 50-250 MeV/c^2 as the width of $N(1710)$ and 100-300 MeV/c^2 as the width of $N(1720)$. The COSY-TOF collaboration[AB$^+$10] measured the reaction $pp \longrightarrow pp\omega$ at three different energies and concluded that they found no obvious indication of resonant ω-production via N^* resonances. However, they did not do Dalitz studies.
The HADES data show no significant signal of a resonance. However, the contribution of a broad resonance at or below threshold to the production of ω is not excluded by the data.

The angular distribution of ω mesons was measured by the DISTO collaboration [B$^+$01] at 2.85 GeV beam kinetic energy. The distribution was fitted using the first three even Legendre polynomials. The result:
$\frac{d\sigma}{d\Omega} = (4.0 \pm 0.1)P_0 + (3.1 \pm 0.2)P_2 + (2.0 \pm 0.2)P_4$ [μb/sr]
is strongly anisotropic. The HADES measurement at 3.5 GeV beam kinetic energy is much less anisotropic. This hints to a strong energy dependence in this energy regime.

The production of η via $N(1535)$ has been also measured by the DISTO collaboration at three different beam energies (2.15, 2.5, and 2.85 GeV) [B$^+$04]. The contribution of $N(1535)$ at beam energy of 2.85 GeV was measured to be about 43%. The DISTO measurements of the η angular distribution also point to low anisotropy at the beam energies of 2.5 and 2.85 GeV.

The measurement of angular and Dalitz distributions of meson production in nucleon-nucleon collisions provide valuable information about the magnitude of different contributions to the production process. It is however worth mentioning that most of the models dealing with the nucleon nucleon interaction are valid near to the production threshold. It is not always straight forward to extend them to energies far away from threshold.

10

Zusammenfassung

Im Rahmen dieser Arbeit wurden differentielle und integrale Produktionsquerschnitte von ω und η Mesonen in Proton-Proton Reaktionen bei 3.5 GeV Strahlenergie mit dem High Acceptance DiElektron Spectrometer (HADES) am Schwerionensynchrotron des Helmholtzzentrum für Schwerionenforschung in Darmstadt gemessen. Etwa 80000 ω Mesonen und 35000 η Mesonen wurden rekonstruiert. Diese Statistik erlaubt die Untersuchung von Winkelverteilungen und Dalitz-Diagrammen.

10.1 Motivation

Die Untersuchung der Mesonenproduktion in Proton-Proton Kollisionen bei wenigen hunderten MeV über der Produktionsschwelle liefert wichtige Informationen über die Wechselwirkung zwischen Nukleonen. Theoretische Modelle beschreiben die Wechselwirkung zwischen Nukleonen über den Austausch von Mesonen. In diesen Modellen tragen verschiedene Wechselwirkungsmechanismen zur Produktion von Mesonen in Nukleon-Nukleon Kollisionen bei. Messungen von differentiellen und integralen Produktionsquerschnitten liefern somit wichtige Informationen, mit deren Hilfe der Beitrag der einzelnen Wechselwirkungsmechanismen ermittelt werden kann. Darüber hinaus liefern solche Studien essentielle Ausgangsdaten für Transportmodelle, die z.B. die Elektronenpaarproduktion in Pion- und Proton-induzierten Reaktionen sowie in Schwerionenkollisionen beschreiben.

10.2 Datenanalyse

ω und η Mesonen wurden im Zerfallskanal ($\pi^+\pi^-\pi^0$) in der exklusiven Reaktion $pp \longrightarrow pp\pi^+\pi^-\pi^0$ rekonstruiert.

Ausgewertet wurden Ereignisse mit drei positiv geladenen Spuren und einer negativ geladenen Spur. In jedem Ereignis wurden drei Hypothesen für die Massen der positiv geladenen Teilchen berücksichtigt (siehe Tabelle 3.1). Ereignisse, in denen ein neutrales Pion zusätzlich zu den zwei Protonen und zwei geladenen Pionen produziert wurde, werden mit Hilfe einer Bedingung auf die $pp\pi^+\pi^-$-fehlende-Masse selektiert. Durch die "π^0-fehlende-Masse"Bedingung werden die meisten nichtzutreffenden Massenhypothesen aussortiert (siehe Tabelle 3.3). Abbildung 10.1 zeigt den Energieverlust gegen den gemessenen Impuls für Spuren, die nach der "π^0 fehlende Masse"Bedingung als: (a) positive Pionen und (b) Protonen identifiziert wurden. Die Fehlidentifikationsquote liegt bei etwa 3% (siehe Abschnitt 3.3.3).

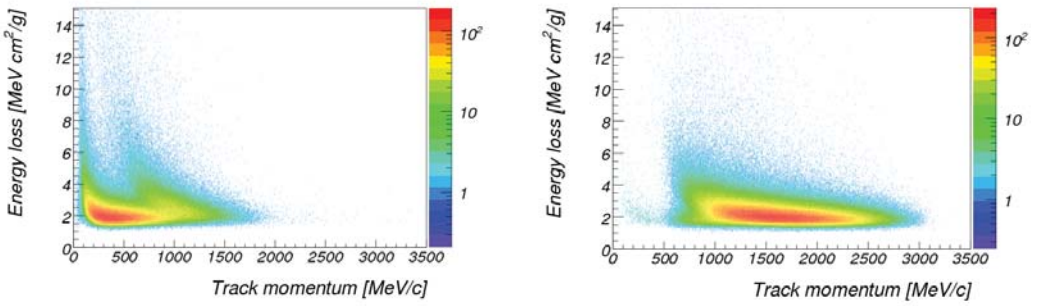

(a) (b)

Abbildung 10.1: Der Energieverlust aufgetragen gegen den gemessenen Impuls für Spuren die mit dem "π^0 fehlende MasseSSchnitt als: (a) positive Pionen und (b) Protonen identifiziert wurden.

Um die Massenauflösung zu verbessern und um Ereignisse, in denen ein π^0 produziert wurde, zu identifizieren, wurde ein kinematischer Fit angewendet. Insbesondere im Bereich des η Signals führt der kinematische Fit zu einer deutlichen Verbesserung der Massenauflösung und des Signal-zu-Untergrund-Verhältnisses, wie in Abbildung 10.2 zu sehen ist.

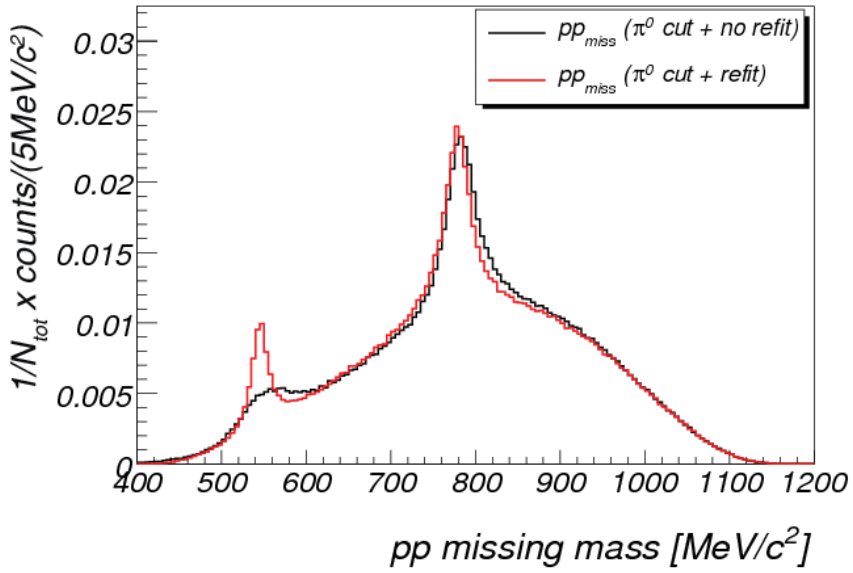

Abbildung 10.2: Das Proton-Proton fehlende-Masse-Spektrum in der Reaktion $pp \longrightarrow pp +$ missing mass: mittels der π^0-fehlende-Masse Bedingung (schwarz) und mittels des kinematischen Fit zusätzlich zu der π^0 Bedingung (rot). Der kinematische Fit führt zu einer deutlichen Verbesserung der Massenauflösung und des Signal-zu-Untergrund-Verhältnisses im Bereich des η Signals. Beide Kurven wurden auf eins normiert.

10.3 Akzeptanzkorrektur und Normierung

Die Korrektur der gemessenen Daten auf Effekte der Spektrometereffizienz und Akzeptanz wurde in vier Dimensionen durchgeführt. Hierfür wurden der Produktionswinkel im Reaktionsschwerpunktsystem ($\theta^{\eta/\omega}_{CM}$ Abbildung 10.3(a)), der Winkel der Protonen in deren gemeinsamen Ruhesystem (θ^{p}_{pp} Abbildung 10.3(b)), sowie zwei invariant Massen (die invariante Masse von dem produzierten Meson und jeweils eines der beiden Protonen ($M^2_{p_{1/2}} + \eta/\omega$) oder alternativ die invariante Masse der beiden Protonen (M^2_{p+p})) ausgewählt.

Die Akzeptanz des Spektrometers für unterschiedliche Winkelverteilungen wurde mit Hilfe von umfassenden Simulationen systematisch untersucht. Die gemessenen Daten wurden auf den Querschnitt von der Proton-Proton elastischer Streuung bei dem gleichen Strahlimpuls normiert. Systematische Fehler aufgrund der verschiedenen Algorithmen der Datenanalyse und des Untergrundabzugs wurden bestimmt.

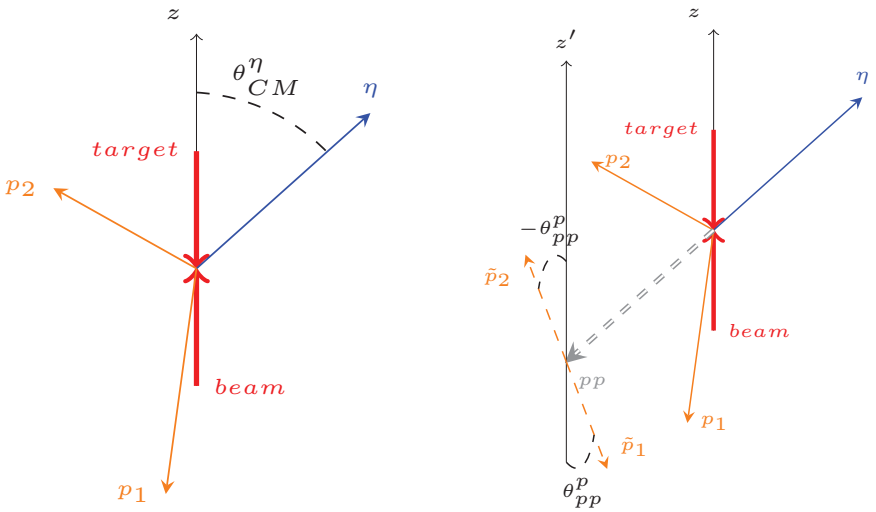

(a) (b)

Abbildung 10.3: Die gewählten Winkel für die Akzeptanzkorrektur. (a) Der Produktionswinkel im Schwerpunktsystem θ^{η}_{CM}. (b) Der Protonenwinkel in dem Ruhesystem der beiden Protonen θ^{p}_{pp}. Hier dient das η Meson als Beispiel. Für das ω Meson sind die Winkel gleich definiert.

10.4 Resultate

Insgesamt wurden ca. 35 000 η und ca. 80 000 ω Mesonen rekonstruiert. Der totale Wirkungsquerschnitt für die Produktion von ω Mesonen in der exklusiven Reaktion $pp \longrightarrow pp\omega$ beträgt $106.5 \pm 0.9\ (stat) \pm 7.9\ (sys)\ [\mu b]$. Für die η Mesonen beträgt der totale Produktionswirkungsquerschnitt $136.9 \pm 0.9\ (stat) \pm 10.1\ (sys)\ [\mu b]$ in der exklusiven Reaktion $pp \longrightarrow pp\eta$.

Die Winkelverteilungen von ω und η Mesonen im Schwerpunktsystem der Reaktion wurden gemessen. Beide Verteilungen sind leicht anisotrop (siehe Abbildung 10.4). Die Winkelverteilung von Protonen wurde in den beiden Reaktionen $pp \longrightarrow pp\eta$ und $pp \longrightarrow pp\omega$ in dem Bereich $0 \leq cos\theta^{p}_{pp} \leq 0.6$ gemessen. In diesem Bereich ist die Winkelverteilung der Protonen isotrop (siehe Appendix B).

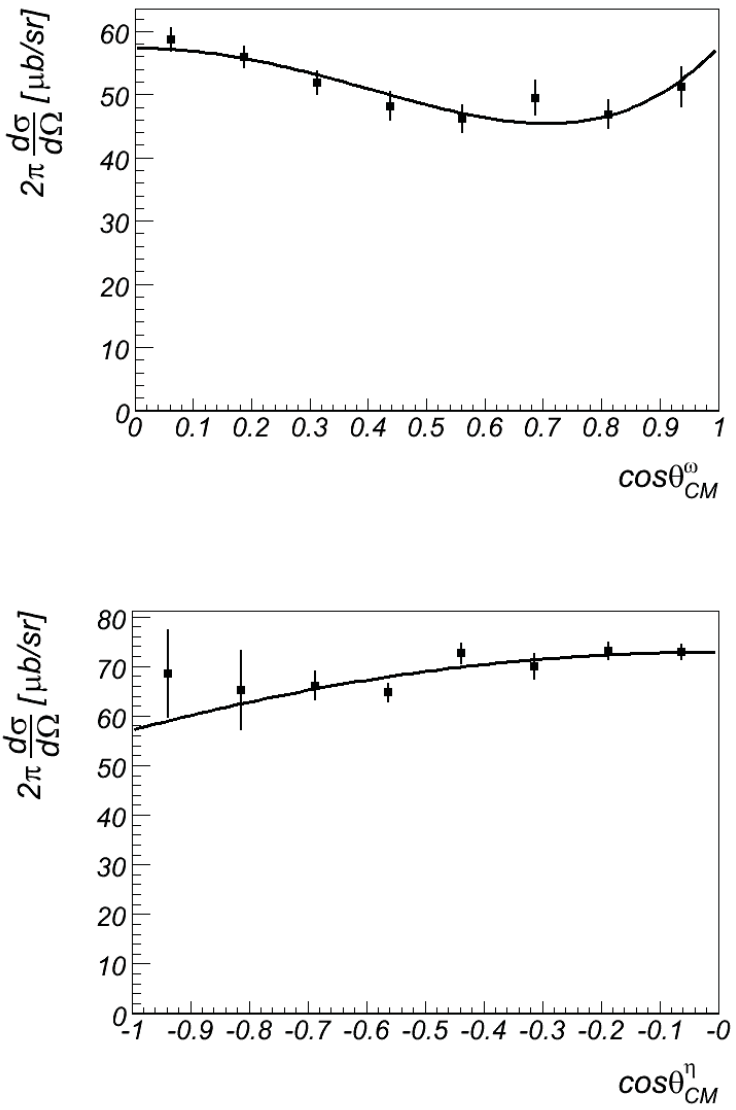

Abbildung 10.4: (a) Die Verteilung von ω Mesonen als Funktion von deren Winkel im Schwerpunktsystem der Reaktion $pp \longrightarrow pp\omega$. Die Ereignisse wurden in den Bereichen $|cos\theta^{p}_{pp}| \leq 0.6$ und $M^2_{pp} \geq 4\ GeV^2/c^4$ selektiert. Die Verteilung wurde mit den ersten drei geraden Legendre Polynomen gefittet.
(b) Die Verteilung von η Mesonen als Funktion von deren Winkel im Schwerpunktsystem von der Reaktion $pp \longrightarrow pp\eta$. Die Ereignisse wurden in den Bereichen $|cos\theta^{p}_{pp}| \leq 0.4$ und $M^2_{pp} \geq 5.5\ GeV^2/c^4$ selektiert. Die Verteilung wurde mit den ersten zwei geraden Legendre Polynomen gefittet.
Die Datenpunkte in beiden Diagrammen wurden auf Akzeptanz und Effizienz korrigiert. Die Fehlerbalken sind von systematischen Fehler aufgrund des Untergrundabzugs dominiert. Die statistischen Fehler sind vernachlässigbar.

Das ppω Dalitz-Diagramm (Abbildung 10.5(a)) zeigt einen Hinweis auf einen Produktionsmechanismus abweichend von der einfachen Phasenraumproduktion. Jedoch ist die Abweichung der gemessenen Verteilung von Phasenraumsimulationen nicht groß. Hingegen zeigt das $pp\eta$ Dalitz-Diagramm (Abbildung 10.5(b)) ein Signal der resonanten Produktion über die $N(1535)$ Resonanz. Etwa die Hälfte aller η Mesonen werden via die $N(1535)$ Resonanz produziert. Die Winkelverteilung von η Mesonen im Schwerpunktsystem ändert sich für resonante und nicht resonante Produktion nicht.

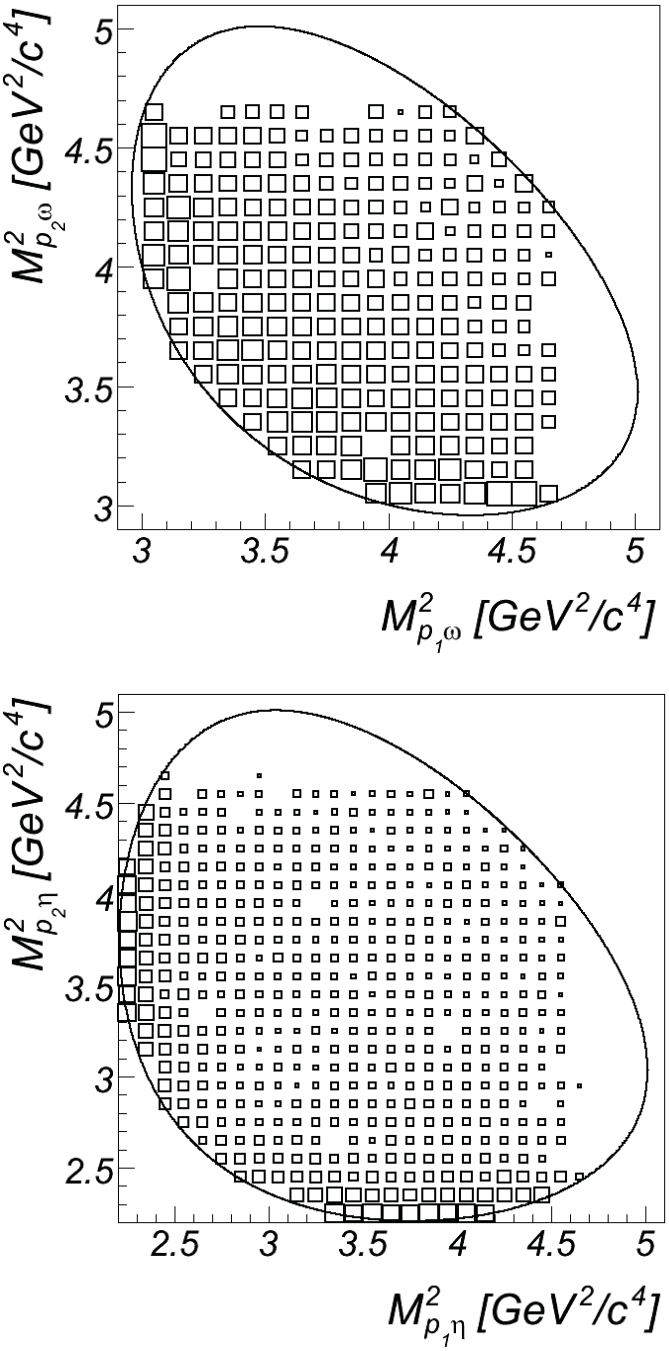

Abbildung 10.5: $pp\omega$ (a) und $pp\eta$ (b) Dalitz-Diagramme. Die Daten wurden im Bereich der Spektrometerakzeptanz auf Akzeptanz und Effizienz korrigiert. Phasenraumzellen ausserhalb der Phasenraumgrenze und solche, in denen der systematische Fehler größer ist als der Inhalt der Zelle wurden nicht dargestellt. Das $pp\omega$ Dalitz-Diagramm zeigt eine Abweichung von der einfachen Phasenraumproduktion, jedoch kein signifikantes Signal einer Resonanz. Das $pp\omega$ Dalitz-Diagramm weist ein Signal der resonanten Produktion an der $p\eta$ Schwelle auf. Dieses Signal wird mit der $N(1535)$ Resonanz identifiziert.

References

[A+95] Claude Amsler et al. eta decays into three pions. *Phys. Lett.*, B346:203–207, 1995. 61

[A+09] G. Agakishiev et al. The High-Acceptance Dielectron Spectrometer HADES. *Eur. Phys. J.*, A41:243–277, 2009. 6

[AB+10] M. Abdel-Bary et al. Systematic study of the pp → pp omega reaction. *Eur. Phys. J.*, A44:7–22, 2010. 108

[B99] M Böhmer. Das Auslesesystem für den Ringabbildenden Cherenkovdetektor im HADES Spektrometer. *Diplomarbeit. Physik-Department der Technischen Universität München, Institut E12*, 1999. 7

[B+01] F. Balestra et al. Phi and omega meson production in p p reactions at p(lab) = 3.67-GeV/c. *Phys. Rev.*, C63:024004, 2001. 108

[B+03] J. Barth et al. Low-energy of photoproduciton of omega-mesons. *Eur. Phys. J.*, A18:117–127, 2003. 108

[B+04] F. Balestra et al. Exclusive eta production in proton-proton reactions. *Phys. Rev.*, C69:064003, 2004. 108

[BCG] Rene Brun, Federico Carminati, and Simone Giani. GEANT Detector Description and Simulation Tool. CERN-W5013. 58

[BST61] J. Peter Berge, Frank T. Solmitz, and Horace D. Taft. Kinematical analysis of interaction vertices from bubble chamber data. *Review of Scientific Instruments*, 32(5):538–548, 1961. 41

[F+07] I. Frohlich et al. Pluto: A Monte Carlo Simulation Tool for Hadronic Physics. *PoS*, ACAT2007:076, 2007. 58

REFERENCES

[GAR] GARFIELD. Simulation of gaseous detectors. *http://garfield.web.cern.ch/garfield*. 16

[Gar98] C. Garabatos et al. Optimisation of low-mass drift chambers for HADES. *Nucl. Instrum. Meth.*, A 412:38–46, 1998. 11

[K+71] R. C. Kammerud et al. Large angle proton proton elastic scattering at intermediate momenta. *Phys. Rev.*, D4:1309–1324, 1971. 83, 89

[K+08] Frank Klein et al. Beam asymmetry in near threshold omega photoproduction off the proton. *Phys. Rev.*, D78:117101, 2008. 108

[Kri10] F. Krizek. Study of inclusive electron-positron pair production in collisions of Ar+KCl at 1.756 A GeV. *Doctoral thesis. Czech Technical University in Prague*, 2010. 2

[Lip00] C. Lippmann. Aufbau und Inbetriebnahme eines Gasqualitätsmonitors für die HADES-Driftkammern. *Diplomarbeit. Physik-Fachbereich der Johann-Wolfgang- Goethe-Universität Frankfurt a.M.*, 2000. 8

[LL09] S. Leupold and M. F. M. Lutz. Hadronic three-body decays of light vector mesons. *Eur. Phys. J.*, A39:205–212, 2009. 61

[N+10] K Nakamura et al. Review of particle physics. *J. Phys.*, G37:075021, 2010. 24, 38, 39, 42, 80, 108

[Nak10] K. Nakayama. private communication. 2010. 4

[NSH+98] K. Nakayama, A. Szczurek, C. Hanhart, J. Haidenbauer, and J. Speth. Production of omega mesons in proton proton collisions. *Phys. Rev.*, C57:1580–1587, 1998. 3

[Rus06] A. Rustamov. Exclusive η meson reconstruction in proton-proton collisions at 2.2 gev with the hades spectrometer and high resolution tracking. *Disseration. Technische Universität Darmstadt*, 2006. 41, 45, 81

[Sau] F. Sauli. Principles of Operation of Multiwire Proportional and Drift Chambers. CERN-77-09. 25

[Sie10] J. Siebenson. Exclusive analysis of the $\Lambda(1405)$ resonance in the charged $\Sigma\pi$ decay channels in proton-proton reactions with HADES. *Diplomarbeit. Technische Universität Müchen*, 2010. 41

[Str98] J. Stroth. A Low-mass Tracking System for HADES. *WCC 98, Vienna*, 1998. 9

[Tar10] A. Tarantola. ω production in p+p reactions at 3.5 GeV with the HADES experiment and new electronics for the readout of the multiwire drift chambers. *Disseration. Goethe Universität Frankfurt*, 2010. 3

[Tei07] K. Teilab. Eine neue Methode der Zeiteichung der HADES Driftkammern. *Diplomarbeit. Goethe Universität Frankfurt*, 2007. 6

[W$^+$93] P. Weidenauer et al. N anti-N annihilation at rest into five pions. *Z. Phys.*, C59:387–398, 1993. 61

[Web11] M. Weber. *Disseration. Technische Universität München*, 2011. 3

Appendix A

Acceptance plots

Table A.1 and A.2 provide additional plots to those shown in tables 5.2 and 5.3.

Table A.1: The acceptance of η mesons as a function of different observables. The figures show the number of simulated events in 4π (Pluto input) and the corresponding number of reconstructed events (HADES acceptance) as a function of the selected observable.

DOF	Pluto input	HADES acceptance
$cos\theta^{\eta}_{CM}$	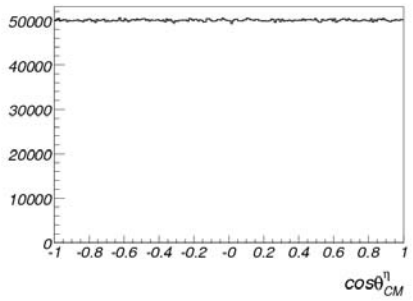	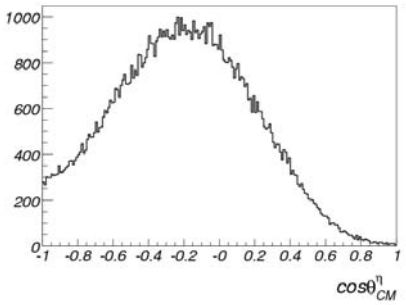
$cos\theta^{p}_{pp}$	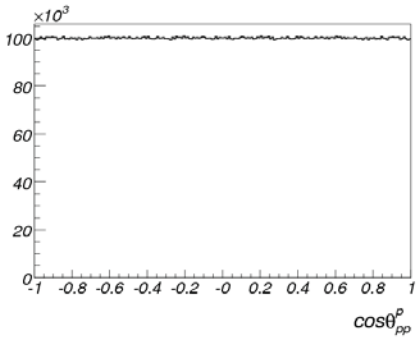	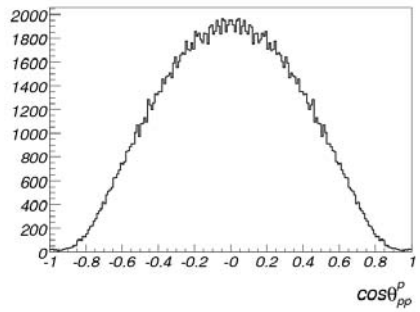

Continued on next page

Table A.1 – continued from last page

DOF	Pluto input	HADES acceptance
$M^2_{p\eta}$	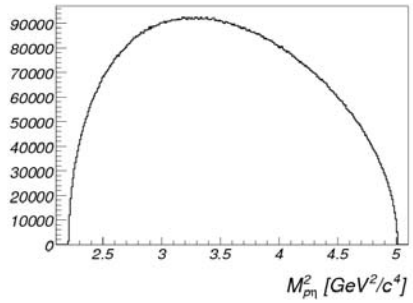	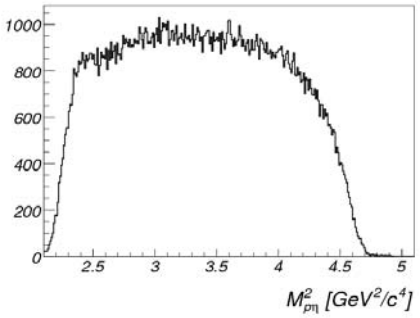
M^2_{pp}	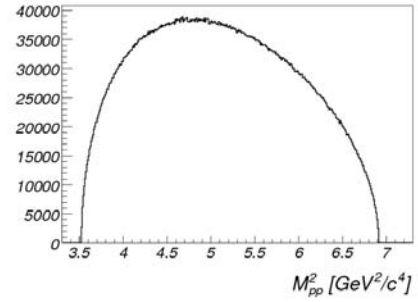	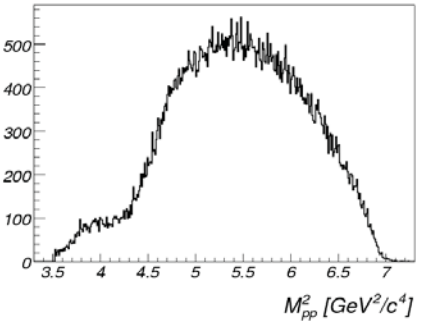
$cos\theta^p_{pp}$ vs $cos\theta^\eta_{CM}$	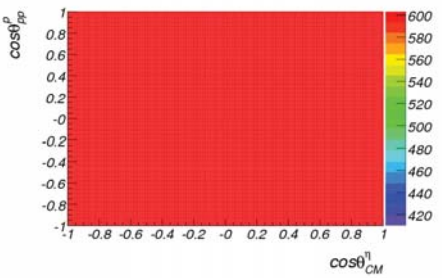	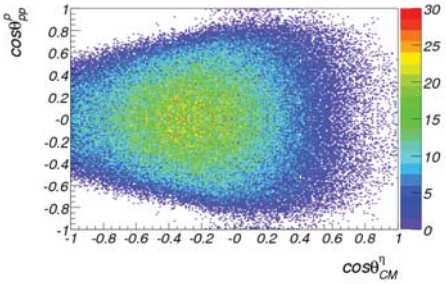
$M^2_{p\eta}$ vs $cos\theta^\eta_{CM}$	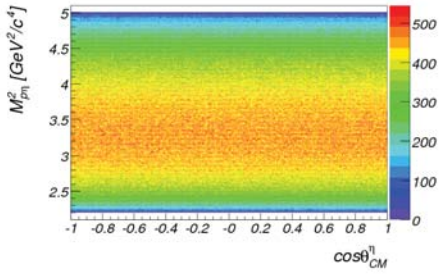	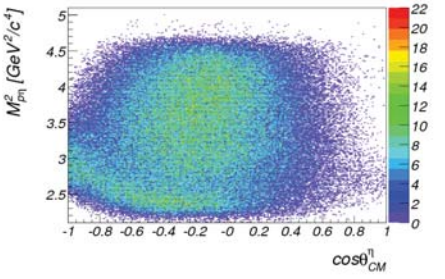

Continued on next page

Table A.1 – continued from last page

DOF	Pluto input	HADES acceptance
M^2_{pp} vs $cos\theta^{\eta}_{CM}$	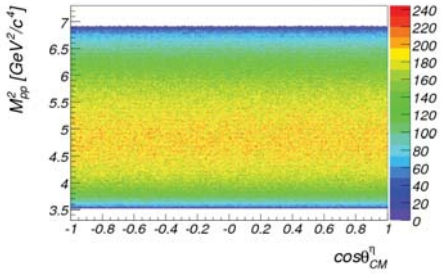	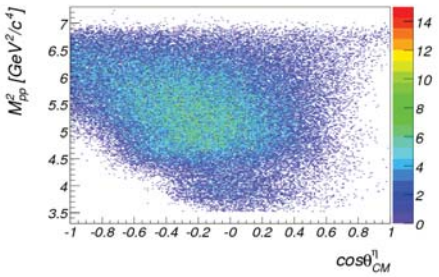
$M^2_{p\eta}$ vs $cos\theta^{p}_{pp}$	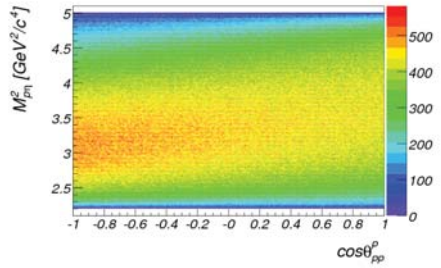	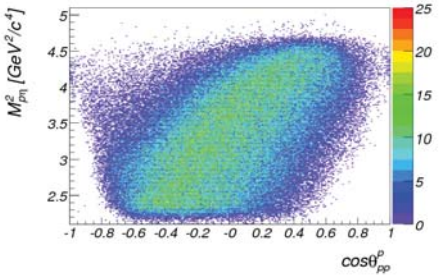
M^2_{pp} vs $cos\theta^{p}_{pp}$	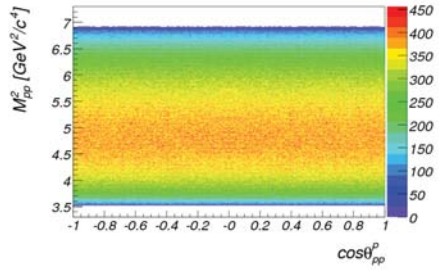	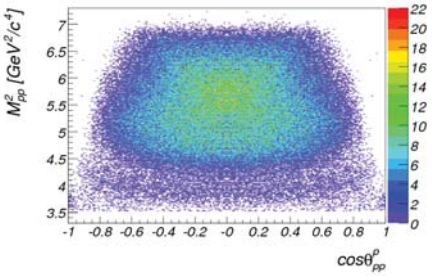
M^2_{pp} vs $M^2_{p\eta}$	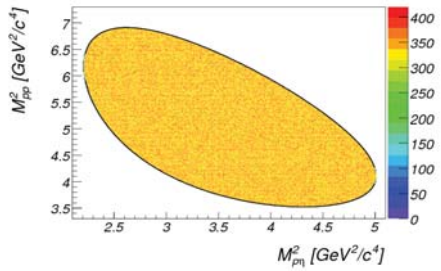	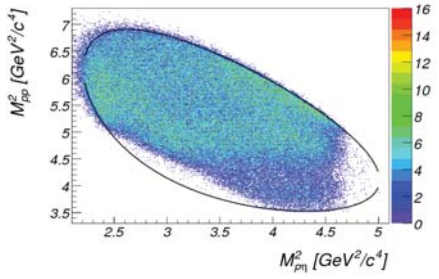
$M^2_{p\eta}$ vs $M^2_{p\eta}$	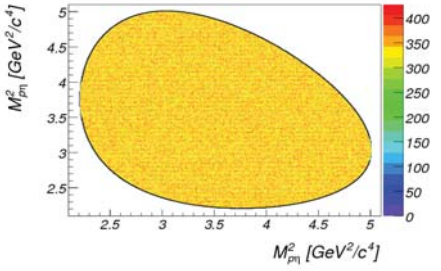	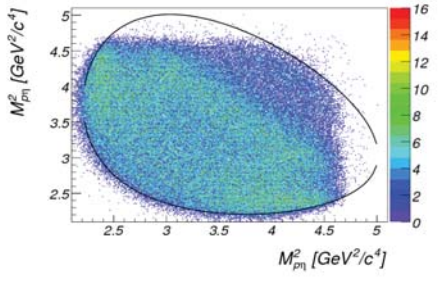

Table A.2: The acceptance of ω mesons as a function of different observables. The figures show the number of simulated events in 4π (Pluto input) and the corresponding number of reconstructed events (HADES acceptance) as a function of the selected observable.

DOF	Pluto input	HADES acceptance
$cos\theta^{\omega}_{CM}$	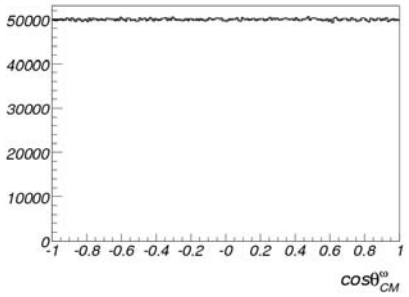	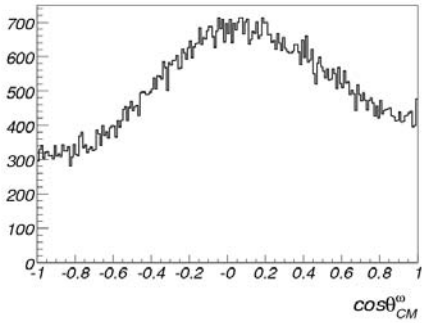
$cos\theta^{p}_{pp}$	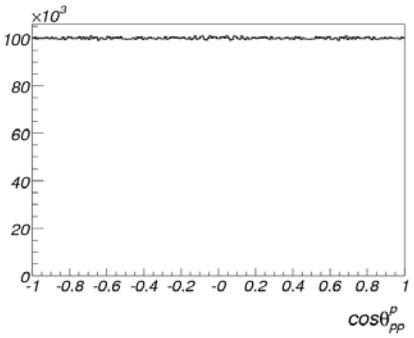	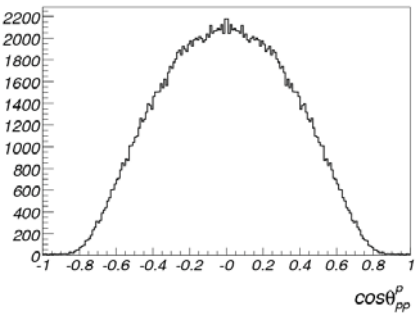
$M^2_{p\omega}$	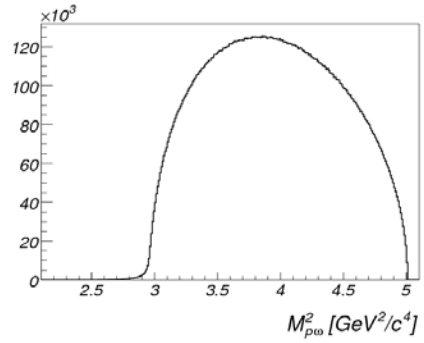	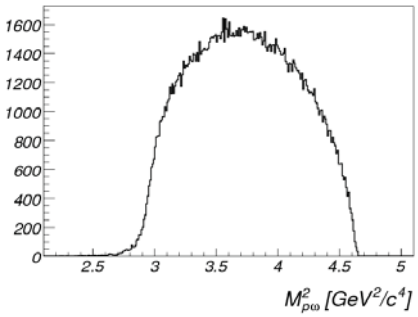

Continued on next page

Table A.2 – continued from last page

DOF	Pluto input	HADES acceptance
M^2_{pp}	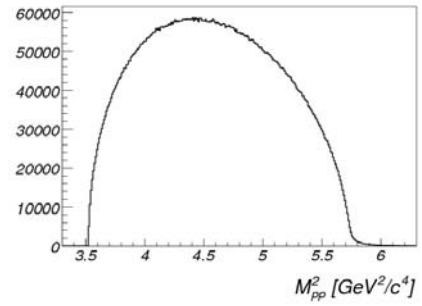	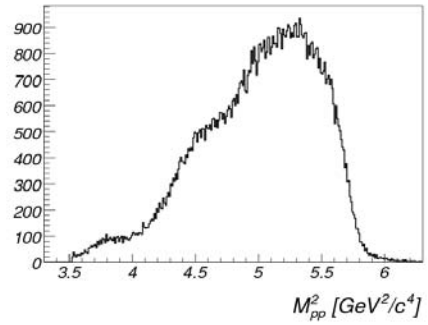
$cos\theta^p_{pp}$ vs $cos\theta^\omega_{CM}$	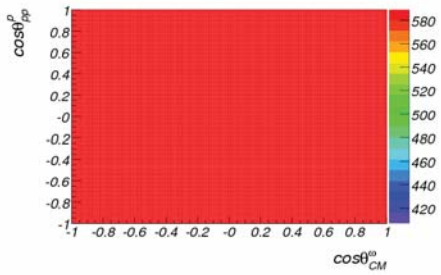	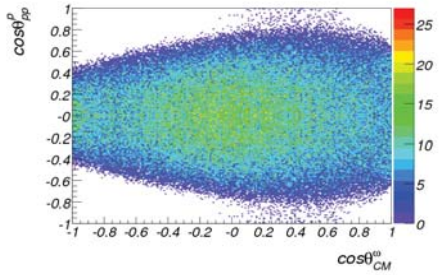
$M^2_{p\omega}$ vs $cos\theta^\omega_{CM}$	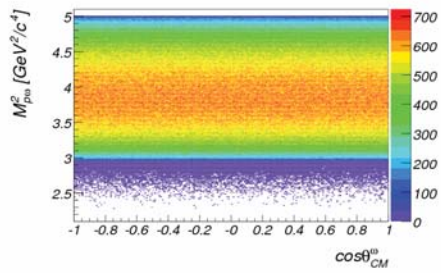	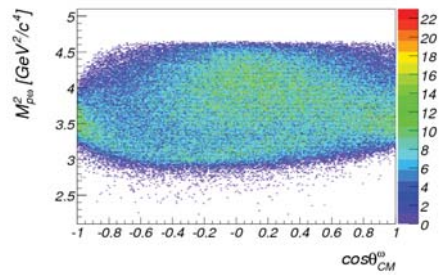
M^2_{pp} vs $cos\theta^\omega_{CM}$	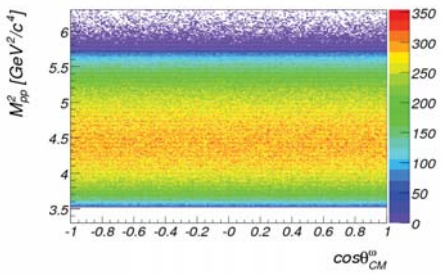	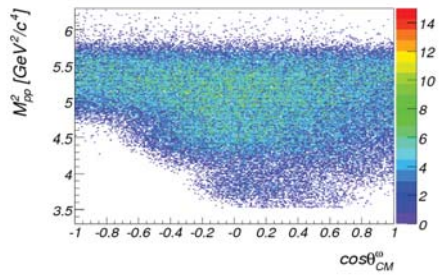

Continued on next page

Table A.2 – continued from last page

DOF	Pluto input	HADES acceptance
$M^2_{p\omega}$ vs $cos\theta^p_{pp}$	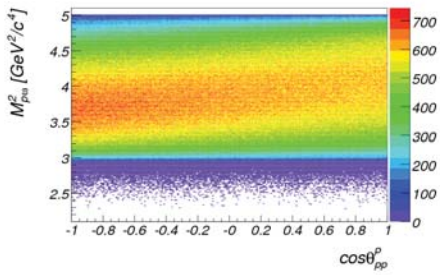	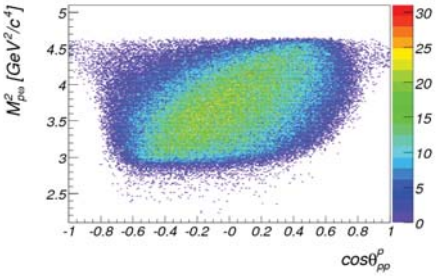
M^2_{pp} vs $cos\theta^p_{pp}$	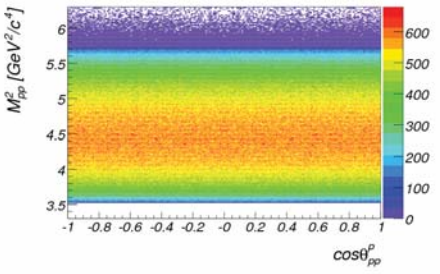	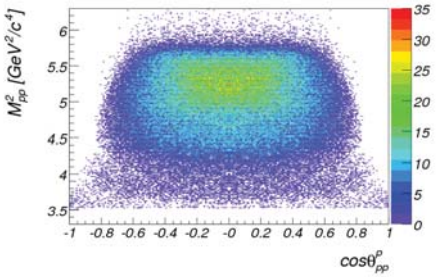
M^2_{pp} vs $M^2_{p\omega}$	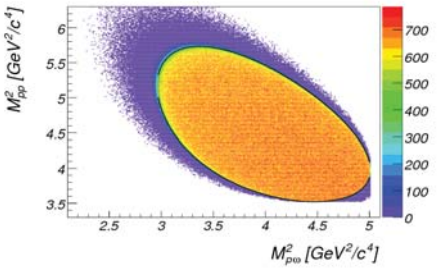	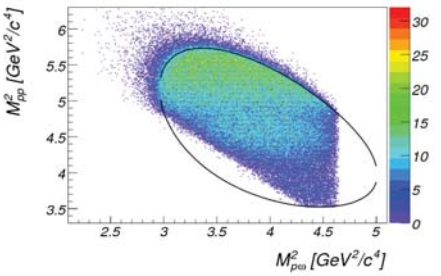
$M^2_{p\omega}$ vs $M^2_{p\omega}$	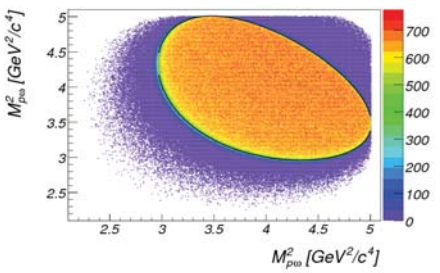	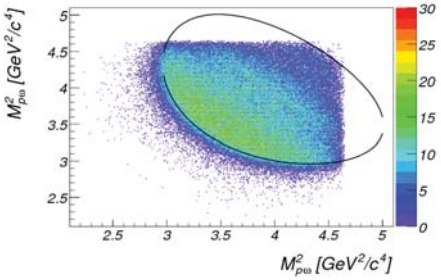

Appendix B

Angular distributions

The angular distribution of protons was measured in the range $|cos\theta^{p}_{pp}| < 0.6$ in the two reactions: $pp \longrightarrow pp\eta$ and $pp \longrightarrow pp\omega$. Both distributions are fairly isotropic as shown in sections B.1 and B.2. The angular distribution of η mesons in the reaction center-of-mass system is shown in section B.3.

All angular distributions presented in this appendix were fitted twice; using the first Legendre polynomial (P_0) and using the first and third Legendre polynomials ($P_0 + P_2$). The results of the fits are given.

B.1 proton angular distribution in the reaction $pp \longrightarrow pp\eta$

The acceptance corrected distribution of events in the reaction $pp \longrightarrow pp\eta$ as a function of $cos\theta^{p}_{pp}$ is shown in figure B.1. The events were selected within the range $|cos\theta^{\eta}_{CM}| \leq 0.4$ and $M^2_{pp} \geq 4.5$ GeV^2/c^4.
The results of the fitting the angular distribution are given in table B.1. The distribution is fairly well fitted by a constant function (P_0) yielding a value for the χ^2 per degree of freedom less than one.

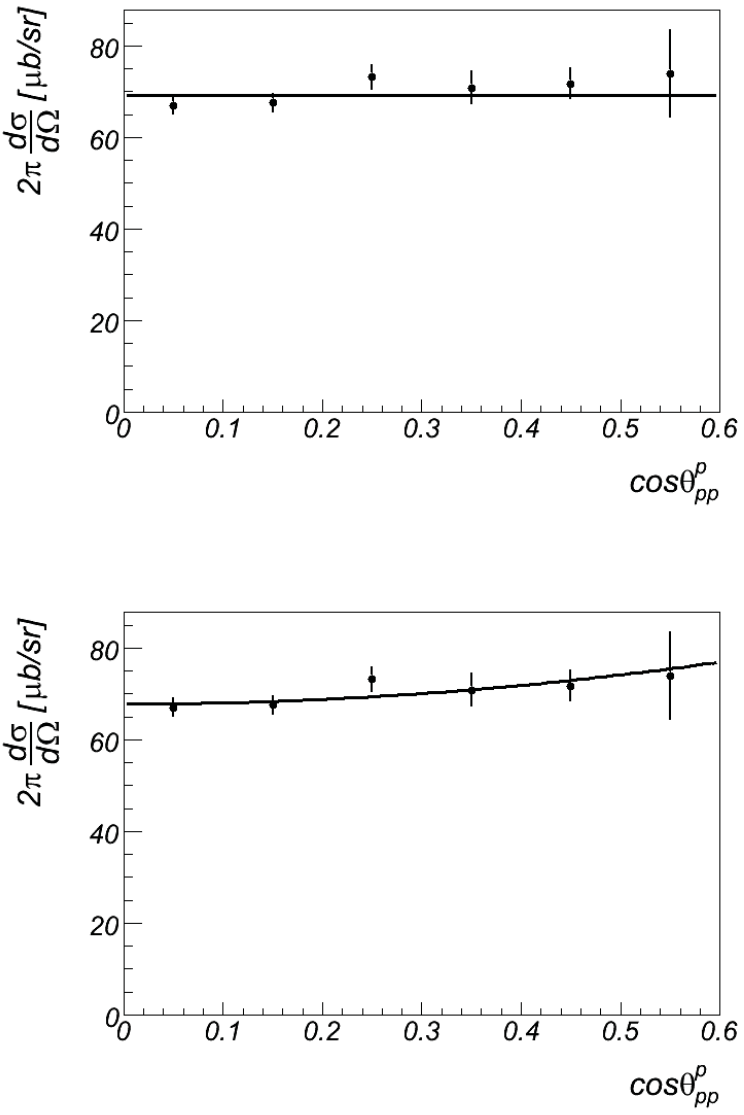

Figure B.1: Angular distribution of protons in the reaction $pp \longrightarrow pp\eta$. The spectra are corrected for spectrometer acceptance and fitted in (a) using the first Legendre polynomial (P_0) and in (b) using the first and third Legendre polynomials ($P_0 + P_2$). The results of the fits are given in table B.1.

Fit function	Result	χ^2/NDF
αP_0	$2\pi\frac{d\sigma}{d\Omega} = (69.27 \pm 1.18)P_0$ [μb/sr]	0.93
$\alpha(P_0 + \beta P_2)$	$2\pi\frac{d\sigma}{d\Omega} = (76.27 \pm 4.74) \times (P_0 + (0.22 \pm 0.13)P_2)$ [μb/sr]	0.58

Table B.1: Results of fitting the proton angular distribution in the reaction $pp \longrightarrow pp\eta$. P_0 and P_2 are the first and third Legendre polynomials, respectively. α and β are free parameters of the fit. NDF denotes the number of degrees of freedom.

B.2 proton angular distribution in the reaction $pp \longrightarrow pp\omega$

The acceptance corrected distribution of events in the reaction $pp \longrightarrow pp\omega$ as a function of $cos\theta^p_{pp}$ is shown in figure B.2. The events were selected within the range $-0.5 \leq cos\theta^{\omega}_{CM} \leq 1$ and $M^2_{pp} \geq 4.3$ GeV^2/c^4.
The results of the fitting the distribution are given in table B.2. The distribution is fairly well fitted by a constant function (P_0) yielding a value for the χ^2 per degree of freedom less than one.

Fit function	Result	χ^2/NDF
αP_0	$2\pi\frac{d\sigma}{d\Omega} = (57.1 \pm 0.92)P_0$ [μb/sr]	0.34
$\alpha(P_0 + \beta P_2)$	$2\pi\frac{d\sigma}{d\Omega} = (59.65 \pm 2.62) \times (P_0 + (0.13 \pm 0.11)P_2)$ [μb/sr]	0.14

Table B.2: Results of fitting the proton angular distribution in the reaction $pp \longrightarrow pp\omega$. P_0 and P_2 are the first and third Legendre polynomials, respectively. α and β are free parameters of the fit. NDF denotes the number of degrees of freedom.

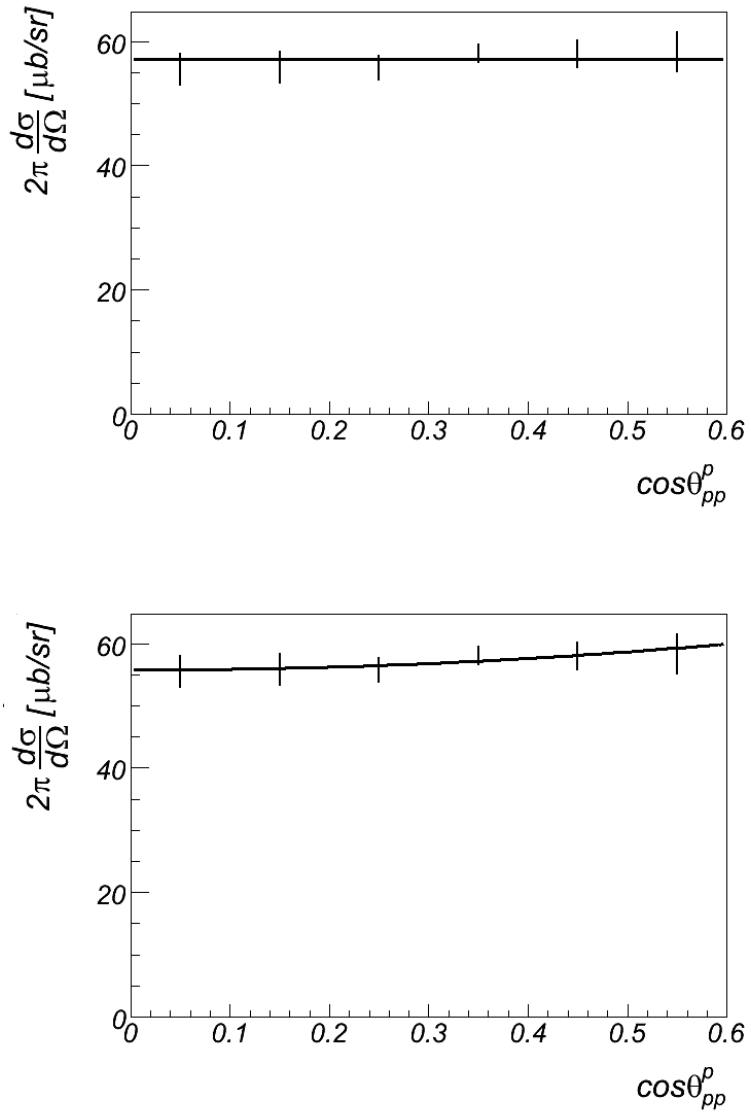

Figure B.2: Angular distribution of protons in the reaction $pp \longrightarrow pp\omega$. The spectra are corrected for spectrometer acceptance and fitted in (a) using the first Legendre polynomial (P_0) and in (b) using the first and third Legendre polynomials ($P_0 + P_2$). The results of the fits are given in table B.2.

B.3 η meson angular distribution

The acceptance corrected distribution of events in the reaction $pp \longrightarrow pp\eta$ as a function of $cos\theta^{\eta}_{CM}$ is shown in figure B.3. The events were selected within the range $|cos\theta^{p}_{pp}| \leq 0.4$ and $M^2_{pp} \geq 5.5$ GeV^2/c^4.
The results of the fitting the angular distribution are given in table B.1. Fitting the distribution using the first and third Legendre polynomial yields a value for the χ^2 per degree of freedom close to one, whereas the fit using only the first Legendre polynomial yields a value for the χ^2 per degree of freedom larger than two. Therefore, the first mentioned choice of the fit function is favored.

Fit function	Result	χ^2/NDF
αP_0	$2\pi\frac{d\sigma}{d\Omega} = (70.36 \pm 0.85)P_0$ [μb/sr]	2.32
$\alpha(P_0 + \beta P_2)$	$2\pi\frac{d\sigma}{d\Omega} = (67.64 \pm 1.2) \times (P_0 - (0.155 \pm 0.05)P_2)$ [μb/sr]	0.99

Table B.3: Results of fitting the integrated η meson angular distribution in the reaction $pp \longrightarrow pp\eta$. P_0 and P_2 are the first and third Legendre polynomials, respectively. α and β are free parameters of the fit. NDF denotes the number of degrees of freedom.

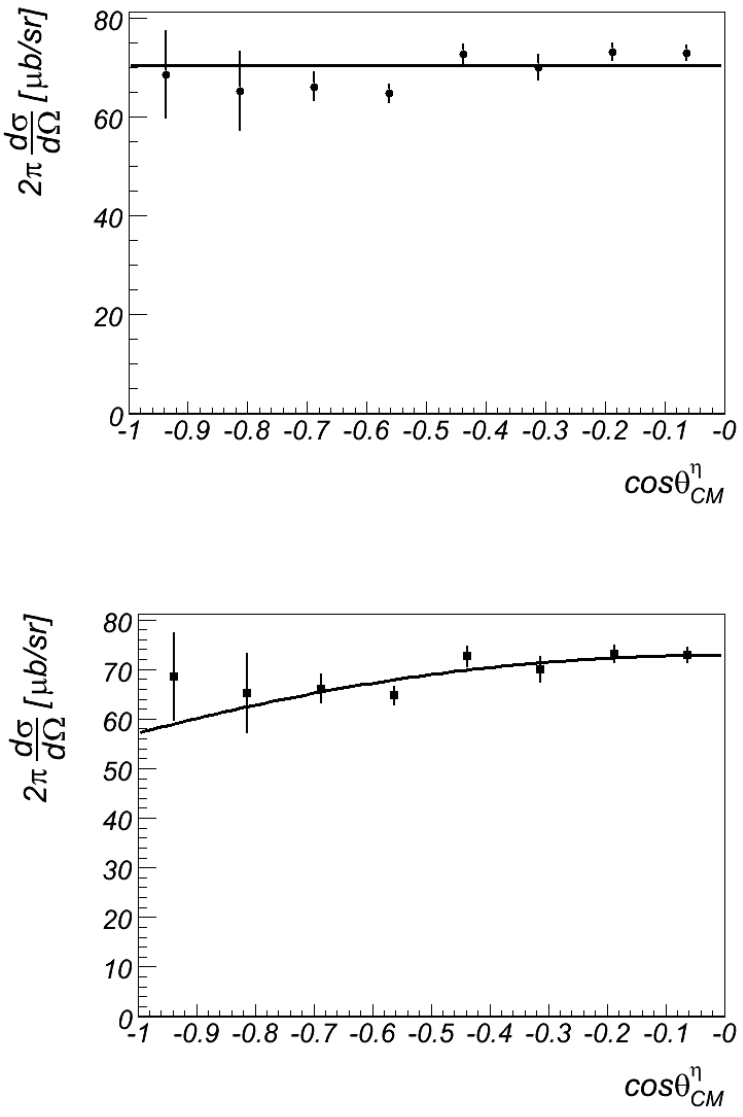

Figure B.3: Angular distribution of η mesons in the reaction $pp \longrightarrow pp\eta$. The spectra are corrected for spectrometer acceptance and fitted in (a) using the first Legendre polynomial (P_0) and in (b) using the first and third Legendre polynomials ($P_0 + P_2$). The results of the fits are given in table B.3.

Lebenslauf

Khaled Teilab

Geburtsdatum: 14.03.1982
Geburtsort: Paris, Frankreich

1999:	Abitur	Saad Zaghloul Secondary School Kairo, Ägypten
1999-2003:	Bachelor studies	Physics Department. Faculty of Science Cairo University. Kairo, Ägypten
Mai 2003:	B.Sc. degree	Special physics section
2003-2004:	Teaching assistant	Physics Department. Faculty of Science Cairo University. Kairo, Ägypten
März 2005:	DSH	Deutsche Sprachprüfung für den Hochschulzugang Studienkolleg der Goethe-Universität Frankfurt am Main, Deutschland
2005-2007:	Diplomstudium	Fachbereich Physik. Goethe-Universität Frankfurt am Main, Deutschland
Juli 2007:	Diplom Betreuer:	Institut für Kernphysik. Goethe-Universität Prof. Dr. Herbert Ströbele
2007-2011:	Doktorand Betreuer:	Institut für Kernphysik. Goethe Universität Prof. Dr. Herbert Ströbele Prof. Dr. Joachim Stroth

اَللّهمَّ مَا أَصبَحَ بي مِن نِعمَةٍ أَو بِأَحَدٍ مِن خَلقِكَ، فَمِنكَ وَحدَكَ لَا شَريكَ لَكَ، فَلَكَ الحَمدُ وَ لَكَ الشُكرُ.

O Allah, what blessing I or any of Your creation have risen upon, is from You alone, without partner, so for You is all praise and unto You all thanks.

Acknowledgment

This thesis has been only possible by the support and help of many people, whom I wish to thank all. In the first place, I would like thank my supervisors Prof. Herbert Ströbele and Prof. Joachim Stroth, who gave me the chance to join the international HADES collaboration and carry out this study. From their wide experience, I learned a lot about experimental nuclear physics and data analysis.

The continuous discussions and help of Dr. Ingo Fröhlich have been essential for carrying out this work. His broad knowledge of such type of studies and being ready for discussion at any time, always provided me with valuable suggestions.

I would also like to thank Dr. Jochen Markert for his continuous support concerning ROOT, HYDRA, the GSI batch farm, and all possible software issues.

Without the effort of every member of the HADES collaboration, the collection of the data and its analysis would never have been possible. Nevertheless, I want to explicitly thank some of them, with whom I had more contact and discussions about physics, analysis, software and detectors. These are: Prof. Piotr Salabura, Dr. Anar Rustamov, Dr. Ilse König, Dr. Christian Müntz, and Dr. Jerzy Pietraszko.

The HADES group at GSI has been my new family since I came to Germany. I would like to cordially thank all of them, especially my roommates Dr. Alexander Schmah, Dr. Yvonne Pachmayer, Dr. Simon Lang, Dr. Peter Zumbruch, and Dr. Jörn Wüstenfeld as well as Dr. Christian Sturm.

I thank my roommates in Frankfurt for the nice atmosphere in our office (and during our downstairs meetings :)) Samir Amar-Youcef, Jan Michel, and Christoph Schrader.

I would like also to thank Prof. Henner Büsching and other organizers of the H-QM school, who created that excellent program which provided many Ph.D. students –including myself– with valuable training and education and with necessary funding.

Finally, outside the university there are few persons who have done me great favors that made my life during my Ph.D. easier and better, sometimes even possible. The first of them is my wife. She has always been to my side, asking for nothing and doing everything to create a supporting atmosphere at home. I don't find words to describe my deep thanks to her.

The second person is my supervisor Prof. Herbert Ströbele who continuously helped me during all my stay in Germany, in many cases even without being asked. I also admire a lot his non-complicated way of thinking and his very democratic manner. He is always ready to get convinced, if one has the right argument.

A person who made me enjoy being in Frankfurt is Dr. Christian Müntz. Since he picked me up at the airport, he has taken special care of me. Except for the museum of modern arts, he has shown me every important place in Frankfurt :).

The last person in this special list is my close friend and roommate Samir Amar-Youcef. Together, we have played football, table tennis and even paint ball. We have shared the room on almost every soft skill seminar, lecture week, or HADES summer school. He helped me during moving from one flat to another, renovating flats, or even negotiating carpet price :).

All the time since my birth till today, two persons have done all what they can to ensure the best future for me. I don't find words to describe how grateful I am for all what they did, and how glad I am that they are my parents.